

# UC San Diego

## UC San Diego Electronic Theses and Dissertations

### Title

Biodegradable porous silicon nanomaterials for imaging and treatment of cancer

### Permalink

<https://escholarship.org/uc/item/5ct3b35d>

### Author

Gu, Luo

### Publication Date

2012

Peer reviewed|Thesis/dissertation

UNIVERSITY OF CALIFORNIA, SAN DIEGO

**Biodegradable Porous Silicon Nanomaterials for Imaging and  
Treatment of Cancer**

A dissertation submitted in partial satisfaction of the requirements for the degree  
Doctor of Philosophy

in

Chemistry with Specialization in Multi-Scale Biology

by

**Luo Gu**

Committee in charge:

Professor Michael J. Sailor, Chair  
Professor Seth M. Cohen  
Professor Sadik C. Esener  
Professor Clifford P. Kubiak  
Professor James K. Whitesell

2012

Copyright  
Luo Gu, 2012  
All rights reserved.

The dissertation of Luo Gu is approved, and it is acceptable in quality and form for publication on microfilm and electronically:

---

---

---

---

---

Chair

University of California, San Diego

2012

## **DEDICATION**

This dissertation is dedicated:

To my late Grandma, Guiqin Jiang, who always cared more about my grades than I did.

To my Mom, a “Chinese mom”, who never gives me pressure and would be just happy if I could ever get a degree from any college.

To my Dad, a professor of fine arts, who once dreamed to train me as an artist but still has been supportive to my Ph.D. study even though I showed no interest in painting.

To my fascination with understanding the physical world.

# TABLE OF CONTENTS

Signature Page.....	iii
Dedication.....	iv
Table of Contents.....	v
List of Figures.....	viii
List of Tables.....	xii
Acknowledgements.....	xiii
Vita.....	xv
Abstract of Dissertation.....	xvii
<b>Chapter I: Introduction.....</b>	<b>1</b>
1.1 Motivation.....	2
1.2 Nanotechnology in the treatment of cancer.....	2
1.3 Limit of nanomaterials for biomedical applications.....	4
1.4 Porous silicon.....	5
1.5 Toxicity and biodegradation of porous silicon.....	5
1.6 Porous silicon for biomedical applications.....	7
1.7 References.....	9
<b>Chapter II: Development of Biodegradable Luminescent Porous Silicon Nanoparticles for In Vivo Applications.....</b>	<b>21</b>
2.1 Abstract.....	22
2.2 Introduction.....	22
2.3 Experimental.....	24
2.4 Results and discussion.....	32
2.5 Conclusions.....	37
2.6 References.....	37

<b>Chapter III: In Vivo Time-Gated Fluorescence Imaging with Biodegradable Luminescent Porous Silicon Nanoparticles.....</b>	<b>56</b>
3.1 Abstract.....	57
3.2 Introduction.....	57
3.3 Experimental.....	59
3.4 Results and discussion.....	62
3.5 Conclusions.....	68
3.6 References.....	69
<b>Chapter IV: Magnetic Luminescent Porous Silicon Microparticles for Localized Delivery of Molecular Drug Payloads.....</b>	<b>83</b>
4.1 Abstract.....	84
4.2 Introduction.....	84
4.3 Experimental.....	85
4.4 Results and discussion.....	90
4.5 Conclusions.....	96
4.6 References.....	96
<b>Chapter V: The Phototoxicity of Porous Silicon Nanoparticle Photosensitizers against Cancer Cells.....</b>	<b>114</b>
5.1 Abstract.....	115
5.2 Introduction.....	115
5.3 Experimental.....	117
5.4 Results and discussion.....	120
5.5 Conclusions.....	124
5.6 References.....	125
<b>Chapter VI: Multivalent Porous Silicon Nanoparticles Enhance the Immune Activation Potency of Agonistic CD40 Antibody.....</b>	<b>140</b>
6.1 Abstract.....	141
6.2 Introduction.....	141
6.3 Experimental.....	143
6.4 Results and discussion.....	147
6.5 Conclusions.....	151
6.6 References.....	152
<b>Appendix A: Generation of Porous Silicon Images on Si Wafers.....</b>	<b>169</b>
A.1 Introduction.....	170

A.2 Materials.....	170
A.3 Experimental.....	170
A.4 References.....	171



## LIST OF FIGURES

Figure 1.1	Mortality in the US based on the cause of death, year of 2007.....	13
Figure 1.2	Change in US death rates of diseases, from 1991 to 2007.....	14
Figure 1.3	Examples of some common nanomaterials.....	15
Figure 1.4	Examples of nanoparticle-based products that have been approved for clinical use.....	16
Figure 1.5	Porous silicon.....	17
Figure 1.6	Serum silicon concentration of various age groups.....	18
Figure 1.7	Long term toxicity and degradation of hydrosilylated porous Si particles in the eye (rabbit model).....	19
Figure 1.8	Fluorescence microscopy image of magnetic, luminescent porous silicon microparticles.....	20
Figure 2.1	Characterization of luminescent porous Si nanoparticles (LPSiNP).....	40
Figure 2.2	Schematic diagram of the synthesis of luminescent porous silicon nanoparticles (LPSiNP).....	41
Figure 2.3	FTIR spectra of porous silicon film and luminescent porous silicon nanoparticles (LPSiNP).....	42
Figure 2.4	Photoluminescence spectra of LPSiNP.....	43
Figure 2.5	Characterization of three types of LPSiNP prepared with different porous nanostructures.....	44
Figure 2.6	Characterization of LPSiNP with different average particle sizes, prepared using the same etching conditions (200 mA/cm <sup>2</sup> for 150 sec).....	45
Figure 2.7	Photostability of LPSiNP compared to conventional fluorophores.....	46
Figure 2.8	Quantum yield (QY=10.2%) of luminescent porous Si nanoparticles (LPSiNP) compared to Rhodamine 101 (QY=100%).....	47
Figure 2.9	Evolution of photoluminescence spectrum of LPSiNP during degradation under physiological conditions.....	48
Figure 2.10	Biocompatibility and biodegradability of luminescent porous Si nanoparticles (LPSiNP).....	49
Figure 2.11	Optical microscope images of HeLa cells incubated with LPSiNP at various concentrations.....	50
Figure 2.12	In vitro, in vivo and ex vivo fluorescence imaging with luminescent porous Si nanoparticles (LPSiNP).....	51

Figure 2.13	In vitro cellular imaging with LPSiNP.....	52
Figure 2.14	Characterization of dextran-coated luminescent porous silicon nanoparticles (D-LPSiNP).....	53
Figure 2.15	Fluorescence images of tumors containing dextran-coated luminescent porous Si nanoparticles (D-LPSiNP).....	54
Figure 3.1	Characterization of polyethylene glycol-conjugated luminescent porous silicon nanoparticles (PEG-LPSiNPs).....	72
Figure 3.2	Steady-state photoluminescence (PL) spectra of LPSiNPs in deionized water.....	73
Figure 3.3	Photoluminescence decay curves for LPSiNPs prepared at etching current densities of 50 mA/cm <sup>2</sup> , 200 mA/cm <sup>2</sup> , or 400 mA/cm <sup>2</sup> .....	74
Figure 3.4	Transmission electron microscope image of polyethylene glycol coated LPSiNPs (PEG-LPSiNPs).....	75
Figure 3.5	In vitro and in vivo comparison of time-domain fluorescence characteristics of porous Si nanoparticles (PEG-LPSiNPs) and the common imaging fluorophore Cy3.5.....	76
Figure 3.6	Comparison of PEG-LPSiNPs and mCherry in the time-domain.....	77
Figure 3.7	Time-gated fluorescence images comparing PEG-LPSiNP with fluorescent protein mCherry in a nude mouse bearing mCherry-expressing tumors...	78
Figure 3.8	Time-gated fluorescence images of mouse bearing SKOV3 xenograft tumor after IV (tail vein) injection of PEG-LPSiNPs.....	79
Figure 3.9	Ex vivo fluorescence images of SKOV3 xenograft tumor and muscle in the vicinity of the tumor.....	80
Figure 4.1	Preparation and characterization of magnetic luminescent porous Si microparticles.....	101
Figure 4.2	FTIR spectra of porous silicon film and luminescent porous silicon microparticles, prior to loading of magnetite nanoparticles.....	102
Figure 4.3	Optical and magnetic characterization of porous Si microparticles.....	103
Figure 4.4	N <sub>2</sub> adsorption/desorption isotherms of porous Si microparticles before and after loading of magnetite nanoparticles.....	104
Figure 4.5	Photostability of porous Si microparticles.....	105
Figure 4.6	Characterization of DOX loaded magnetic, luminescent porous Si microparticles.....	106

Figure 4.7	UV-Vis absorption spectra of DOX standard in ethanol and DOX extracted from DOX loaded magnetic luminescent porous Si microparticles in ethanol.....	107
Figure 4.8	In vitro cytotoxicity of doxorubicin (DOX) alone compared to DOX plus iron oxide nanoparticles towards HeLa cells.....	108
Figure 4.9	Magnetic field guided delivery of DOX using magnetic luminescent porous Si microparticles.....	109
Figure 4.10	Phase contrast and fluorescence microscope images of a control dish of HeLa cells.....	110
Figure 4.11	Phase contrast microscope images of HeLa cells after 24 h incubation with drug-free magnetic, luminescent porous Si microparticles.....	111
Figure 4.12	Phase contrast microscope images of HeLa cells after 8 h incubation with different quantities of DOX-loaded magnetic, luminescent porous Si microparticles.....	112
Figure 5.1	Synthetic procedure followed to prepare porous Si nanoparticles from a single crystal silicon substrate.....	129
Figure 5.2	Fourier-transform infrared (FT-IR) spectrum of a typical porous Si nanoparticle preparation.....	130
Figure 5.3	Generation of singlet oxygen from porous Si nanoparticles.....	131
Figure 5.4	Time course of the absorption spectrum of air-saturated DPBF and N <sub>2</sub> -saturated DPBF (0.08 mM) under irradiation.....	132
Figure 5.5	Decay curves of DPBF optical absorption at 410 nm in the presence of 5, 10, and 20 µg/mL of porous Si nanoparticles as a function of irradiation time.....	133
Figure 5.6	Normalized fluorescence spectra of SOSG incubated (25 °C) with porous Si nanoparticles (PSiNP) in the presence and in the absence of light.....	134
Figure 5.7	Detection of singlet oxygen generation from porous Si using SOSG.....	135
Figure 5.8	Photoinduced toxicity exhibited by HeLa cells treated with porous Si nanoparticles.....	136
Figure 5.9	Phase contrast microscope images of HeLa cells treated with porous Si nanoparticles (PSiNP) and control experiment.....	137
Figure 6.1	Preparation and characterization of FGK45 loaded luminescent porous silicon nanoparticles (FGK-LPSiNP).....	158
Figure 6.2	Immunoblot analysis of FGK45 loaded on luminescent porous silicon nanoparticles (LPSiNPs).....	159

Figure 6.3	Representative hydrodynamic size data.....	160
Figure 6.4	Dendritic cell uptake of FGK-LPSiNPs (1).....	161
Figure 6.5	Dendritic cell uptake of FGK-LPSiNPs (2).....	162
Figure 6.6	Photoluminescence spectra of LPSiNPs in acidic buffer solutions at room temperature.....	163
Figure 6.7	Interaction of FGK-LPSiNPs with B cells.....	164
Figure 6.8	Stimulation of B cells using various concentrations of FGK45 loaded LPSiNPs or avidin coated LPSiNPs.....	165
Figure 6.9	Amplified activation potency of FGK-LPSiNPs compared to free FGK45.....	166
Figure 6.10	No CD86 or MHC II upregulation of B cells incubated with LPSiNP....	167
Figure A.1	The setup of photo-assisted etching of a image on Si wafers.....	172
Figure A.2	Black and white images etched on Si wafers.....	173

## LIST OF TABLES

Table 3.1	Photoluminescence decay lifetimes of LPSiNPs prepared at different etching current densities and activation durations.....	81
Table 5.1	Characteristics of porous Si nanoparticles (PSiNP) prepared with different etching current densities.....	138

## ACKNOWLEDGEMENTS

The Ph.D. study has been an exciting yet challenging journey for me. Many people have helped me on the path. First, I want to thank my Ph.D. advisor Prof. Mike Sailor, an outstanding scientist, a respectable leader, and a great mentor. His guidance, encouragement, and support through the years helped me grow as a scientist. And what I learned from Mike will always help me through my career in the years to come.

I would like to thank Shawn Meade, who first showed me how to etch porous silicon. I also really enjoyed our road trips to the desert, another way to look at the world without using microscopes or test tubes. I'd like to thank Ji-Ho Park for teaching me bio-techniques, for being an awesome colleague, and for drinking soju together. I'd like to thank Brian King, Manny Orosco and Michelle Chen, who brought so much fun into the main-office. It was the best relief whenever my experiments failed for the 10th time. I'd like to thank Zhengtao Qin and Ling Xiao for helping me with my experiments and sharing Chinese culture. I'd like to thank Matt Kinsella, Andrea Potocny, Chia-chen Wu, Adrian Garcia Segal, Kim Duong, Joel Grondek, Nobuhiro Yagi, Liz Wu, Loren Perelman, Anne Ruminski, Sara Alvarez, Jenny Andrew and everybody else from the Sailor lab who helped me over the years.

I would like to thank Dr. Steve Howell for providing lab space and facility for cell and animal experiments. His insightful perspective on clinical research has helped me tremendously. I'd like to thank Dr. Erkki Ruoslahti, Dr. Sangeeta Bhatia, Dr. David Hall, Dr. Stephen Hedrick, and Dr. Laura Ruff for their help and suggestions on our collaborations.

At last, I'd like to thank Gif Cheung for constantly bringing in snacks for the hungry graduate students in the Sailor lab. We would not have survived without her. And of course, thank you for all the help and encouragement through the years!

Chapters two, three, four, five, and six are, in part, reprints of the following publications:

1. Park, Ji-Ho; **Gu, Luo**; von Maltzahn, Geoffrey; Ruoslahti, Erkki; Bhatia, Sangeeta N.; Sailor, Michael J., "Biodegradable Luminescent Porous Silicon Nanoparticles for in vivo Applications". *Nature Materials* 2009, 8 (4), 331-336.
2. **Gu, Luo**; Hall, David J.; Qin, Zhengtao; Howell, Stephen B.; Sailor, Michael J., "In Vivo Time-gated Fluorescence Imaging with Biodegradable Luminescent Porous Silicon Nanoparticles", *submitted*.
3. **Gu, Luo.**; Park, Ji-Ho; Duong, Kim H.; Ruoslahti, Erkki; Sailor, Michael J., "Magnetic Luminescent Porous Silicon Microparticles for Localized Delivery of Molecular Drug Payloads". *Small* 2010, 6 (22), 2546-2552.
4. Xiao, Ling; **Gu, Luo**; Howell, Stephen B.; Sailor, Michael J., "Porous Silicon Nanoparticle Photosensitizers for Singlet Oxygen and Their Phototoxicity Against Cancer Cells", *ACS Nano* 2011, 5 (5), 3651-3659.
5. **Gu, Luo**; Ruff, Laura E.; Qin, Zhengtao; Corr, Maripat P.; Hedrick, Stephen M.; Sailor, Michael J., "Multivalent Porous Silicon Nanoparticles Enhance the Immune Activation Potency of Agonistic CD40 Antibody", *accepted by Advanced Materials*.

## VITA

June 2004	B.S. in Chemistry, Peking University, Beijing, China
June 2007	M.S. in Chemistry, University of California, San Diego
June 2012	Ph.D. in Chemistry with Specialization in Multi-scale Biology, University of California, San Diego

## PUBLICATIONS

1. **Gu, L.**; Orosco, M.; Sailor, M. J., “Detection of Protease Activity by FRET Using Porous Silicon as an Energy Acceptor”. *Physica Status Solidi a-Applications and Materials Science* 2009, 206 (6), 1374-1376.
2. Park, J. H.; **Gu, L.**; von Maltzahn, G.; Ruoslahti, E.; Bhatia, S. N.; Sailor, M. J., “Biodegradable Luminescent Porous Silicon Nanoparticles for in vivo Applications”. *Nature Materials* 2009, 8 (4), 331-336.
3. **Gu, L.**; Park, J. H.; Duong, K. H.; Ruoslahti, E.; Sailor, M. J., “Magnetic Luminescent Porous Silicon Microparticles for Localized Delivery of Molecular Drug Payloads”. *Small* 2010, 6 (22), 2546-2552.
4. Xiao, L.; **Gu, L.**; Howell, S. B.; Sailor, M. J., “Porous Silicon Nanoparticle Photosensitizers for Singlet Oxygen and Their Phototoxicity Against Cancer Cells”, *ACS Nano* 2011, 5 (5), 3651-3659.
5. Singh, N.; Karambelkar, A.; **Gu, L.**; Lin, K.; Miller, J. S.; Chen, C. S.; Sailor, M. J.; Bhatia, S. N., “Bioresponsive Mesoporous Silica Nanoparticles for Triggered Drug Release”, *J. Am. Chem. Soc.* 2011, 133 (49), 19582-19585.
6. **Gu, L.**; Ruff, L.E.; Qin, Z.; Corr, M.P.; Hedrick, S. M.; Sailor, M. J., “Multivalent Porous Silicon Nanoparticles Enhance the Immune Activation Potency of Agonistic CD40 Antibody”, *Advanced Materials*, accepted.
7. **Gu, L.**; Fang, R.; Sailor, M. J.; Park, J. H., “In Vivo Clearance and Toxicity of Monodisperse Iron Oxide Nanocrystals”, *ACS Nano*, accepted.
8. **Gu, L.**; Hall, D.J.; Qin, Z.; Howell, S. B.; Sailor, M. J., “In Vivo Time-gated Fluorescence Imaging with Biodegradable Luminescent Porous Silicon Nanoparticles”, *submitted*.



9. Qin, Z.; **Gu, L.**; Sailor, M. J., “Controlled synthesis of porous silicon nanoparticles through perforated etching”, *in preparation*.

10. **Gu, Luo**; Huang, Carlos; Kotamraju, Venkata Ramana; Adams, Preston L.; Braun, Gary; Teesalu, Tambet; Sugahara, Kazuki N.; Yagi, Nobuhiro; Tsai, Olivia; Howell, Stephen B.; Ruoslahti, Erkki; Sailor, Michael J., “Biodegradable porous silicon nanoparticles conjugated with iRGD show specificity to ovarian cancer cells”, *in preparation*.

## **ABSTRACT OF THE DISSERTATION**

### **Biodegradable Porous Silicon Nanomaterials for Imaging and Treatment of Cancer**

by

**Luo Gu**

Doctor of Philosophy in Chemistry with Specialization in Multi-Scale Biology

University of California, San Diego, 2012

Professor Michael J. Sailor, Chair

Cancer is the second leading cause of death, claiming ~0.56 million lives in the U.S. every year following heart diseases (~0.62 million). From 1991 to 2007, mortality associated with heart diseases decreased 39%; by contrast, the death rate of cancer only decreased by 17% in spite of intensive research and improved therapeutics. The stagnation of conventional medicine and the complexity of cancer demand new therapeutic strategies.

As an emerging approach, the use of nanomaterials as cancer diagnostic and therapeutic agents has shown promising results due to their unique physical and chemical properties. To date, more than two dozen nanoparticle-based products have been approved for clinical use and they show advantages over conventional therapeutics.

However, translation of many other nanomaterials has been impeded due to concerns over toxicity and biodegradability. This dissertation presents the development of biodegradable luminescent porous silicon nanomaterials and their potential applications for imaging and treatment of cancer.

After a brief introduction to nanomedicine and the biomedical applications of porous silicon, Chapter 2 presents a method of making silicon nanoparticles with porous structure and intrinsic luminescence (LPSiNPs). The low toxicity and biodegradability of LPSiNPs are demonstrated *in vitro* with human cancer cells and *in vivo* with mouse model. The *in vivo* clearance of intravenously injected LPSiNPs is studied by tracking the emission of the nanoparticles with fluorescence imaging.

Chapter 3 presents a diagnostic application of LPSiNPs. Time-gated fluorescence imaging of tumors using LPSiNPs with long emission lifetime is developed. This technique can effectively eliminate interference from short-lived tissue autofluorescence and improve the detection sensitivity.

Chapter 4-6 demonstrate the therapeutic applications of porous silicon nanomaterials. In Chapter 4, magnetically-guided delivery of anticancer drug to cancer cells *in vitro* is achieved using magnetic, luminescent porous Si microparticles. Chapter 5 demonstrates that porous silicon nanoparticles can be used as photosensitizer and generate cytotoxic singlet oxygen when irradiated by light. The phototoxicity of the nanoparticles against cancer cells is also studied. Finally, the use of LPSiNPs for immune activation is investigated in Chapter 6.

# **CHAPTER I:**

## **Introduction**

## 1.1 Motivation

About forty years ago, President Richard Nixon signed the National Cancer Act of 1971, declaring the “War on Cancer”. This act provided a strong stimulus for research to improve the understanding of cancer and to develop more effective treatments, in the hope of finding a cure for cancer<sup>1</sup>. However, forty years later cancer remains the second leading cause of death, claiming ~0.56 million lives in the U.S. every year following heart diseases (~0.62 million)<sup>2</sup>, Fig 1.1. From 1991 to 2007, the death rate of cancer only decreased by 17% in spite of intensive research and improved therapeutics; by contrast, mortality associated with heart diseases decreased 39% in the same period<sup>2</sup> (Fig 1.2). The stagnation of conventional medicine and the complexity of cancer demand new therapeutic strategies.

## 1.2 Nanotechnology in the treatment of cancer

The invention of scanning tunneling microscope in 1981 and the discovery of fullerenes in 1985 accelerated the emergence of modern nanotechnology which is the engineering of matters between molecular scale and micrometer scale<sup>3-4</sup>. Materials of nanometer size show distinct chemical and physical properties compared to the same substance at the bulk or molecular form. For example, semiconductor cadmium selenide (CdSe) with the size of a few nanometers emits visible luminescence under excitation, and the emission wavelength is dependent on the size of the nanoparticles<sup>5</sup> (Fig 1.3a); iron oxide nanoparticles display superparamagnetism<sup>6</sup> (Fig 1.3b); Carbon nanotubes have the highest tensile strength among known materials<sup>7</sup> (Fig 1.3c).

Due to their unique chemical and physical properties, the *in vivo* use of nanomaterials as diagnostic and therapeutic agents has shown promising results in the treatment of cancer<sup>8-9</sup>. In addition to the above mentioned properties, nanoparticles are much easier to engineer compared to molecular drugs due to their larger physical sizes. Diagnostic, therapeutic, and targeting components can be simultaneously integrated into a single nanoparticle to achieve multifunction or synergistic effect<sup>8</sup>. Furthermore, intravenously injected nanoparticles can circulate in the body and passively accumulate in tumor tissues due to the enhanced permeability and retention (EPR) effect<sup>8, 10-11</sup>, having decreased systemic side effects than that normally seen in the use of small molecular drugs<sup>12</sup>. Another advantage of using nanoparticles to delivery molecular drugs is that this approach can potentially bypass multi-drug resistance (MDR), a mechanism cancer cells commonly develop against chemotherapy. Cancer cells can overexpress MDR transporters that actively pump chemotherapeutic drugs out of the cell. Nanoparticles can overcome such resistance by entering the cells through endocytosis and releasing the drugs intracellularly<sup>9</sup>.

To date, more than two dozen nanoparticle-based products have been approved for clinical use and they show advantages over conventional medicine<sup>13-14</sup>. For example, Feridex<sup>®</sup> is an injectable solution containing dextran coated superparamagnetic iron oxide nanoparticles (Fig 1.4a). It is approved by US Food and Drug Administration (FDA) as magnetic resonance imaging (MRI) contrast agent. Clinical use of Feridex<sup>®</sup> show improved MRI contrast of liver lesions in patients, which can potentially aid early detection of tumors<sup>15</sup> (Fig. 1.4b). Doxil<sup>®</sup>, a liposome-encapsulated form (~100 nm vesicles composed of a lipid bilayer) of the anticancer drug doxorubicin, is used to treat

ovarian cancer and Kaposi's sarcoma that have not improved or that have worsened after treatment with other medications (Fig 1.4c). This nanoparticle formulation of doxorubicin prolongs the circulation time of the drug and enhances its accumulation in tumors (Fig 1.4d). Furthermore, Doxil<sup>®</sup> shows reduced cardiotoxicity compared to free doxorubicin due to decreased cardiac uptake<sup>12</sup>. Abraxane<sup>®</sup>, an injectable suspension containing paclitaxel albumin-bound nanoparticles, is another example of nanoparticle-based anticancer therapeutic. Paclitaxel is a small molecule that is used to treat breast, ovarian, and lung cancers. However, it has a poor solubility in water and its common solvent for clinical use polyoxyethylated castor oil has certain toxicity. The albumin nanoparticle bound formulation of paclitaxel (Abraxane<sup>®</sup>) overcomes this problem since albumin is a natural protein that carries water-insoluble molecules such as certain vitamins and hormones found in humans. In addition to the reduced toxicity, Abraxane<sup>®</sup> also shows improved response rate in patients compared to conventional paclitaxel injection<sup>16</sup>.

### **1.3 Limit of nanomaterials for biomedical applications**

Although more than two dozen nanoparticle-based products have been approved for clinical use, translation of many other nanomaterials has been impeded due to concerns over toxicity and biodegradability: heavy-metal-containing quantum dots have been shown to be toxic in biological environments<sup>17</sup>; needle-shaped carbon nanotubes display structural toxicities<sup>18</sup>; gold nanoparticles do not degrade within an acceptable time for *in vivo* use. Therefore, it is critical that the nanomaterials have low toxicity and can be harmlessly eliminated from the body in a reasonable period of time after they perform their diagnostic or therapeutic function.

#### 1.4 Porous silicon

Porous silicon was accidentally discovered by Dr. Uhlir at Bell laboratories in 1956, but it did not attract much interest from researchers until Canham, Gosele, and Lehmann reported visible photoluminescence of porous silicon caused by quantum confinement<sup>19-22</sup>. Using quantum confined porous silicon for optoelectronics did not live up to the hope because of the indirect bandgap and low electroluminescence efficiency of the material. However, the increased study of porous silicon at the same time revealed its unique properties which make this material suitable for other applications<sup>22</sup>.

Porous silicon (Fig. 1.5) can be prepared by anodic etching of single-crystal Si in HF-containing electrolyte. Its pore size and porosity can be easily adjusted by changing the etching current density, electrolyte, and wafer doping. The pore diameter of porous silicon can vary from a few nanometers to a few microns, and the porosity can be as low as 20% to 90% depending on the etching conditions. Due to the porous structure, porous silicon also has large specific surface areas (typically  $>200\text{m}^2/\text{g}$ )<sup>22</sup>.

#### 1.5 Toxicity and biodegradation of porous silicon

Safety is always the first and most important criterion for any chemicals or materials used *in vivo*. Silicon, the 2nd most abundant element in the earth's crust, is considered as an essential trace element in humans<sup>23</sup>. It is widely distributed in various mammalian (including human) tissues<sup>23-24</sup> in the form of orthosilicate ( $\text{SiO}_4^{4-}$ ). The main functions of silicon in humans are ossification of bone and possible functions in the connective tissues. A study of silicon concentration in human serum showed that the



silicon level is highest in infants and lowest in pregnant women (Fig 1.6), suggesting pregnant mothers provide silicon to the growing fetus for incorporation in bone structure and mineralization and for connective tissue development<sup>25</sup>. The main sources of silicon in our diet include grains, vegetables, and beverages. In the US, the mean daily silicon intake is ~ 20-50 mg<sup>26</sup>.

Orthosilicate is the primary degradation product of porous silicon<sup>27-28</sup>. The degradation rate of porous silicon can be controlled by its porosity, pore size, physical dimension, and surface chemistry<sup>22, 28-29</sup>. Studies have shown that porous silicon has low toxicity and are degradable in biological environments. For example, the material has been investigated in the culture of mammalian cells<sup>30-31</sup>, as implants in eye tissues<sup>32</sup>, and as intraocular drug delivery vehicles<sup>33</sup>. However, most of the toxicity and degradation studies were focused on porous silicon films or microparticles in local tissues; little has been done on the nanoparticles of porous silicon. In Chapter 2 of this dissertation, luminescent porous silicon nanoparticles (LPSiNPs) are developed, and their cytotoxicity, systemic toxicity, distribution and degradation are studied using human cancer cells *in vitro* and mouse model *in vivo*. The results show that LPSiNPs are biocompatible, have low systemic toxicity, and can degrade into components cleared by the kidneys<sup>29</sup>.

Reported toxicity from porous silicon including the release of silane ( $\text{SiH}_4$ ) when the surface hydride of freshly etched porous silicon reacts with water<sup>34</sup>. However, aging or oxidation of porous silicon can avoid such problem<sup>35</sup>. Another potential toxicity of porous silicon is hemolysis. Studies have shown that high concentration of silica nanoparticles can destruct red blood cells<sup>36</sup>. Although this phenomena has not been observed in porous silicon nanomaterials, oxidized porous silicon nanoparticles could

potentially be hemolytic due to its chemical similarity to silica nanoparticles. However, surface coating can be used to effectively reduce the hemolytic activity of silicon oxide<sup>36</sup>.

### **1.6 Porous silicon for biomedical applications**

Due to its biodegradability, low toxicity, large pore volume, tunable pore size, and intrinsic photoluminescence, porous silicon has shown considerable potential for biomedical applications<sup>37-38</sup>.

In 1995, Canham first demonstrated that porous silicon film can induce hydroxyapatite growth on its surface in simulated body fluid, suggesting the potential use of porous silicon as bioactive material for tissue engineering<sup>27</sup>. Lin *et al* showed that porous silicon chips could be used as low power biosensors to detect picomolar DNA oligomers or proteins<sup>39</sup>. Cheng *et al* studied the long-term toxicity and degradation of porous silicon microparticles in vitreous humor (Fig. 1.7). The results show the microparticles have good biocompatibility and stability, which suggests the material can be used as intraocular drug delivery system<sup>33</sup>. A first human study using radioactive Phosphorus-32 (<sup>32</sup>P) doped porous silicon microparticles as intratumoral implants to treat liver cancer showed that the treatment was safe and well tolerated. An antitumor response was also observed in the early stage of this clinical study. For oral drug delivery, Salonen and Foraker *et al* demonstrated that porous silicon microparticles could be used to carry poorly water-soluble drugs, protect them from biological environments, and better delivery the drug molecules across intestinal cell monolayers<sup>40-41</sup>. Recently, Low *et al* studied the biocompatibility of various types of porous silicon membranes in tissues of the eye. They found thermally-oxidised, aminosilanised porous silicon membrane elicited

very little host reaction following implantation into the rat eye and the material supported the attachment and growth of human ocular cells. Their finding suggests porous silicon can be potentially used to deliver cells to the ocular surface as a treatment for corneal epithelial stem cell dysfunction<sup>32</sup>. RNA interference (RNAi) is a powerful approach for silencing genes associated with a variety of pathologic conditions. However, *in vivo* delivery of interfering RNA has been a challenge due to lack of safe, efficient, and sustained system. The delivery of small interfering RNA (siRNA) using porous silicon has been demonstrated recently<sup>42</sup>. Porous silicon macroparticles loaded with liposomes containing siRNA against an oncogene resulted in sustained gene silencing for 3 weeks in ovarian cancer model<sup>42</sup>. In the study shown in Chapter 4, magnetic luminescent Si microparticles with porous nanostructures are prepared by incorporating superparamagnetic iron oxide nanoparticles into the intrinsically luminescent porous Si matrix to provide a composite that is simultaneously fluorescent and magnetic (Fig. 1.8). The anticancer drug doxorubicin is loaded into the dual-functional microparticles, and the drug is delivered to human cervical cancer (HeLa) cells *in vitro* under the guidance of a magnetic field, demonstrating magnetic manipulation, fluorescent tracking, and localized delivery of a molecular payload<sup>43</sup>.

So far, most of the biomedical applications of porous silicon have been focused on using porous silicon films or microparticles; the study on porous silicon nanoparticles has been limited due to lack of efficient preparation method<sup>29</sup>. Chapter 2, 3, 5, and 6 present some of the first applications using porous silicon nanoparticles as cancer diagnostic and therapeutic agents, demonstrating the unique properties of porous silicon nanoparticles and their advantages in biomedical applications.

Specifically, Chapter 2 provides a biofriendly method of making silicon nanoparticles with porous nanostructure and intrinsic luminescence (LPSiNPs). The nanoparticles can carry anticancer drug payload and their intrinsic photoluminescence enables monitoring of both accumulation and degradation *in vivo*.

Chapter 3 focuses on the diagnostic application of LPSiNPs. We show that the long emission lifetime of LPSiNPs can allow time-gated fluorescence imaging of tumors, eliminating interference from short-lived tissue autofluorescence or interferences from other exogenous fluorophores.

In Chapter 5 and 6, the therapeutic applications of porous silicon nanoparticles are explored. Chapter 5 demonstrates that porous silicon nanoparticles can be used as photosensitizer and generate cytotoxic singlet oxygen when irradiated by light. The phototoxicity of the nanoparticles against human cancer cells is also studied *in vitro*.

In Chapter 6, the use of LPSiNPs for immunomodulation is explored. We found that LPSiNPs have low intrinsic immunogenicity to antigen presenting cells (APC) due to their inorganic chemical composition and low similarity to natural pathogens or other “danger signals” normally presented to the immune system. However, when coated with agonistic CD40 antibody, the nanoparticles are able to substantially amplify the antibody’s activation potency on APC, equivalent to using ~30-40 fold larger concentration of the free antibody. The amplification effect suggests that a nanoparticle-based CD40 antibody therapeutic may amplify the potency and decrease the dose required in the clinical application of CD40 mAb.

## 1.7 References

1. The National Cancer Act of 1971. *Cancer* **78**, 2611-2617 (1996).
2. Altekruse, S.F. et al. in SEER Cancer Statistics Review 1975-2007, National Cancer Institute (1975-2007).
3. Binnig, G. & Rohrer, H. Scanning tunneling microscopy. *Ibm Journal of Research and Development* **30**, 355-369 (1986).
4. Kroto, H.W., Heath, J.R., O'Brien, S.C., Curl, R.F. & Smalley, R.E. C-60 - Buckminsterfullerene. *Nature* **318**, 162-163 (1985).
5. Dabbousi, B.O. et al. (CdSe)ZnS core-shell quantum dots: Synthesis and characterization of a size series of highly luminescent nanocrystallites. *Journal of Physical Chemistry B* **101**, 9463-9475 (1997).
6. Laurent, S. et al. Magnetic iron oxide nanoparticles: Synthesis, stabilization, vectorization, physicochemical characterizations, and biological applications. *Chemical Reviews* **108**, 2064-2110 (2008).
7. Yu, M.F. et al. Strength and breaking mechanism of multiwalled carbon nanotubes under tensile load. *Science* **287**, 637-640 (2000).
8. Peer, D. et al. Nanocarriers as an emerging platform for cancer therapy. *Nature Nanotechnology* **2**, 751-760 (2007).
9. Davis, M.E., Chen, Z. & Shin, D.M. Nanoparticle therapeutics: an emerging treatment modality for cancer. *Nature Reviews Drug Discovery* **7**, 771-782 (2008).
10. Iyer, A.K., Khaled, G., Fang, J. & Maeda, H. Exploiting the enhanced permeability and retention effect for tumor targeting. *Drug Discovery Today* **11**, 812-818 (2006).
11. Brigger, I., Dubernet, C. & Couvreur, P. Nanoparticles in cancer therapy and diagnosis. *Advanced Drug Delivery Reviews* **54**, 631-651 (2002).
12. Gabizon, A. et al. Prolonged circulation time and enhanced accumulation in malignant exudates of doxorubicin encapsulated in polyethylene-glycol coated liposomes. *Cancer Research* **54**, 987-992 (1994).
13. Wagner, V., Dullaart, A., Bock, A.K. & Zweck, A. The emerging nanomedicine landscape. *Nature Biotechnology* **24**, 1211-1217 (2006).
14. Zhang, L. et al. Nanoparticles in medicine: Therapeutic applications and developments. *Clin. Pharmacol. Ther.* **83**, 761-769 (2008).
15. Seneterre, E. et al. Detection of hepatic metastases: Ferumoxides-enhanced MR imaging versus unenhanced MR imaging and CT during arterial portography. *Radiology* **200**, 785-792 (1996).

16. Abraxane Prescribing information. (Abraxis BioScience, LLC, 2012).
17. Derfus, A.M., Chan, W.C.W. & Bhatia, S.N. Probing the Cytotoxicity of Semiconductor Quantum Dots. *Nano Letters* **4**, 11-18 (2003).
18. Poland, C.A. et al. Carbon nanotubes introduced into the abdominal cavity of mice show asbestos-like pathogenicity in a pilot study. *Nat. Nanotech.* **3**, 423-428 (2008).
19. Uhler, A. ELECTROLYTIC SHAPING OF GERMANIUM AND SILICON. *Bell System Technical Journal* **35**, 333-347 (1956).
20. Canham, L.T. Silicon Quantum Wire Array Fabrication by Electrochemical and Chemical Dissolution of Wafers. *Appl. Phys. Lett.* **57**, 1046-1048 (1990).
21. Lehmann, V. & Gosele, U. Porous silicon formation: a quantum wire effect. *Appl. Phys. Lett.* **58**, 856-858 (1991).
22. Sailor, M.J. Porous Silicon in Practice: Preparation, Characterization, and Applications. (Wiley-VCH, Weinheim, Germany; 2012).
23. Mertz, W. The Essential Trace-Elements. *Science* **213**, 1332-1338 (1981).
24. Yoo, Y.C. et al. Organ distribution of heavy metals in autopsy material from normal Korean. *Journal of Health Science* **48**, 186-194 (2002).
25. Van Dyck, K., Robberecht, H., Van Cauwenbergh, R., Van Vlaslaer, V. & Deelstra, H. Indication of silicon essentiality in humans - Serum concentrations in Belgian children and adults, including pregnant women. *Biological Trace Element Research* **77**, 25-32 (2000).
26. Pennington, J.A.T. Silicon in foods and diets. *Food Additives and Contaminants* **8**, 97-118 (1991).
27. Canham, L.T. Bioactive silicon structure fabrication through nanoetching techniques. *Advanced Materials* **7**, 1033-& (1995).
28. Anderson, S.H.C., Elliott, H., Wallis, D.J., Canham, L.T. & Powell, J.J. Dissolution of different forms of partially porous silicon wafers under simulated physiological conditions. *Physica Status Solidi a-Applied Research* **197**, 331-335 (2003).
29. Park, J.-H. et al. Biodegradable luminescent porous silicon nanoparticles for in vivo applications. *Nat. Mater.* **8**, 331-336 (2009).
30. Bayliss, S.C., Heald, R., Fletcher, D.I. & Buckberry, L.D. The culture of mammalian cells on nanostructured silicon. *Advanced Materials* **11**, 318-321 (1999).

31. Chin, V., Collins, B.E., Sailor, M.J. & Bhatia, S.N. Compatibility of primary hepatocytes with oxidized nanoporous silicon. *Adv. Mater.* **13**, 1877-1880 (2001).
32. Low, S.P., Voelcker, N.H., Canham, L.T. & Williams, K.A. The biocompatibility of porous silicon in tissues of the eye. *Biomaterials* **30**, 2873-2880 (2009).
33. Cheng, L. et al. Intravitreal properties of porous silicon photonic crystals: A potential self-reporting intraocular drugdelivery vehicle. *British Journal of Ophthalmology* **92**, 705-711 (2008).
34. Jay, T., Canham, L.T., Heald, K., Reeves, C.L. & Downing, R. Autoclaving of porous silicon within a hospital environment: Potential benefits and problems. *Physica Status Solidi a-Applied Research* **182**, 555-560 (2000).
35. Canham, L.T., Saunders, S.J., Heeley, P.B., Keir, A.M. & Cox, T.I. Rapid chemography of porous silicon undergoing hydrolysis. *Advanced Materials* **6**, 865-868 (1994).
36. Lin, Y.-S. & Haynes, C.L. Impacts of Mesoporous Silica Nanoparticle Size, Pore Ordering, and Pore Integrity on Hemolytic Activity. *J. Am. Chem. Soc.* **132**, 4834-4842 (2010).
37. Anglin, E.J., Cheng, L., Freeman, W.R. & Sailor, M.J. Porous silicon in drug delivery devices and materials. *Advanced Drug Delivery Reviews* **60**, 1266-1277 (2008).
38. Salonen, J., Kaukonen, A.M., Hirvonen, J. & Lehto, V.P. Mesoporous silicon in drug delivery applications. *Journal of Pharmaceutical Sciences* **97**, 632-653 (2008).
39. Lin, V.S.Y., Motesharei, K., Dancil, K.P.S., Sailor, M.J. & Ghadiri, M.R. A porous silicon-based optical interferometric biosensor. *Science* **278**, 840-843 (1997).
40. Salonen, J. et al. Mesoporous silicon microparticles for oral drug delivery: Loading and release of five model drugs. *Journal of Controlled Release* **108**, 362-374 (2005).
41. Foraker, A.B. et al. Microfabricated porous silicon particles enhance paracellular delivery of insulin across intestinal Caco-2 cell monolayers. *Pharmaceutical Research* **20**, 110-116 (2003).
42. Tanaka, T. et al. Sustained Small Interfering RNA Delivery by Mesoporous Silicon Particles. *Cancer Research* **70**, 3687-3696 (2010).
43. Gu, L., Park, J.-H., Duong, K.H., Ruoslahti, E. & Sailor, M.J. Magnetic Luminescent Porous Silicon Microparticles for Localized Delivery of Molecular Drug Payloads. *Small* **6**, 2546-2552 (2010).

## US Mortality, 2007

Rank	Cause of Death	No. of deaths	% of all deaths
1.	Heart Diseases	616,067	25.4
<b>2.</b>	<b>Cancer</b>	<b>562,875</b>	<b>23.2</b>
3.	Cerebrovascular diseases	135,952	5.6
4.	Chronic lower respiratory diseases	127,924	5.3
5.	Accidents (unintentional injuries)	123,706	5.1
6.	Alzheimer disease	74,632	3.1
7.	Diabetes mellitus	71,382	2.9
8.	Influenza & pneumonia	52,717	2.2
9.	Nephritis*	46,448	1.9
10.	Septicemia	34,828	1.4

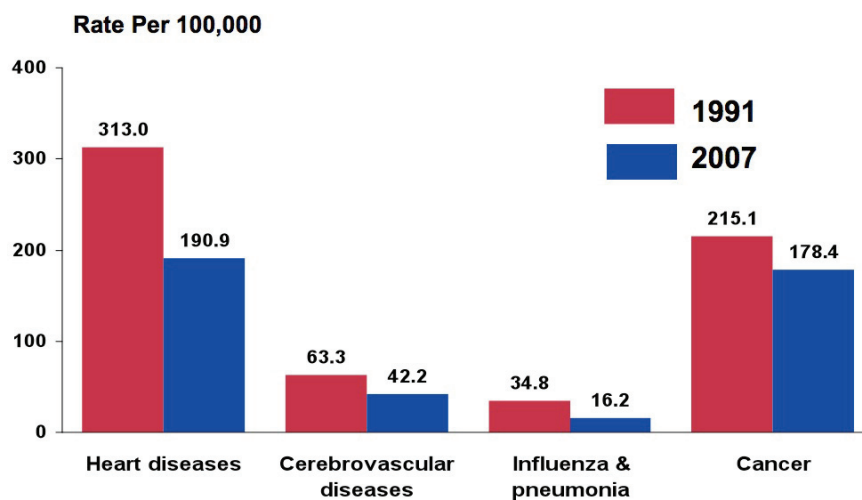
\*Includes nephrotic syndrome and nephrosis.

Source: US Mortality Data 2007, National Center for Health Statistics, Centers for Disease Control and Prevention, 2010.

**Figure 1.1 Mortality in the US based on the cause of death, year of 2007.**



## Change in US Death Rates\* from 1991 to 2007



\* Age-adjusted to 2000 US standard population.

Sources: US Mortality Data, National Center for Health Statistics, Centers for Disease Control and Prevention, 2010.

Figure 1.2 Change in US death rates of diseases, from 1991 to 2007.

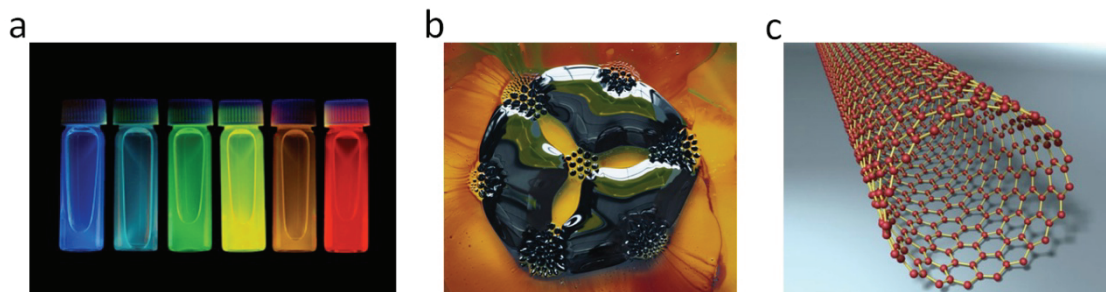


**Figure 1.3 Examples of some common nanomaterials.** (a) Photograph of photoluminescent quantum dots under ultra-violet excitation. (b) Photograph of a solution containing superparamagnetic iron oxide nanoparticles (ferrofluid). The ferrofluid forms an interesting pattern in response to a magnetic field. (c) Computer modeled carbon nanotube. Image credit: (a) and (b), Felice Frankel Photography; (c), Digital Art/Corbis.

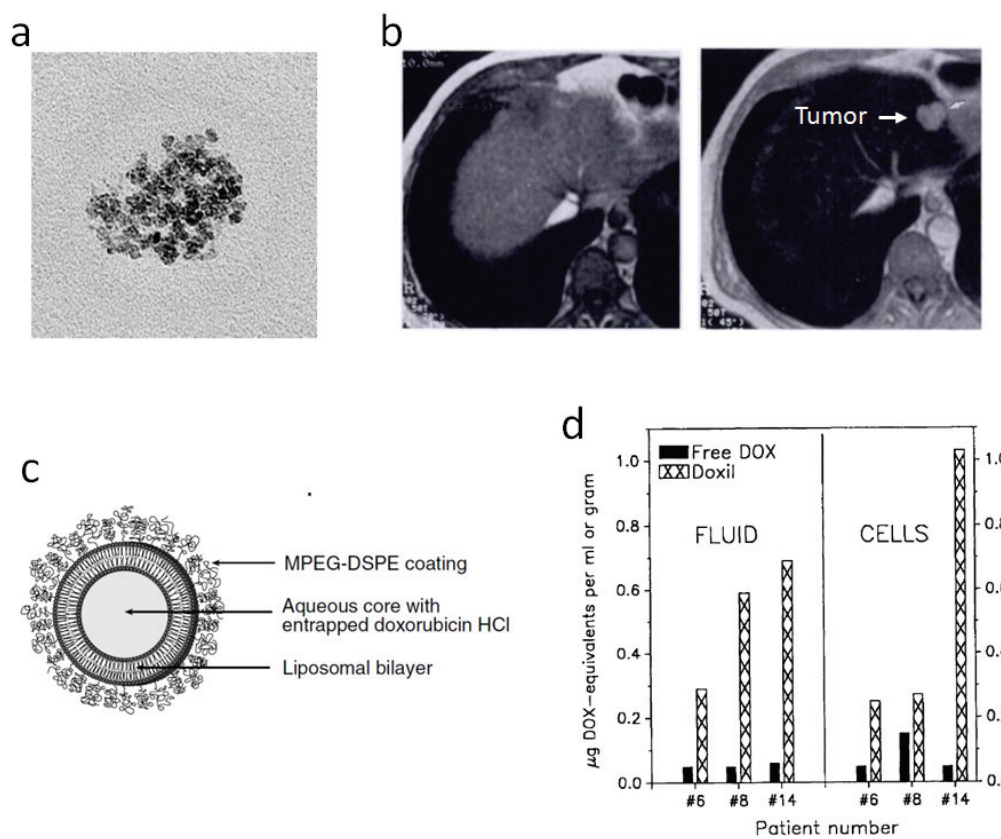


**Figure 1.4 Examples of nanoparticle-based products that have been approved for clinical use. (a)** Transmission electron microscope image of Feridex<sup>®</sup>. **(b)** Magnetic resonance imaging (MRI) of liver before (left) and after (right) use of Feridex (images are adapted from ref. 15). **(c)** Schematic diagram showing the composition of Doxil<sup>®</sup> (Image credit: Janssen Biotech, Inc.). **(d)** Doxorubicin levels in malignant pleural effusions in patients treated with free doxorubicin and Doxil (figure is adapted from ref.12).

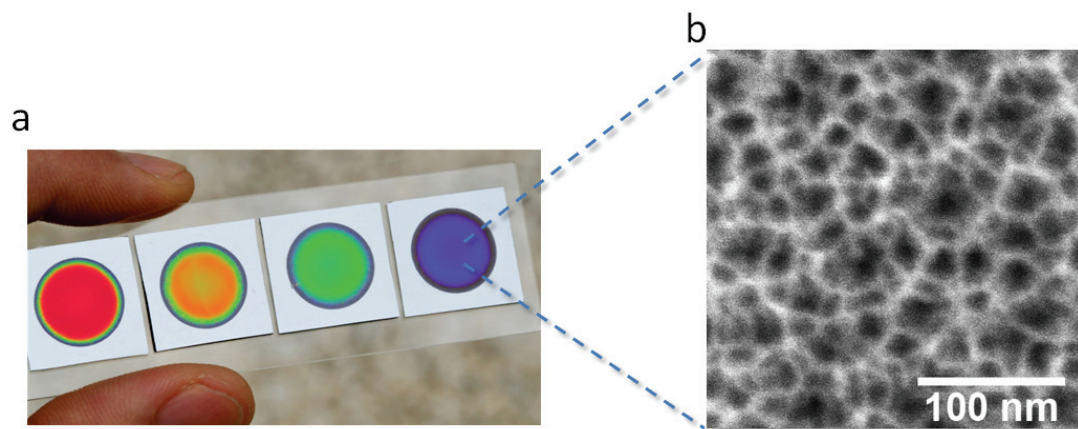


**Figure 1.5 Porous silicon.** (a) Photographs of porous silicon chips etched with various current densities and frequencies. (b) Scanning electron microscope images of porous silicon showing its porous nanostructure.

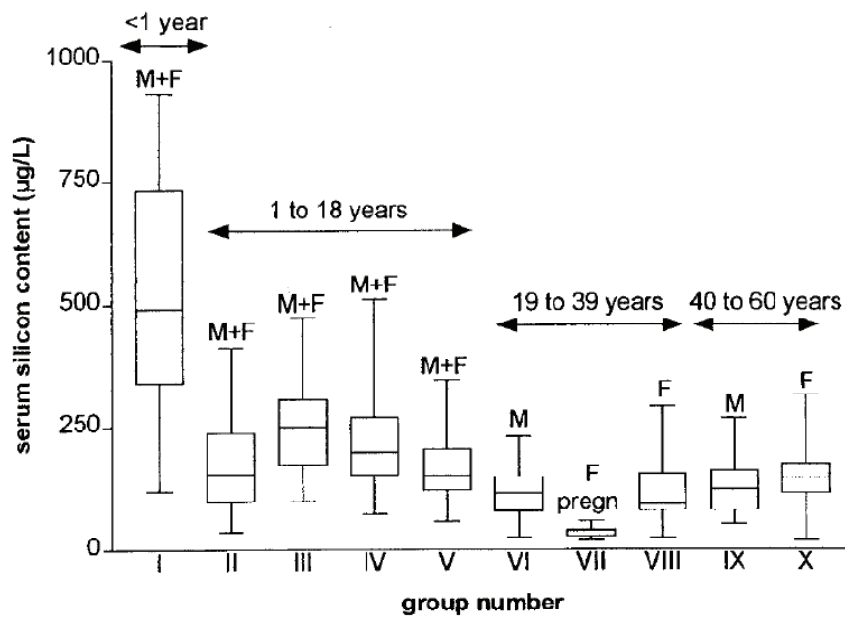


**Figure 1.6 Serum silicon concentration of various age groups. M: male; F: female; F pregn: pregnant women<sup>25</sup>.**

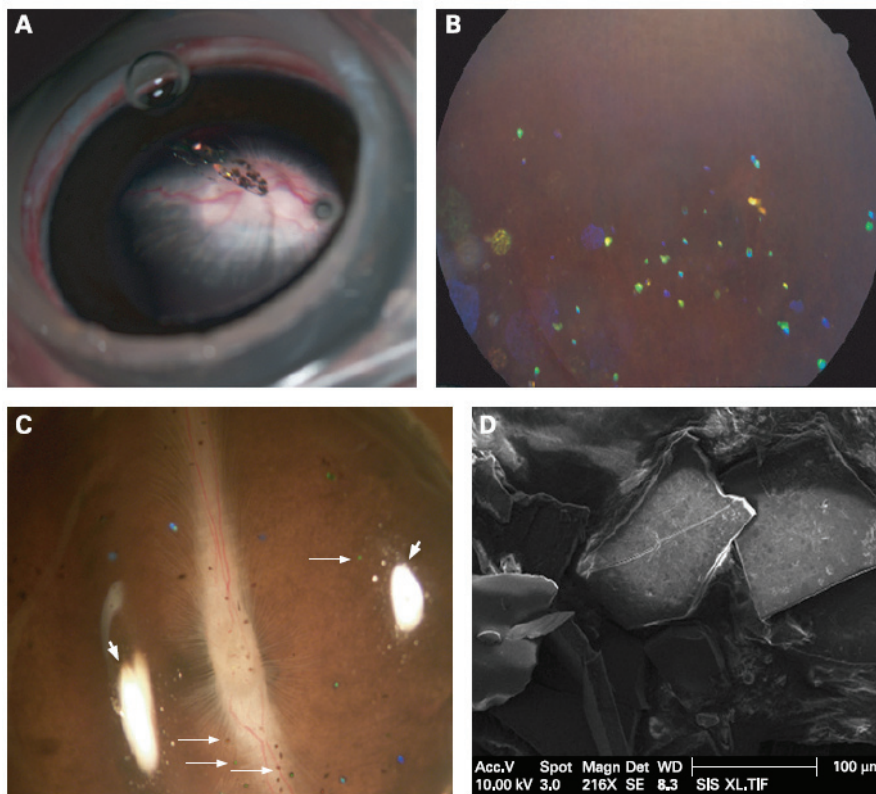


**Figure 1.7 Long term toxicity and degradation of hydrosilylated porous Si particles in the eye (rabbit model).** (a) Photograph taken under a surgical microscope immediately after intravitreal injection of hydrosilylated porous Si particles. Particles can be observed suspended in the centre of the vitreous. (b) Fundus photograph obtained 3 months after injection. The particles are dispersed in the vitreous, and many demonstrated a distinctive blue color corresponding to partial degradation and dissolution. (c) Dissecting microscope image of a rabbit eye cup, with hydrosilylated porous Si particles (small arrows) distributed on a normal-looking retina. Photograph was obtained 4 months after injection. (d) Scanning electron microscope image of the hydrosilylated porous Si particles sampled from a rabbit eye 4 months after intravitreal injection. The sharp edges and pitted surface of the particles indicate a very slow erosion process<sup>33</sup>.

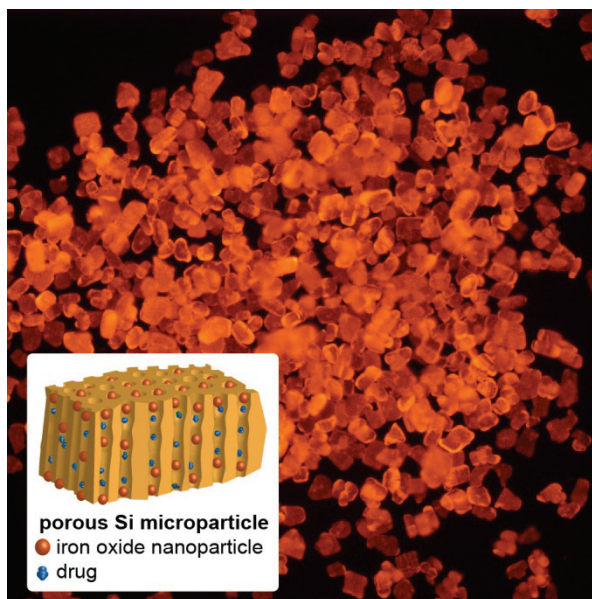


**Figure 1.8 Fluorescence microscopy image of magnetic, luminescent porous silicon microparticles.** The bright orange color is from the intrinsic luminescence of the particles. The insert is a schematic diagram showing the composition of the microparticles.

## **CHAPTER II:**

### **Development of Biodegradable Luminescent Porous Silicon**

#### **Nanoparticles for In Vivo Applications**



## 2.1 Abstract

Nanomaterials that can circulate in the body hold great potential to diagnose and treat disease<sup>1-4</sup>. For such applications, it is important that the nanomaterials be harmlessly eliminated from the body in a reasonable period of time after they perform their diagnostic or therapeutic function. Despite efforts to improve their targeting efficiency, significant quantities of systemically administered nanomaterials are cleared by the mononuclear phagocytic system (MPS) before finding their targets, increasing the likelihood of unintended acute or chronic toxicity. However, there has been little effort to engineer the self-destruction of errant nanoparticles into non-toxic, systemically eliminated products. Here we present luminescent porous silicon nanoparticles (LPSiNP) that can carry a drug payload and whose intrinsic near-infrared (NIR) photoluminescence allows monitoring of both accumulation and degradation *in vivo*. Furthermore, in contrast to most optically active nanomaterials [carbon nanotubes (CNT), gold nanoparticles (GN), and quantum dots (QD)], LPSiNP self-destruct in a mouse model into renally cleared components in a relatively short period of time with no evidence of toxicity. As a preliminary *in vivo* application, we demonstrate tumor imaging using dextran-coated LPSiNP (D-LPSiNP). These results demonstrate a new type of multifunctional nanostructure with a low-toxicity degradation pathway for *in vivo* applications.

## 2.2 Introduction

The *in vivo* use of nanomaterials as therapeutic and diagnostic agents is of intense interest due to their unique properties such as large specific capacity for drug loading<sup>2</sup>,

strong superparamagnetism<sup>3</sup>, efficient photoluminescence<sup>1,5</sup>, or distinctive Raman signatures<sup>4</sup>, among others. Materials with sizes in the range of 20-200 nm can avoid renal filtration, leading to prolonged residence time in the blood stream that allows more effective targeting of diseased tissues. Many biodegradable polymeric nanoparticles that can encapsulate hydrophilic or hydrophobic drugs have been developed for *in vivo* therapeutic applications<sup>2,6-7</sup>, and some of them have been approved for clinical use. However, organic molecule-based nanoparticles generally require the addition of a molecular tag in order to allow *in vivo* monitoring by fluorescence. Although CNT, GN, and QD have demonstrated potential for *in vivo* imaging due to their unique optical properties<sup>1,4,8</sup>, clinical translation has been impeded due to concerns regarding the biodegradability of such materials<sup>4,8-9</sup>, the toxicity of degradation byproducts<sup>10</sup>, or the toxic structural characteristics of the nanomaterials themselves<sup>11</sup>. Although efficient renal clearance can mitigate toxic effects, optimized formulations can leave significant residual heavy metals or other toxic constituents in MPS organs<sup>4,12</sup>. Furthermore, the hydrodynamic size required for renal clearance ( $< 5.5$  nm)<sup>12</sup> may be too small to allow the incorporation of functional components such as multivalent targeting ligands, and rapid renal excretion reduces the time available to the nanomaterial to perform its function. A more desirable design criterion for improving the biocompatibility of nanomaterials would involve the incorporation of controllable rates of self-destruction, through which components could be hierarchically degraded into harmless, renally-cleared products after performing their *in vivo* function.

Electrochemically etched porous silicon has exhibited considerable potential for biological applications due to its biocompatibility<sup>13</sup>, biodegradability<sup>14</sup>, encoding

property for multiplexed detection<sup>15</sup>, and tunable porous nanostructure for drug delivery<sup>16</sup>. Furthermore, since the discovery of photoluminescence of porous silicon in 1990<sup>17</sup>, luminescent (porous) silicon nanoparticles have been produced by several methods<sup>18-22</sup>, some of which are amenable to biological applications<sup>21-22</sup>. For *in vivo* use, silicon nanoparticles provide attractive chemical alternatives to heavy metal-containing QD, which have been shown to be toxic in biological environments<sup>10</sup>. Additionally, silicon is a common trace element in humans and a biodegradation product of porous silicon, orthosilicic acid ( $\text{Si}(\text{OH})_4$ ), is the form predominantly absorbed by humans and is naturally found in numerous tissues. Furthermore, silicic acid administered to humans is efficiently excreted from the body through the urine<sup>23</sup>. In this work, we show that porous silicon nanostructures with intrinsic NIR luminescence can be used for *in vivo* monitoring, they can be loaded with therapeutics, and they can be engineered to resorb *in vivo* into benign components that clear renally within specific timescales (Fig. 2.1a).

### 2.3 Experimental

*Preparation of luminescent porous silicon nanoparticles (LPSiNP):* Porous silicon samples were prepared by electrochemical etch of a single-crystal, (100)-oriented p-type silicon wafer (0.8-1.2  $\text{m}\Omega$  cm, Siltronix) by application of a constant current density of 200  $\text{mA}/\text{cm}^2$  for 150 s in a 3:1 (v/v) electrolyte of 48 % aqueous HF/ethanol. A freestanding film of the porous silicon nanostructure was then removed from the crystalline silicon substrate by application of a current pulse of 4  $\text{mA}/\text{cm}^2$  for 250 s in a solution of 3.3% (by volume) 48 % aqueous HF in ethanol. The freestanding hydrogen-terminated porous silicon film was placed in deionized (DI) water and fractured into

multi-sized particles by sonication overnight. The particles were then filtered through a 0.22  $\mu\text{m}$  filtration membrane (Millipore). The nanoparticles were further incubated in DI water for  $\sim 2$  weeks to activate their luminescence in the near-infrared range. Finally, in order to remove dissolved silicic acids during the activation and obtain porous silicon nanoparticles in a size range of 20-200 nm, the activated nanoparticles were spun down in DI water at 14,000 rpm for 30 min, the supernatant containing silicic acids and smaller nanoparticles ( $< 20$  nm) was removed.

For LPSiNP with different porous nanostructures, porous Si samples were prepared by electrochemical etch of a single-crystal, (100)-oriented p-type silicon wafer (0.8-1.2  $\text{m}\Omega\text{ cm}$ , Siltronix) by application of a constant current density of 50  $\text{mA}/\text{cm}^2$  for 300 s, 200  $\text{mA}/\text{cm}^2$  for 150 s or 400  $\text{mA}/\text{cm}^2$  for 150 s in a 3:1 (v/v) electrolyte of 48 % aqueous HF/ethanol. A freestanding film of the porous silicon nanostructure was then removed from the crystalline silicon substrate by application of a current pulse of 4  $\text{mA}/\text{cm}^2$  for 250 s in a solution of 3.3% (by volume) 48 % aqueous HF in ethanol. The freestanding hydrogen-terminated porous silicon film was placed in deionized (DI) water and fractured into multi-sized particles by sonication overnight. The particles were then filtered through a 0.22  $\mu\text{m}$  filtration membrane (Millipore). The nanoparticles were further incubated in DI water for  $\sim 2$  weeks to activate their luminescence in the near-infrared range. Finally, in order to remove dissolved silicic acid and obtain porous silicon nanoparticles in a size range of 20-200 nm, the activated nanoparticles in DI water were spun down at 14,000 rpm for 30 min, the supernatant containing silicic acid and non-porous smaller nanoparticles ( $< 20$  nm) was removed.

For LPSiNP with different sizes, the particles were then filtered through a 0.45  $\mu\text{m}$  filtration membrane (Millipore) after overnight sonication process. The nanoparticles were further incubated in DI water for  $\sim 2$  weeks to activate their luminescence in the near-infrared range. First, LPSiNP with larger sizes (hydrodynamic size =  $\sim 270.3$  nm) were obtained by centrifugation at low speed (at 6,000 rpm for 10 min) and removal of the supernatant. The nanoparticles were then filtered through a 0.22  $\mu\text{m}$  filtration membrane. Secondly, LPSiNP with medium size (hydrodynamic size =  $\sim 125.7$  nm, which are the LPSiNP used mainly in this study) were obtained by centrifugation at high speed (at 14,000 rpm for 30 min) and removal of the supernatant. Lastly, LPSiNP with smaller size (hydrodynamic size =  $\sim 14.5$  nm) were obtained from the supernatant.

To prepare D-LPSiNP, a dextran coating was applied. A 1 mL aliquot of an aqueous dispersion of 0.5 mg of LPSiNP was mixed with a 1 mL aliquot of water containing 100 mg of dextran (MW  $\sim 20,000$ , Sigma). The mixture was stirred overnight, rinsed three times using a centrifugal filter (100,000 Da molecular weight cut-off, Millipore, inc.), the particles were resuspended in water and then filtered through a 0.22  $\mu\text{m}$  filtration membrane.

*Nanoparticle characterization:* Scanning electron micrographs (SEM) were obtained with a Hitachi S-4800 field-emission instrument. A 20  $\mu\text{L}$  drop of ethanol containing LPSiNP was directly placed onto a polished silicon wafer and the solvent allowed to dry in air. Dynamic light scattering (Zetasizer Nano ZS90, Malvern Instruments) was used to determine hydrodynamic size and zeta potential of LPSiNP or D-LPSiNP (in DI water). To analyze porous nanostructure (pore surface area, pore size,

and pore volume) of LPSiNP, N<sub>2</sub> adsorption isotherms (interpreted with the BJH and BET models) were measured on a Micromeritics Accelerated Surface Area and Prosimetry analyzer (ASAP 2020).

The photoluminescence (PL,  $\lambda_{\text{ex}} = 370$  nm and 460 nm longpass emission filter) and absorbance spectra of LPSiNP or D-LPSiNP in DI water were obtained using a Princeton Instruments/Acton spectrometer fitted with a liquid nitrogen-cooled silicon charge-coupled device detector, and a Hewlett-Packard 8452A UV-vis diode array spectrophotometer, respectively. Fluorescence images of D-LPSiNP in DI water subjected to different excitation wavelength bands were obtained using an IVIS 200 imaging system (Xenogen). (GFP: 445-490 nm and 1 s exposure time, DsRed: 500-550 nm, 2 s exposure time, Cy5.5: 615-665 nm, 8 s exposure time, and ICG: 710-760 nm, 20 s exposure time). The emission filter used was ICG (810-875 nm).

The photostability (photobleaching) of LPSiNP was evaluated relative to organic dyes commonly used in biological imaging (fluorescein, Cy5.5 and Cy7). The LPSiNP and dyes (dispersed or dissolved in aqueous solution) were illuminated with a 100 W mercury lamp, and fluorescence intensities were monitored using a fluorescence microscope (Nikon Eclipse LV150) equipped with a thermoelectrically cooled CCD camera (Photometrics CoolSNAP HQ<sup>2</sup>). Excitation ( $355 \pm 25$  nm for LPSiNP,  $480 \pm 20$  nm for Fluorescein,  $650 \pm 22$  nm for Cy5.5, and  $710 \pm 35$  nm for Cy7) and emission (435 nm long pass for LPSiNP,  $535 \pm 25$  nm for Fluorescein,  $710 \pm 25$  nm for Cy5.5, and  $800 \pm 35$  nm for Cy7) were used for these experiments. The fluorescence intensities were monitored at 0.5 or 1 min intervals. The quantum yield (QY) of LPSiNP in ethanol was measured using the comparative method, using Rhodamine 101 (QY = 100%, Sigma) in

ethanol as the standard. The Fourier-transform infrared (FTIR) spectra of as-etched porous silicon films and LPSiNP were obtained in the absorption mode using a Thermo Scientific Nicolet 6700 FTIR spectrometer equipped with a diamond Attenuated Total Reflectance (ATR) accessory.

*In vitro degradation:* A series of samples containing 0.05 mg/mL of LPSiNP or D-LPSiNP in 1 mL of PBS solution were incubated at 37 °C. An aliquot of 0.5 mL of solution was removed at different time points and filtered with a centrifugal filter (30,000 Da molecular weight cut-off, Millipore, inc.) to remove undissolved LPSiNP. 0.4 mL of the filtered solution was diluted with 4.6 mL HNO<sub>3</sub> (2 %(v/v)) and subjected to analysis by inductively coupled plasma optical emission spectroscopy (ICP-OES, Perkin Elmer Optima 3000DV). The silicon concentration in the original solution was determined by incubating the solution in PBS at 37 °C for 72 h and measuring the silicon concentration without filtration. The decrease in PL of the above samples over time was also monitored.

*Drug loading and cytotoxicity:* 0.5 mg LPSiNP (0.5 mg/mL) was mixed with 0.05 mg doxorubicin (DOX, Sigma) in DI water at room temperature overnight and then rinsed three times using a centrifugal filter (100,000 Da molecular weight cut-off, Millipore, inc.). The amount of DOX incorporated into LPSiNP was determined by incubating DOX-loaded LPSiNP (DOX-LPSiNP) in a 0.3 M HCl 70% ethanol solution overnight and comparing the fluorescence with a standard curve (~ 43.8 µg DOX per 1 mg LPSiNP). Release kinetics of DOX from DOX-LPSiNP (0.05 mg/mL) in PBS at 37°C was measured by filtering out DOX-LPSiNP from the solution at each time point

using the centrifugal filter and measuring fluorescence of free DOX left in the solution at 590 nm ( $\lambda_{\text{ex}} = 480$  nm).

For drug-mediated cytotoxicity experiments, MDA-MB-435 human carcinoma cells were incubated with LPSiNP, DOX-LPSiNP or free DOX (at different DOX/LPSiNP concentrations) for 48 h and rinsed with cell medium three times. The cytotoxicity of LPSiNP, DOX-LPSiNP or free DOX was evaluated using the MTT assay (Chemicon). For nanostructure- or size-related cytotoxicity experiments (without DOX), HeLa cells were incubated with the LPSiNP (at different LPSiNP concentrations) for 48 h and rinsed with cell medium (no phenol red) three times. The cytotoxicity of LPSiNP was evaluated using the Calcein assay [fluorogenic intracellular esterase sensor Calcein acetoxymethylester (Calcein AM), Invitrogen]. Cell viability was expressed as the percentage of viable cells compared with controls (cells treated with PBS). The cytotoxicity of the LPSiNP was also examined by observing morphology of live cells using an inverted optical microscope (Nikon).

*In vitro fluorescence imaging:* HeLa cells (3000 cells per well) were seeded into 8-well chamber glass slides (Lab-Tek) and incubated overnight. A 50  $\mu\text{g}$  per well quantity of LPSiNP was added and the cells incubated for 2 h at 37 °C in the presence of 10% fetal bovine serum (FBS). The cells were then rinsed three times with cell medium, fixed with 4% paraformaldehyde for 20 min and then observed in the fluorescence microscope (370 nm or 488 nm excitation and 650 nm long pass emission filter) and in the Radiance 2100/AGR-3Q BioRad Multi-photon Laser Point Scanning Confocal Microscope. For confocal fluorescence microscopy, the cells treated with LPSiNP were



imaged using 488 nm Ar ion laser excitation and a 650 nm long pass emission filter. For multi-photon fluorescence microscopy, the cells treated with LPSiNP were imaged using 750 nm Mai-Tai laser excitation. The DAPI and LPSiNP signals were separated using 495 dichroic filter and 560 nm long pass filter.

*In vivo degradation, toxicity, and circulation:* All animal work was performed in accordance with the institutional animal protocol guidelines in place at the Burnham Institute for Medical Research, and it was reviewed and approved by the Institute's Animal Research Committee. LPSiNP or D-LPSiNP (in 200  $\mu$ L PBS solution) were intravenously injected into BALB/c mice at a dose of 20 mg/kg body mass. For *in vivo* degradation studies, the mice were sacrificed 1 day, 1 week and 4 weeks after injection by cardiac perfusion with PBS under anesthesia, and the brain, heart, kidney, liver, lung, and spleen were collected. The tissues were weighed and then digested with a solution of HNO<sub>3</sub> (0.5 mL, ~15.7 M), H<sub>2</sub>O<sub>2</sub> (0.1 mL, 30%) and HF (0.03 mL, 5%) for 2 days. A solution of H<sub>3</sub>BO<sub>3</sub> (0.235 mL, 0.4 M) was added and the mixture diluted with HNO<sub>3</sub> (10.50 mL, 2%). The silicon concentration in the samples was determined using ICP-OES.

For the *in vivo* toxicity studies, the mass of each mouse was monitored for 4 weeks after injection and compared with control mice (PBS-injected). The sections of kidney, liver, and spleen tissues harvested from the mice 1 day and 4 weeks after injection were stained with haematoxylin and eosin and then examined by a pathologist. To determine blood half-lives, the blood (100  $\mu$ L) was collected from the periorbital plexus at several different times after injection using heparinized capillary tubes (Fisher),

and then immediately mixed with 100  $\mu$ L of 10 mM EDTA (in PBS) to prevent coagulation. The blood samples were digested and prepared as mentioned above for the organs. The total silicon concentration in the blood was measured using ICP-OES.

*In vivo fluorescence imaging:* Aliquots of LPSiNP (20  $\mu$ L of 0.1 mg/mL in PBS) were injected subcutaneously and intramuscularly into the left and right flank, respectively, of a nude mouse, and imaged immediately with GFP excitation (445-490 nm) and ICG emission filter (810-875 nm) using the IVIS 200 imaging system.

For systemic administration, LPSiNP or D-LPSiNP (in 200  $\mu$ L PBS) were intravenously injected into nude mice at a dose of 20 mg/kg body mass. The mice were imaged under anesthesia several different times after injection using the IVIS 200 imaging system. The organs (bladder, brain, heart, kidney, lymph nodes, liver, lung, skin, and spleen), harvested 24 h after injection, were also imaged. For *in vivo* fluorescence tumor imaging, the nude mouse bearing an MDA-MB-435 human carcinoma tumor (~0.5 cm, one side of flank) was used. The tumor area was imaged under anesthesia several different times after intravenous injection of D-LPSiNP at a dose of 20 mg/kg body mass using the IVIS 200 imaging system. The tumor and muscle around the tumor harvested 24 h after injection, were also imaged. The excitation filter used was Cy5.5 (615-665 nm). The emission filter used was ICG (810-875 nm). For fluorescent histological analysis, sections of liver, spleen, and tumor tissues were fixed with 4% paraformaldehyde, stained with DAPI, and then observed with 370 nm excitation and 650 nm long pass emission filter using the fluorescence microscope.

## 2.4 Results and Discussion

Luminescent porous Si nanoparticles (LPSiNP) were prepared by electrochemical etching of single-crystal silicon wafers in ethanolic HF solution, lift-off of the porous silicon film, ultrasonication, filtration of the formed particles through a 0.22  $\mu\text{m}$  filtration membrane and finally activation of luminescence in an aqueous solution (Fig. 2.2). During the activation step, silicon oxide grows on the hydrogen-terminated porous silicon surface, generating significant luminescence attributed to quantum confinement effects and to defects localized at the Si/SiO<sub>2</sub> interface (Fig. 2.3 and 2.4)<sup>5,18-19</sup>. The preparation conditions were optimized to provide pore volume and surface area suitable for loading of therapeutics and long *in vivo* circulation times while maintaining an acceptable degradation rate (Fig. 2.5 and 2.6). As a result, the medium-sized (126 nm) particles prepared by electrochemical etching at 200 mA/cm<sup>2</sup> for 150 s were chosen for the study presented here. The LPSiNP appear spherical and fairly uniform in the scanning electron microscope (SEM), with a well-defined micro- and meso-porous nanostructure (Fig. 2.1b). The pore diameters are on the order of 5~10 nm (Fig. 2.5a and 2.5b). The mean hydrodynamic size measured by dynamic light scattering (DLS) is ~126 nm, consistent with the SEM measurements.

The intrinsic photoluminescence of LPSiNP under UV excitation appears at wavelengths between 650 and 900 nm (Fig. 2.1c), suitable for *in vivo* imaging due to low tissue adsorption in this spectral range<sup>24</sup>. The materials display greater photostability relative to fluorescein or the well-known NIR cyanine fluorophores, Cy5.5 and Cy7 (Fig. 2.7). The quantum yield of LPSiNP in ethanol was determined to be ~10.2 % (relative to Rhodamine 101 standard) (Fig. 2.8), which is in accord with previously reported values

for other water-soluble luminescent silicon/silica nanoparticles<sup>21-22</sup>. When placed in biological solution (phosphate buffered saline, PBS, pH 7.4, 37 °C) at a mass concentration less than the solubility of silicic acid (0.1~0.2 mg/mL SiO<sub>2</sub>)<sup>25</sup>, LPSiNP lose their luminescence in a short time and dissolve (Fig. 2.1d). A blue-shift of the luminescence spectrum during degradation is indicative of a shrinking in size of the semiconductor fluorophore (Fig. 2.9). No detectable (by DLS) LPSiNP remain after 8 h of incubation. However, degradation is slowed by addition of a molecular or polymeric surface coating (see below).

The anti-cancer drug doxorubicin (DOX) was incorporated into the LPSiNP (DOX-LPSiNP, ~ 43.8 ug DOX per 1 mg LPSiNP) to test their potential for therapeutic applications. The positively charged DOX molecules are bound to the negatively charged porous SiO<sub>2</sub> surface by electrostatic forces. Loading of DOX increases the zeta potential of the nanoparticles from -52 mV to -39 mV. A relatively slow release of the drug is observed at physiological pH and temperature, reaching significant levels within 8 h (Fig. 2.1e). The appearance of free silicic acid in solution as a function of time, indicative of degradation of the LPSiNP, correlates with the DOX release profile. The rate of degradation of DOX-LPSiNP is somewhat slower than bare LPSiNP. We postulate that the presence of DOX molecules inhibits the nanoparticle dissolution process by slowing the rate of SiO<sub>2</sub> hydrolysis at the LPSiNP surface. DOX-LPSiNP exhibit similar or slightly greater cytotoxicity relative to free DOX, while bare LPSiNP show no significant cytotoxicity (Fig. 2.1f).

Next, we tested biodegradability and biocompatibility of LPSiNP *in vitro* and *in vivo*. The LPSiNP formulation is relatively non-toxic to HeLa cells *in vitro* within the

tested concentration range (Fig. 2.5e, 2.6c, 2.10a and 2.11). For *in vivo* studies, LPSiNP (20 mg/kg) were injected intravenously into mice. As with many other nanomaterials<sup>3-4,12</sup>, the injected LPSiNP accumulate mainly in the MPS-related organs such as the liver and the spleen (Fig. 2.10b). However, the LPSiNP accumulated in the organs are noticeably cleared from the body within a period of 1 week and completely cleared in 4 weeks. The mechanism of clearance is attributed to degradation into soluble silicic acid followed by excretion. This result contrasts with the slow clearance generally observed for other types of inorganic nanoparticles with diameters  $> 5.5$  nm<sup>4,8-9</sup>. Over a period of 4 weeks, the body weight of the mice injected with LPSiNP increased slightly in a pattern similar to the control mice (Fig. 2.10c), indicating that the mice continue to mature without any significant toxic effects.

Since the degradation of highly localized LPSiNP may induce subsequent damage in the organs related to nanoparticle clearance, *in vivo* toxicity of LPSiNP was further examined in kidney, liver, and spleen tissues of mice 1 day and 4 weeks after LPSiNP injection. Histopathologically, no significant toxicity was observed in these tissues relative to the controls (Fig. 2.10d). Hepatocytes in the liver samples appeared unremarkable, and there were no inflammatory infiltrates. However, the sinusoids in between the rows of hepatocytes contained Kupffer cells (macrophages) that appeared swollen 1 day after injection. The cells returned to the normal morphology 4 weeks after injection, implying that LPSiNP were taken up, degraded (presumably by lysosomes), and the soluble products were subsequently released from the cells. Spleen samples showed no significant change in morphology of the lymphoid follicles or in the size of the red pulp after LPSiNP injection. Kidney samples also showed no remarkable change

in the morphology. Although the *in vivo* toxicity results shown here are preliminary, the LPSiNP show promise as non-toxic biodegradable inorganic nanomaterials.

We next investigated the possibility of imaging cells *in vitro* and organs *in vivo* using the intrinsic photoluminescent properties of LPSiNP. Significant luminescence of LPSiNP was observed in HeLa cells using excitation wavelengths of 370 nm, 488 nm, and 750 nm (two-photon excitation) 2 hr after incubation, attributed to non-specific cellular uptake of the silica-based nanomaterials<sup>26</sup> (Fig. 2.12a and 2.13). To examine their potential for *in vivo* imaging, subcutaneous and intramuscular injections of LPSiNP dispersions (20  $\mu$ L aliquots, 0.1 mg/mL) into the left and right flank of a nude mouse, respectively, were administered. The mouse was imaged in a fluorescence mode (GFP excitation filter, 445-490 nm and ICG emission filter, 810-875 nm). The signals from both injections were clearly observed without any skin autofluorescence although the near-skin fluorescence intensity is larger than the signal emanating from deeper tissue (Fig. 2.12b). The fluorescence spectrum of LPSiNP allows imaging in the NIR-emission range, a convenient window for *in vivo* imaging due to the low levels of NIR autofluorescence of mouse skin excited with visible light<sup>1,27</sup>.

We next examined whole-body fluorescence imaging of nude mice using LPSiNP administered by intravenous injection. To prevent rapid degradation after injection and to increase their blood half-life, LPSiNP were coated with the biopolymer dextran by physisorption<sup>28</sup> (D-LPSiNP, Fig. 2.14). The coating process increased the size and zeta potential of the nanoparticles (from 125 nm to 151 nm and from -52 mV to -43.5 mV, respectively). Bare LPSiNP or D-LPSiNP were injected and imaged at different time points (Fig. 2.12c, 2.12d, and 2.12e). A significant fraction of the bare LPSiNP were

immediately removed by renal clearance, presumably due to their degradation into smaller (< 5.5 nm) nanoparticles<sup>12</sup>. The remaining nanoparticles were observed to accumulate in the liver and the spleen, consistent with the histology data discussed above.

The D-LPSiNP exhibit a somewhat different pattern in their uptake by the MPS-related organs. These nanoparticles accumulate and degrade in the liver slowly relative to bare LPSiNP, which is consistent with the *in vitro* degradation and *in vivo* blood half-life data (Fig. 2.14c and 2.14d). Biodistribution and histological studies of the organs harvested from the same mice 24 h after injection are consistent with the whole-body fluorescence imaging data (liver < spleen for LPSiNP and liver > spleen for D-LPSiNP) (Fig. 2.12f and 2.12g). These results indicate that the intrinsic luminescent properties of LPSiNP allow the non-invasive monitoring of their biodistribution and degradation in a live animal as well as the microscopic observation of their localization in the organs.

Lastly, we evaluated the potential of LPSiNP to image tumors *in vivo*. In order to detect and image deep-tissue diseases such as tumors by fluorescence, the excitation wavelength for the nanoparticle should be in the NIR range in order to maximize tissue penetration and minimize optical absorption by physiologically abundant species such as hemoglobin<sup>24</sup>. LPSiNP emit in the NIR (810-875 nm) and they can be excited with red or NIR radiation (615-665 nm or 710-760 nm) (Fig. 2.15a) or by two-photon NIR excitation (Fig. 2.13). Similar to some of the NIR-emitting semiconductor QD<sup>27</sup>, the quantum efficiency of LPSiNP decreases with longer excitation wavelengths. However, the quantum yield is sufficient to allow their observation in internal organs using a conventional fluorescence imaging system.

Injection of the D-LPSiNP formulation (20 mg/kg) into a nude mouse bearing an MDA-MB-435 tumor results in passive accumulation of the nanomaterial in the tumor, as revealed in the NIR fluorescence image (Fig. 2.15b). The *ex vivo* fluorescence images and histology confirm the presence of D-LPSiNP in the tumor (Fig 2.15c and 2.15d).

## 2.5 Conclusions

This study represents the first example of the imaging of a tumor and other organs using biodegradable silicon nanoparticles in live animals, and it is important because of the biodegradability and low *in vivo* toxicity observed. The LPSiNP injected intravenously are observed to accumulate mainly in MPS-related organs and are degraded *in vivo* into apparently non-toxic products within a few days and removed from the body through renal clearance. These larger (100 nm-scale) silicon-based biodegradable nanoparticles overcome many of the disadvantages of smaller (< 5.5 nm) nanocrystals<sup>12</sup> such as fast clearance from circulation, low capacity for drug loading, and toxicity of the residual particles that do not escape MPS uptake<sup>4,12</sup>. We believe the reduced *in vivo* toxicity of this multifunctional inorganic nanomaterial provides a promising pathway for clinical translation.

## 2.6 References

1. Gao, X.H., Cui, Y.Y., Levenson, R.M., Chung, L.W.K. & Nie, S.M. In vivo cancer targeting and imaging with semiconductor quantum dots. *Nat. Biotechnol.* **22**, 969-976 (2004).
2. Torchilin, V.P. Recent advances with liposomes as pharmaceutical carriers. *Nat. Rev. Drug Disc.* **4**, 145-160 (2005).



3. Lee, J.H. et al. Artificially engineered magnetic nanoparticles for ultra-sensitive molecular imaging. *Nat. Med.* **13**, 95-99 (2007).
4. Liu, Z. et al. Circulation and long-term fate of functionalized, biocompatible single-walled carbon nanotubes in mice probed by Raman spectroscopy. *Proc. Natl. Acad. Sci. USA* **105**, 1410-1415 (2008).
5. Godefroy, S. et al. Classification and control of the origin of photoluminescence from Si nanocrystals. *Nature Nanotech.* **3**, 174-178 (2008).
6. Sengupta, S. et al. Temporal targeting of tumour cells and neovasculature with a nanoscale delivery system. *Nature* **436**, 568-572 (2005).
7. Farokhzad, O.C. et al. Targeted nanoparticle-aptamer bioconjugates for cancer chemotherapy in vivo. *Proc. Natl Acad. Sci. USA* **103**, 6315-6320 (2006).
8. Kim, D., Park, S., Lee, J.H., Jeong, Y.Y. & Jon, S. Antibiofouling polymer-coated gold nanoparticles as a contrast agent for in vivo X-ray computed tomography imaging. *J. Am. Chem. Soc.* **129**, 7661-7665 (2007).
9. Ballou, B., Lagerholm, B.C., Ernst, L.A., Bruchez, M.P. & Waggoner, A.S. Noninvasive imaging of quantum dots in mice *Bioconjugate Chem.* **15**, 79-86 (2004).
10. Derfus, A.M., Chan, W.C.W. & Bhatia, S.N. Probing the cytotoxicity of semiconductor quantum dots. *Nano Lett.* **4**, 11-18 (2004).
11. Poland, C.A. et al. Carbon nanotubes introduced into the abdominal cavity of mice show asbestos-like pathogenicity in a pilot study. *Nat. Nanotech.* **3**, 423-428 (2008).
12. Choi, H.S. et al. Renal clearance of quantum dots. *Nat. Biotechnol.* **25**, 1165-1170 (2007).
13. Bayliss, S.C., Heald, R., Fletcher, D.I. & Buckberry, L.D. The culture of mammalian cells on nanostructured silicon. *Adv. Mater.* **11**, 318-321 (1999).
14. Canham, L.T. Bioactive silicon structure fabrication through nanoetching techniques. *Adv. Mater.* **7**, 1033-1037 (1995).
15. Cunin, F. et al. Biomolecular screening with encoded porous-silicon photonic crystals. *Nat. Mater.* **1**, 39-41 (2002).
16. Salonen, J., Kaukonen, A.M., Hirvonen, J. & Lehto, V.-P. Mesoporous silicon in drug delivery applications. *J. Pharm. Sci.* **97**, 632-653 (2008).
17. Canham, L.T. Silicon quantum wire array fabrication by electrochemical and chemical dissolution of wafers. *Appl. Phys. Lett.* **57**, 1046-1048 (1990).

18. Heinrich, J.L., Curtis, C.L., Credo, G.M., Kavanagh, K.L. & Sailor, M.J. Luminescent colloidal silicon suspensions from porous silicon. *Science* **255**, 66-68 (1992).
19. Wilson, W.L., Szajowski, P.F. & Brus, L.E. Quantum confinement in size-selected surface-oxidized silicon nanocrystals. *Science* **262**, 1242-1244 (1993).
20. Mangolini, L. & Kortshagen, U. Plasma-assisted synthesis of silicon nanocrystal inks. *Adv. Mater.* **19**, 2513-2519 (2007).
21. Wang, L., Reipa, V. & Blasic, J. Silicon nanoparticles as a luminescent label to DNA. *Bioconjugate Chem.* **15**, 409-412 (2004).
22. Li, Z.F. & Ruskenstein, E. Water-soluble poly(acrylic acid) grafted luminescent silicon nanoparticles and their use as fluorescent biological staining labels. *Nano Lett.* **4**, 1463-1467 (2004).
23. Popplewell, J.F. et al. Kinetics of uptake and elimination of silicic acid by a human subject: A novel application of  $^{32}\text{Si}$  and accelerator mass spectrometry. *J. Inorg. Biochem.* **69**, 177-180 (1998).
24. Weissleder, R. A clearer vision for in vivo imaging. *Nature Biotech.* **19**, 316-317 (2001).
25. Piryutko, M.M. The solubility of silicic acid in salt solutions. *Russ. Chem. Bull.* **8**, 355-360 (1959).
26. Slowing, I., Trewyn, B.G. & Lin, V.S.-Y. Effect of surface functionalization of MCM-41-type mesoporous silica nanoparticles on the endocytosis by human cancer cells. *J. Am. Chem. Soc.* **128**, 14792-14793 (2006).
27. Kim, S. et al. Near-infrared fluorescent type II quantum dots for sentinel lymph node mapping. *Nat. Biotechnol.* **22**, 93-97 (2003).
28. Suh, K.Y. et al. Characterization of chemisorbed hyaluronic acid directly immobilized on solid substrates. *J. Biomed. Mater. Res. B Appl. Biomater.* **15**, 292-298 (2006).

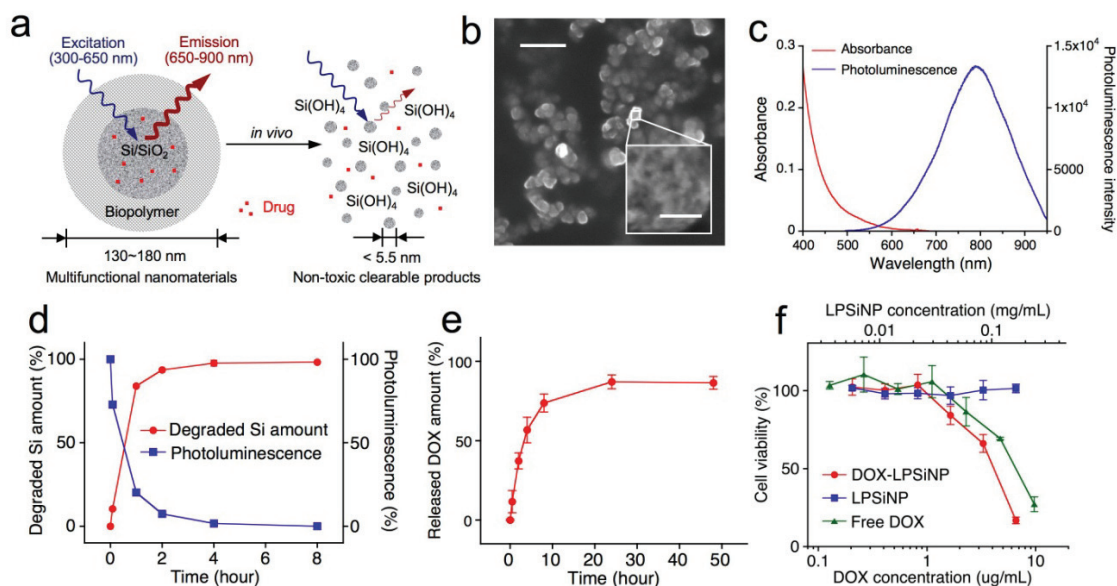


**Figure 2.1 Characterization of luminescent porous Si nanoparticles (LPSiNP).** (a) Schematic depicting the structure and *in vivo* degradation process for the (biopolymer-coated) nanoparticles used in this study. (b) Scanning electron microscope image of LPSiNP (inset shows the porous nanostructure of one of the nanoparticles). Scale bar is 500 nm (50 nm for the inset). (c) Photoluminescence (PL) emission and absorbance spectra of LPSiNP. PL is measured using UV excitation ( $\lambda = 370$  nm). (d) Appearance of silicon in solution (by ICP-OES) and photoluminescence intensity ( $\lambda_{\text{ex}} = 370$  nm and  $\lambda_{\text{em}} = \text{maximum peak intensity at each time point}$ ) from a sample of LPSiNP (50  $\mu\text{g}/\text{mL}$ ) incubated in PBS solution at 37°C as a function of time. (e) Release profile depicting percent of doxorubicin (DOX) from DOX-loaded LPSiNP (DOX-LPSiNP) released into a PBS solution as a function of time at 37 °C. Data were obtained by filtering out DOX-LPSiNP from the solution at each time point using a centrifugal filter and measuring the fluorescence intensity of free DOX left in solution ( $\lambda_{\text{em}} = 590$  nm  $\lambda_{\text{ex}} = 480$  nm). Error bars indicate s.d. (f) Cytotoxicity of DOX-LPSiNP, bare LPSiNP, and free DOX towards MDA-MB-435 human carcinoma cells, quantified by MTT assay. The cells were incubated with the samples for 48 h.

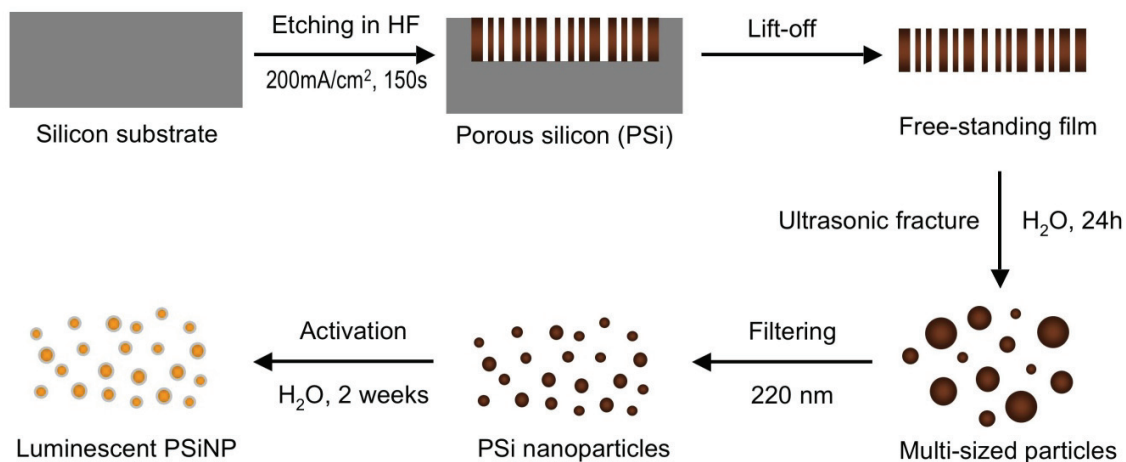


**Figure 2.2 Schematic diagram of the synthesis of luminescent porous silicon nanoparticles (LPSiNP).** A porous silicon layer with a pore size range of 5-10 nm is first etched into the single-crystal silicon substrate in ethanolic HF solution. The entire porous nanostructure is removed from the Si substrate by application of a current pulse. The freestanding hydrogen-terminated porous silicon film is then placed in an aqueous solution and fractured into multi-sized particles by overnight ultrasonication. The particles are then filtered through a 0.22  $\mu\text{m}$  porous filtration membrane to obtain the porous silicon nanoparticles. Finally, the nanoparticles are incubated in an aqueous solution to activate their luminescence.

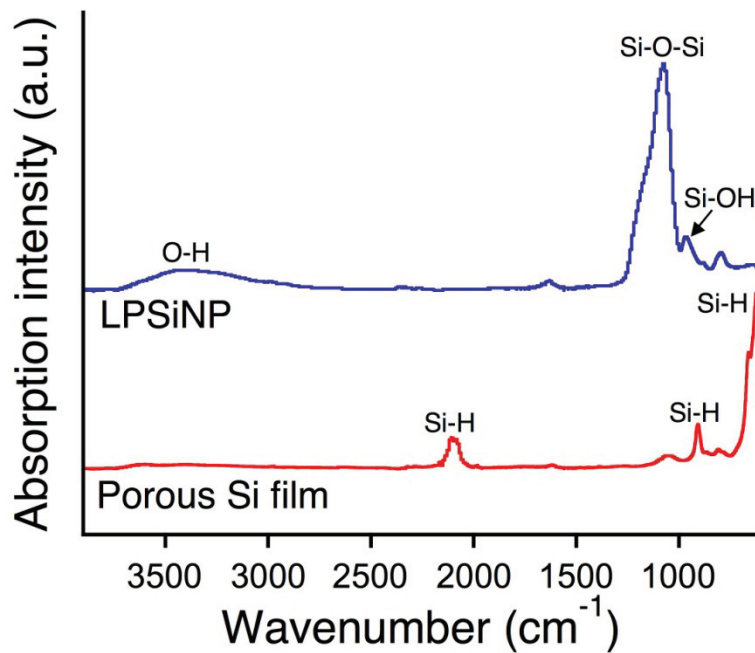


**Figure 2.3** FTIR spectra of porous silicon film and luminescent porous silicon nanoparticles (LPSiNP) shown in Fig. 2.2. The hydrogen-terminated surface of the as-etched porous silicon film is converted to silicon dioxide in the porous silicon nanoparticles. The oxide layer passivates the nanoparticle surface and also generates interfacial oxides, giving rise to a strong NIR photoluminescence.

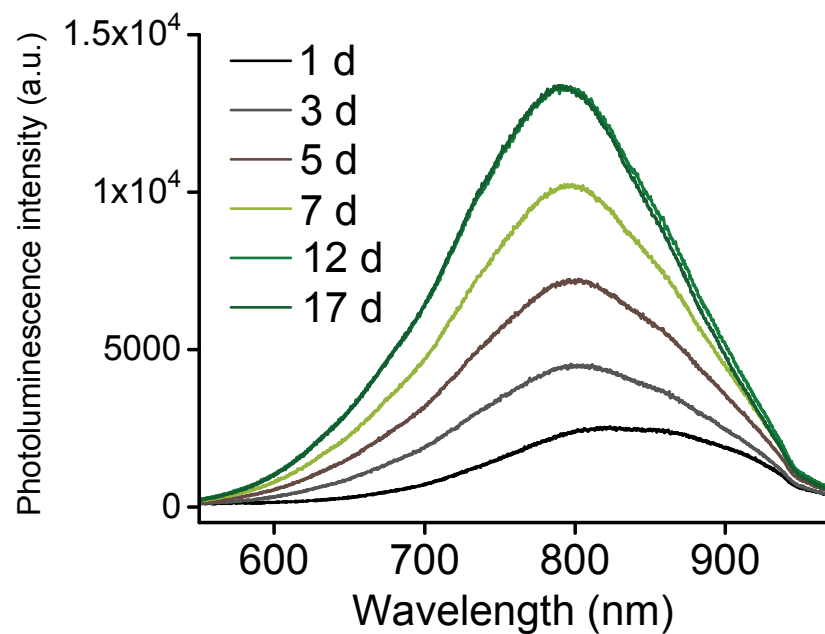


**Figure 2.4 Photoluminescence spectra of LPSiNP.** The spectra were acquired during activation of LPSiNPs in deionized (DI) water at room temperature (1 d indicates 1 day after immersion in DI water). Note the increase in PL intensity and slight blue-shifting of the peak maximum with time.

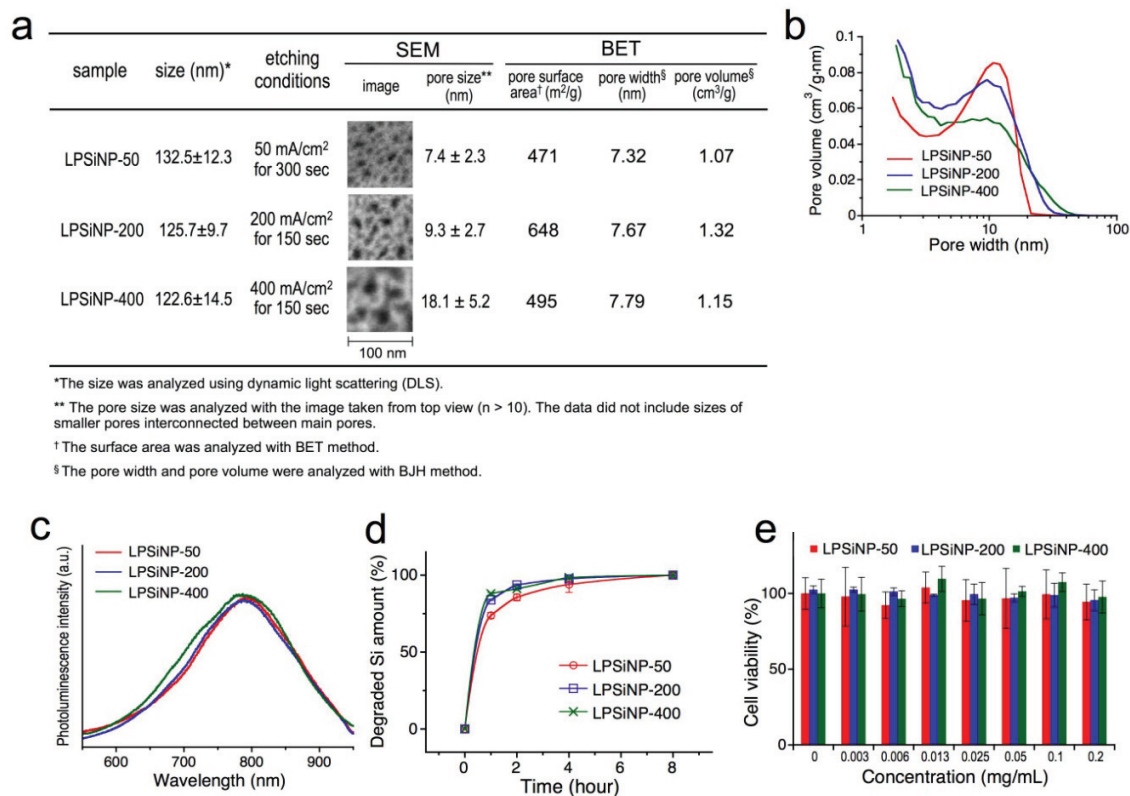


**Figure 2.5 Characterization of three types of LPSiNP prepared with different porous nanostructures.** (a) Analysis of porous nanostructures of LPSiNP by SEM and gas adsorption (BET/BJH) methods. The particle size values (by Dynamic Light Scattering, DLS) are the means plus/minus one standard deviation for three batches of LPSiNP, and the pore size values (by SEM) are averages of > 10 different pores from randomly selected LPSiNP. (b) Pore size distributions and pore volume in LPSiNP determined by gas adsorption (BJH and dV/dw methods). (c) Photoluminescence spectra of LPSiNP ( $\lambda_{\text{ex}} = 370 \text{ nm}$ ). (d) *In vitro* degradation of LPSiNP in PBS solution at  $37^\circ\text{C}$  as a function of time. Note that LPSiNP prepared using the etching condition with a current density of  $50 \text{ mA/cm}^2$  show slightly slower degradation relative to the other two preparations of LPSiNP, suggesting that their lower porosity may be responsible for the slower degradation. (e) Cytotoxicity of LPSiNP by calcein assay. HeLa cells were incubated with LPSiNP for 48 h and then viability was evaluated using the fluorogenic intracellular esterase sensor calcein acetoxymethyl ester (Calcein AM).

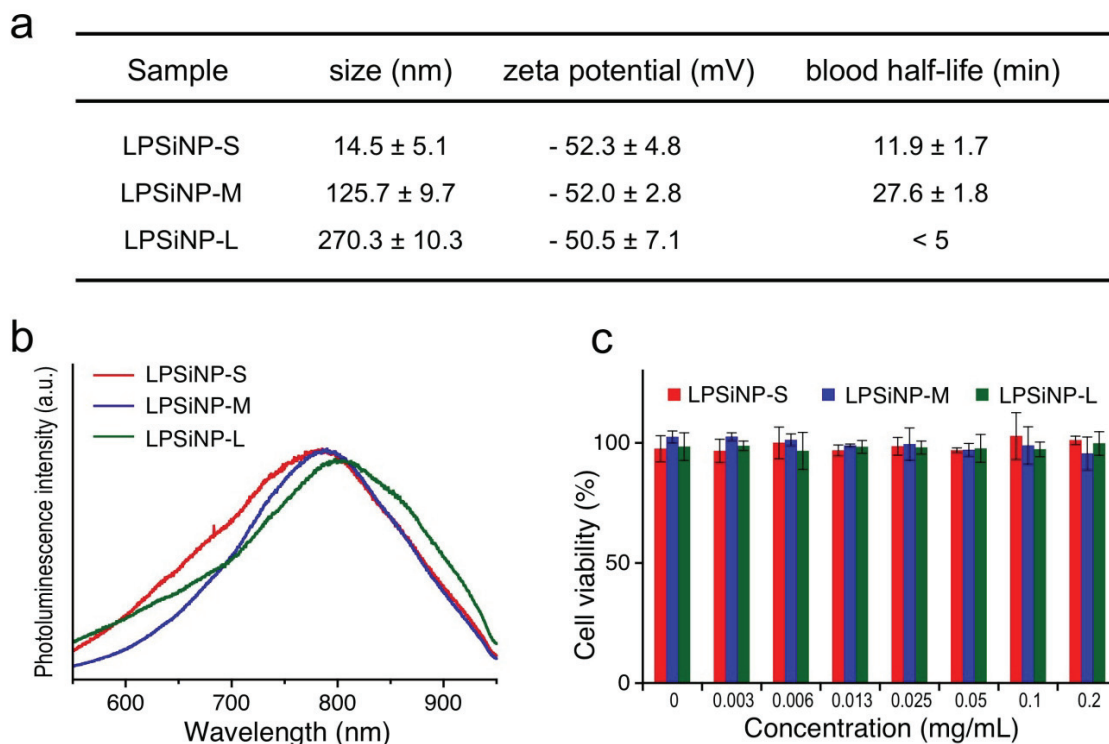


**Figure 2.6 Characterization of LPSiNP with different average particle sizes, prepared using the same etching conditions (200 mA/cm<sup>2</sup> for 150 sec).** The suffixes “-S” “-M” and “-L” refer to small (15 nm), medium (126 nm), and large (270 nm) particles. (a) Effect of nanoparticle size on the blood circulation half-life in mouse (n = 3). Note that the LPSiNP-M show the longest circulation times relative to LPSiNP with other sizes. The LPSiNP-S are cleared rapidly by the kidney due to their small size (close to the typical renal clearance range of < 5.5 nm) while the LPSiNP-L are cleared rapidly by the spleen or lung non-specifically due to their large size. The size and zeta potential values obtained by DLS are the means plus/minus one standard deviation for three lots of LPSiNP. The blood half-life values were obtained by fitting the concentration of silicon in each blood sample at each time point to a single-exponential equation using a one-compartment open pharmacokinetic model<sup>1</sup>. (b) Photoluminescence spectra of the LPSiNP with different sizes ( $\lambda_{\text{ex}} = 370 \text{ nm}$ ). (c) Cytotoxicity of the LPSiNP with different sizes by Calcein assay. HeLa cells were incubated with LPSiNP for 48 h and then their viability was evaluated using the fluorogenic intracellular esterase sensor Calcein acetoxymethylester (Calcein AM).



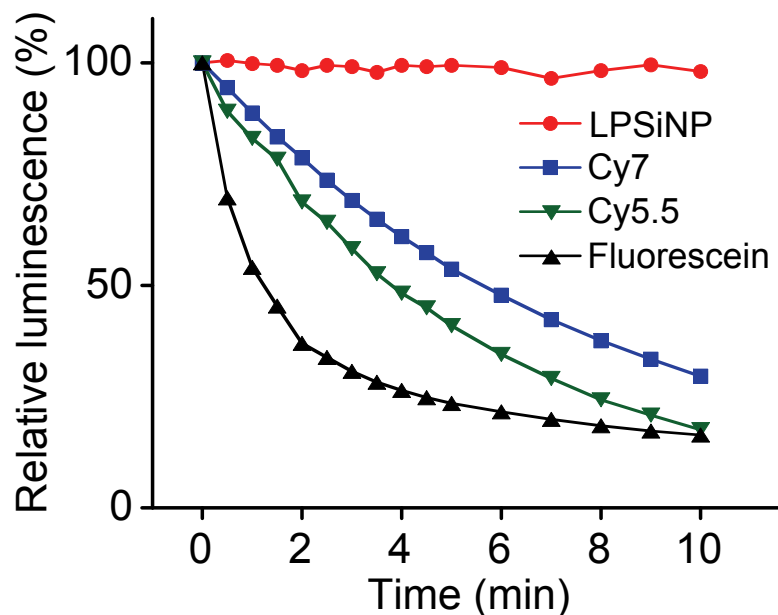


**Figure 2.7 Photostability of LPSiNP compared to conventional fluorophores.** Changes in fluorescence intensity of LPSiNP dispersed in aqueous solution exposed to air during continuous exposure to a 100 W mercury lamp, compared with organic dyes commonly used in biological imaging experiments (Cy5.5, Cy7, and fluorescein). Excitation wavelengths of  $355 \pm 25$  nm for LPSiNP,  $480 \pm 20$  nm for fluorescein,  $650 \pm 22$  nm for Cy5.5, and  $710 \pm 35$  nm for Cy7, and emission wavelengths of 435 nm (long pass) for LPSiNP,  $535 \pm 25$  nm for fluorescein,  $710 \pm 25$  nm for Cy5.5, and  $800 \pm 35$  nm for Cy7 were used for these experiments. The fluorescence intensities were monitored with a thermoelectrically cooled CCD camera.

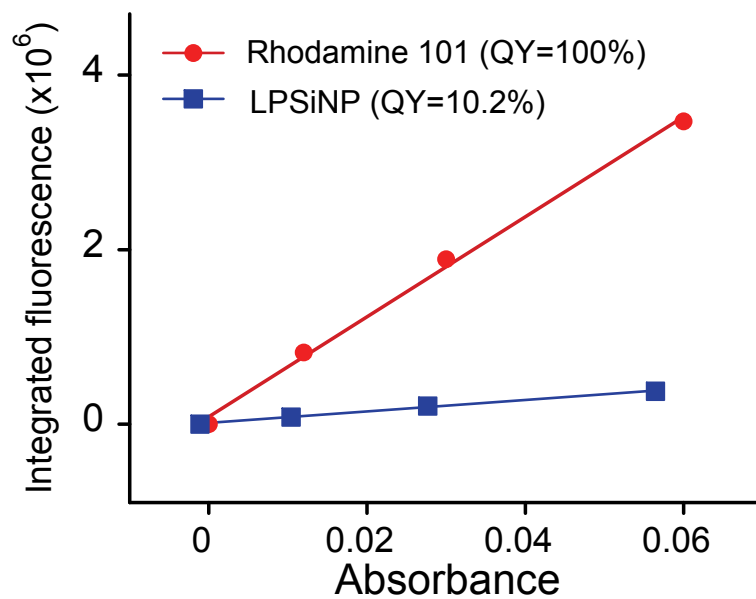


**Figure 2.8 Quantum yield (QY=10.2%) of luminescent porous Si nanoparticles (LPSiNP) compared to Rhodamine 101 (QY=100%)<sup>2</sup>.**

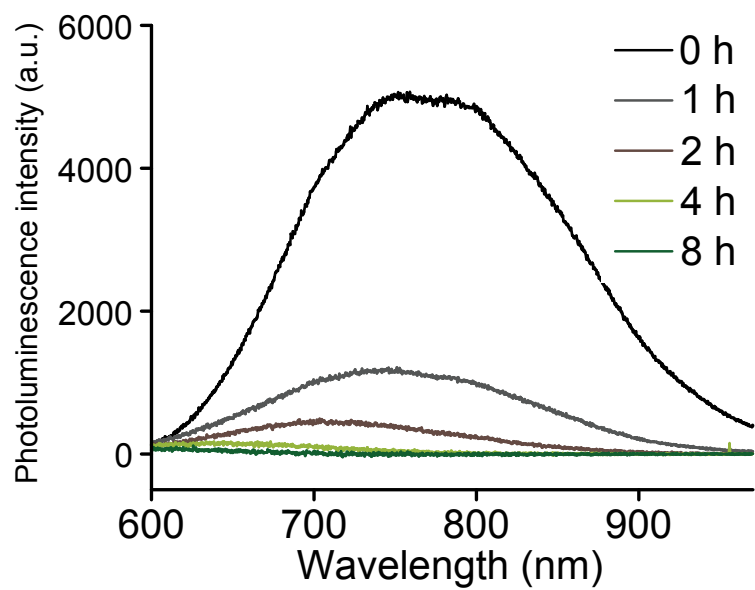


**Figure 2.9 Evolution of photoluminescence spectrum of LPSiNP during degradation under physiological conditions (in PBS at 37 °C).** The maximum intensity of the photoluminescence spectrum at each time point was used for Fig. 2.1d.

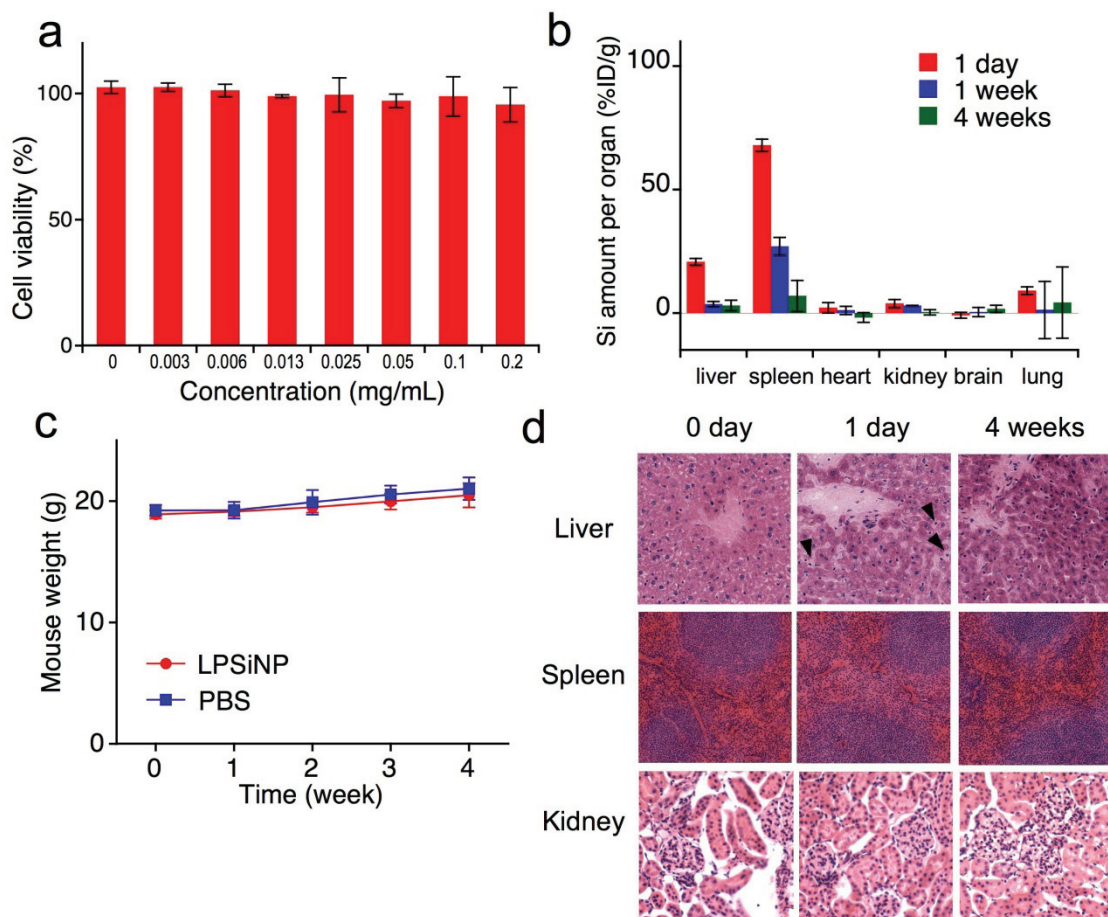


**Figure 2.10 Biocompatibility and biodegradability of luminescent porous Si nanoparticles (LPSiNP).** (a) *In vitro* cytotoxicity of LPSiNP towards HeLa cells, determined by Calcein assay. LPSiNP at the indicated concentrations were incubated with cells for 48 h. (b) *In vivo* biodistribution and biodegradation of LPSiNP over a period of 4 weeks in mouse. Aliquots of LPSiNP were intravenously injected into the mouse ( $n = 3$  or  $4$ , dose =  $20$  mg/kg). The silicon concentration in the organs was determined at different time points after injection using ICP-OES. Error bars indicate s.d. (c) Change in body mass of mice injected with LPSiNP ( $n = 3$ , dose =  $20$  mg/kg) compared with PBS control ( $n = 4$ ). There is no statistically significant difference in the mass change between control (PBS) and LPSiNP over a period of 4 weeks. Error bars indicate s.d. (d) Liver, spleen, and kidney histology. Livers, spleens, and kidneys were harvested from mice before, 1 day, and 4 weeks after intravenous injection of LPSiNP ( $20$  mg/kg). Organs were stained with hematoxylin and eosin. The arrows indicate the LPSiNP taken up by macrophages in the liver. The scale bar is  $50$   $\mu$ m for all images.

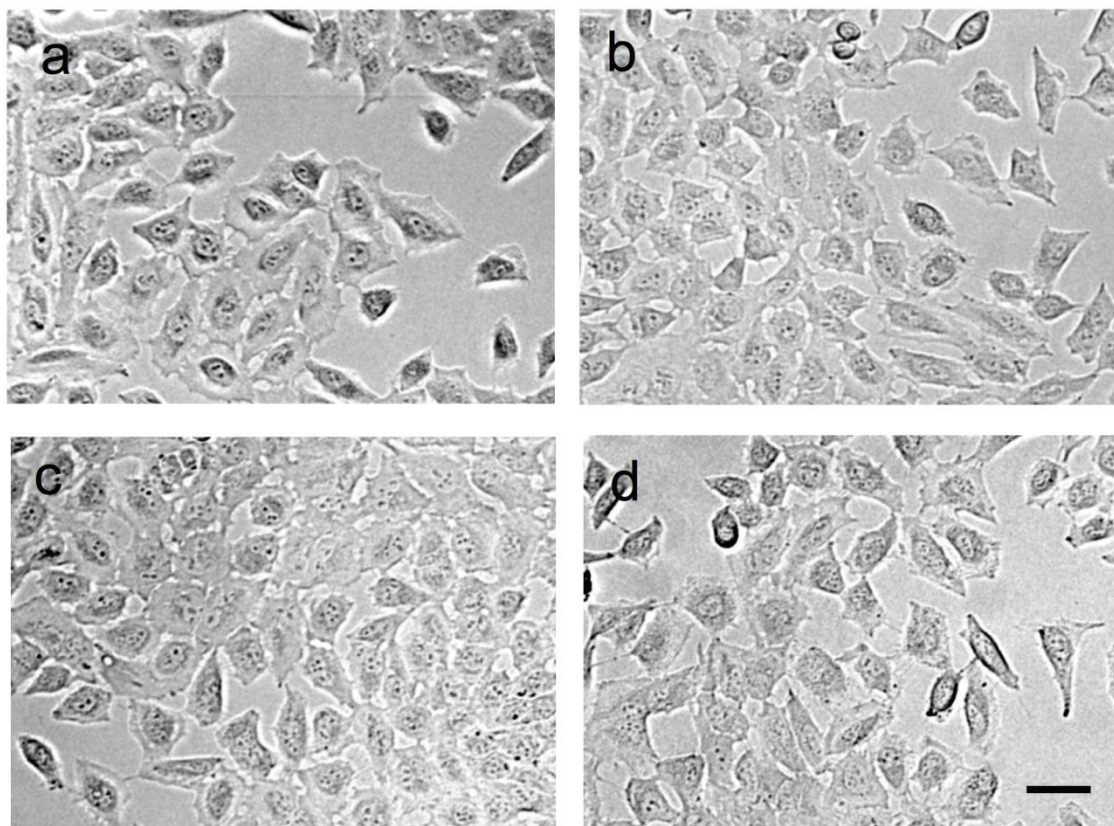


**Figure 2.11 Optical microscope images of HeLa cells incubated with LPSiNP at various concentrations.** (a) 0 mg/mL, (b) 0.013 mg/mL, (c) 0.05 mg/mL, and (d) 0.2 mg/mL of LPSiNP were incubated with HeLa cells. The cells were rinsed three times using cell medium (no phenol red) 48 h after incubation and immediately imaged using an inverted optical microscope. The scale bar is 20  $\mu\text{m}$ .

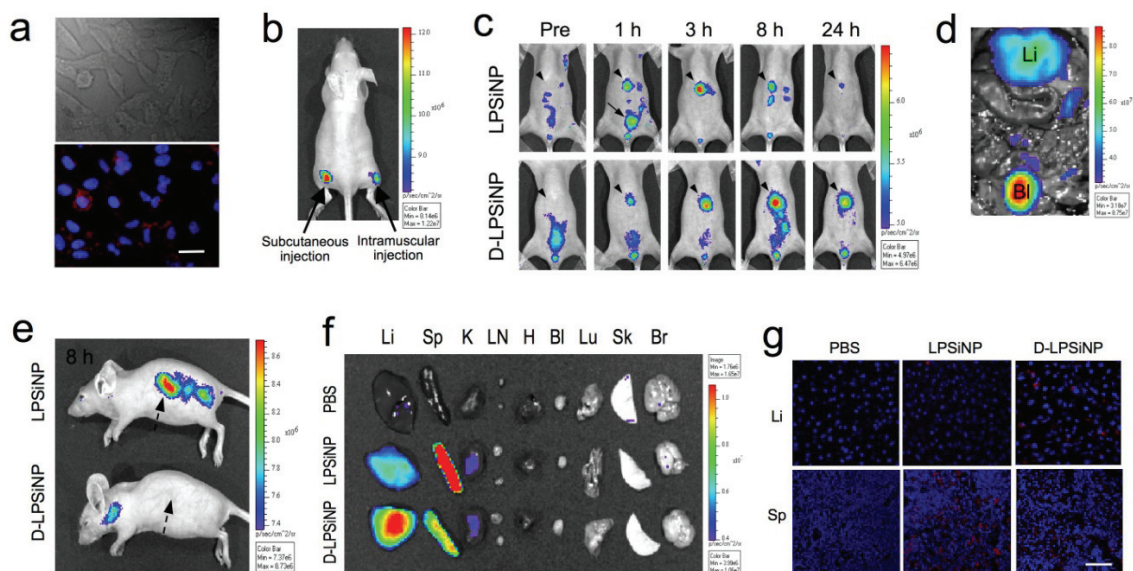


**Figure 2.12** *In vitro*, *in vivo* and *ex vivo* fluorescence imaging with luminescent porous Si nanoparticles (LPSiNP). (a) *In vitro* cellular imaging with LPSiNP. HeLa cells were treated with LPSiNP for 2 h and then imaged. Red and blue indicate LPSiNP and cell nuclei, respectively. The scale bar is 20  $\mu\text{m}$ . (b) *In vivo* fluorescence image of LPSiNP (20  $\mu\text{L}$  of 0.1 mg/mL) injected subcutaneously and intramuscularly on each flank of a mouse. (c) *In vivo* images of LPSiNP and dextran-coated LPSiNP (D-LPSiNP). The mice were imaged at multiple time points after intravenous injection of LPSiNP and D-LPSiNP (20 mg/kg). Arrowhead and arrow with solid line indicate liver and bladder, respectively. (d) *In vivo* image showing the clearance of a portion of the injected dose of LPSiNP into the bladder, 1 h post-injection. Li and Bl indicate liver and bladder, respectively. (e) Lateral image of the same mice shown in (c), 8 h after LPSiNP or D-LPSiNP injection. Arrows with dashed line indicate spleen. (f) Fluorescence images showing the *ex vivo* biodistribution of LPSiNP and D-LPSiNP in mouse. Organs were harvested from the animals shown in (c), 24 h after injection. Li, Sp, K, LN, H, Bl, Lu, Sk, and Br indicate liver, spleen, kidney, lymph nodes, heart, bladder, lung, skin, and brain, respectively. (g) Fluorescence histology images of livers and spleens from the mice shown in (c) and (f), 24 h after injection. Red and blue indicate (D-)LPSiNP and cell nuclei, respectively. The scale bar is 50  $\mu\text{m}$  for all images.

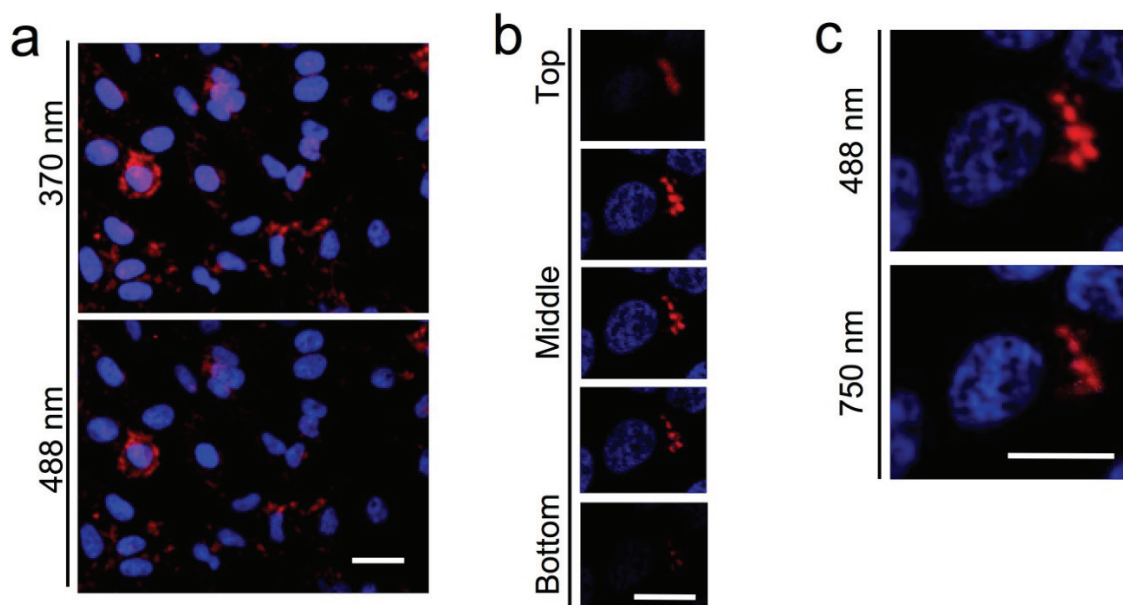


**Figure 2.13 *In vitro* cellular imaging with LPSiNP.** HeLa cells were treated with LPSiNP for 2 h, fixed and then imaged. (a) Fluorescence microscope images of cellular uptake and binding of LPSiNP. The nanoparticles can be imaged *in vitro* under both excitation wavelengths indicated on the left side of the images ( $\lambda_{em} = 650$  nm long pass). (b) Confocal fluorescence microscope images of cellular uptake of LPSiNP ( $\lambda_{ex} = 488$  nm and  $\lambda_{em} = 650$  nm long pass). (c) Multi-photon fluorescence microscope image of cellular uptake of LPSiNP ( $\lambda_{ex} = 750$  nm). The LPSiNP are clearly observable inside the cells under two-photon excitation conditions as well as with single-photon excitation, in agreement with previous observations with porous silicon chips<sup>3</sup>. The scale bar is 20  $\mu$ m.

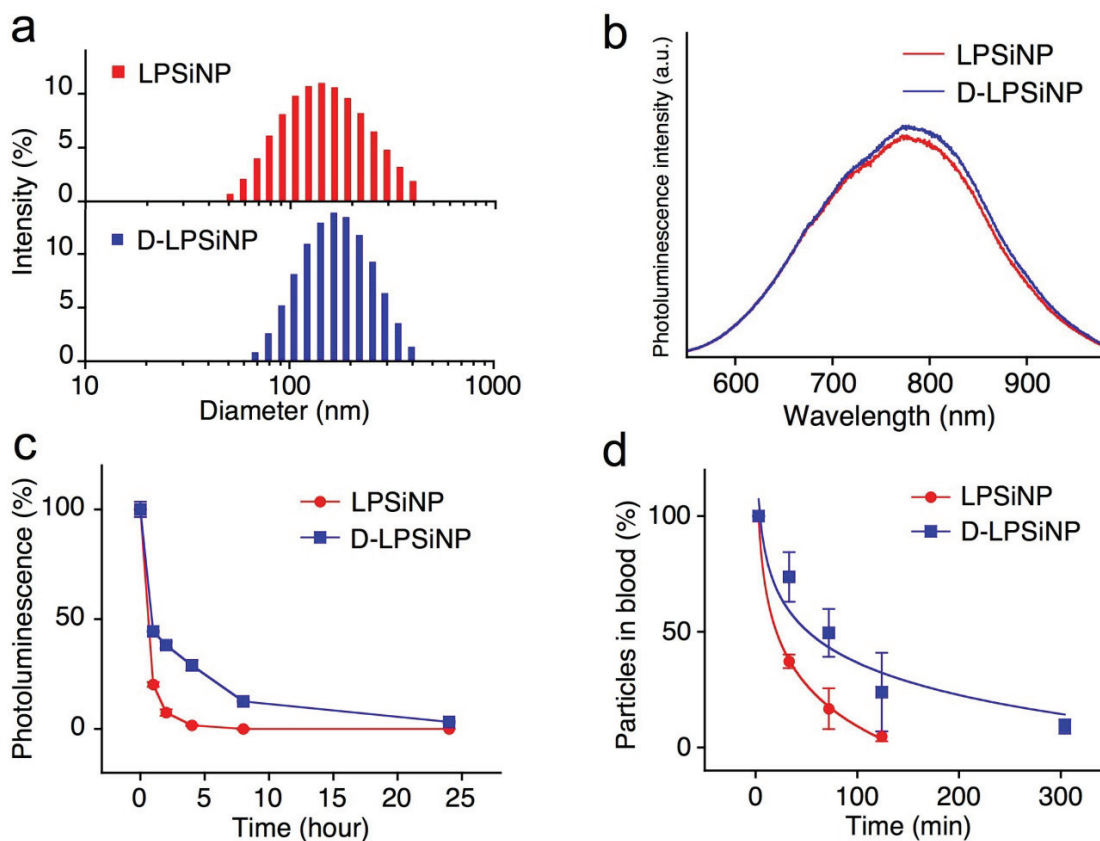


**Figure 2.14 Characterization of dextran-coated luminescent porous silicon nanoparticles (D-LPSiNP).** (a) Dynamic light scattering size data obtained from LPSiNP and D-LPSiNP. Note that the size and zeta potential increases from 125 nm to 151 nm and from -52 mV to -43.5 mV after dextran coating, respectively. Although these samples display a relatively large size distribution, there are several FDA (US Food and Drug Administration)-approved nanoparticle formulations that span this range, such as liposomal doxorubicin (Doxil<sup>®</sup>), albumin-bound Paclitaxel (Abraxane<sup>®</sup>), and dextran-coated iron oxide nanoparticles (Feridex<sup>®</sup>). (b) Photoluminescence spectra of LPSiNP and D-LPSiNP with UV excitation ( $\lambda = 370$  nm). (c) *In vitro* degradation of LPSiNP and D-LPSiNP (in PBS at 37 °C). Degradation is monitored as the intensity of photoluminescence from the nanoparticle. (d) Blood concentration of silicon (by ICP-OES) for mice ( $n = 3$ ) injected with LPSiNP or D-LPSiNP as a function of time. LPSiNP are cleared in a short time (blood half-life:  $27.6 \pm 1.8$  min) while D-LPSiNP circulate for a longer period of time (blood half-life:  $82.0 \pm 15.8$  min).



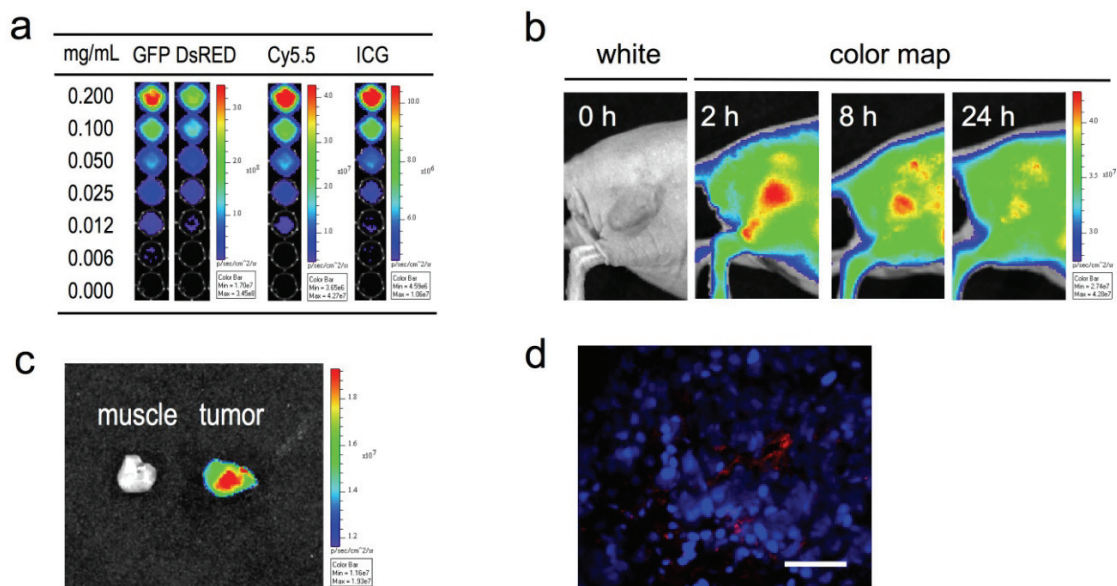


**Figure 2.15 Fluorescence images of tumors containing dextran-coated luminescent porous Si nanoparticles (D-LPSiNP).** (a) Fluorescence images of D-LPSiNP as a function of concentration using different excitation filters (GFP: 445-490 nm and 1 s exposure time, DsRed: 500-550 nm, 2 s exposure time, Cy5.5: 615-665 nm, 8 s exposure time, and ICG: 710-760 nm, 20 s exposure time). The emission filter used is ICG (810-875 nm). (b) Representative fluorescence images of mouse bearing an MDA-MB-435 tumor. The mouse was imaged using a Cy5.5 excitation filter and ICG emission filter at the indicated times after intravenous injection of D-LPSiNP (20 mg/kg). Note that a strong signal from D-LPSiNP is observed in the tumor, indicating significant passive accumulation in the tumor by the EPR effect. (c) *Ex vivo* fluorescence images of tumor and muscle around the tumor from the mouse used in (b). (d) Fluorescence images of a tumor slice from the mouse in (b). Red and blue indicate D-LPSiNP and cell nuclei (DAPI stain), respectively. The scale bar is 100  $\mu$ m.

Chapter two, in part of full, is a reprint (with co-author permission) of the material as it appears in the following publication: Park, Ji-Ho; **Gu, Luo**; von Maltzahn, Geoffrey; Ruoslahti, Erkki; Bhatia, Sangeeta N.; Sailor, Michael J., “Biodegradable Luminescent Porous Silicon Nanoparticles for in vivo Applications”. *Nature Materials* 2009, 8 (4), 331-336. The author of this dissertation is a co-author of this manuscript.

## **CHAPTER III:**

### **In Vivo Time-gated Fluorescence Imaging with Biodegradable Luminescent Porous Silicon Nanoparticles**

### 3.1 Abstract

Fluorescence imaging is one of the most versatile and widely used visualization methods in biomedical research. However, tissue autofluorescence is a major obstacle confounding interpretation of *in vivo* fluorescence images. In this study, I discovered the unusually long emission lifetime (5-13  $\mu$ s) of porous silicon nanoparticles and the methods for turning their lifetime without changing the chemical nature of the nanoparticles. Their long emission lifetime can allow the time-gated imaging of tissues *in vivo*, completely eliminating shorter-lived ( $< 10$  ns) emission signals from organic chromophores or tissue autofluorescence. Using a conventional animal imaging system (eXplore Optix) that is not optimized for such long-lived excited states, we demonstrate improvement of signal to background contrast ratio by  $> 50$ -fold *in vitro* and by  $> 20$ -fold *in vivo* when imaging porous silicon nanoparticles. Time-gated imaging of porous silicon nanoparticles accumulated in a human ovarian cancer xenograft following intravenous injection is demonstrated in a live mouse. This technology potentially permits the multiplexing of images in the time domain by using separate porous silicon nanoparticles engineered with different excited state lifetimes.

### 3.2 Introduction

Fluorescence imaging has become a dominant *in vitro* and *in vivo* visualization method in biomedical research due to its high sensitivity, its high spatial resolution, and its ease of use<sup>1-2</sup>. *In vivo* imaging of exogenous fluorescent probes that target diseased tissues has also shown promising results in clinical settings, such as the early detection of breast cancer, the outlining of tumor margins during surgery, and endoscopic diagnosis of

cancer micrometastasis<sup>1,3-5</sup>. However, the method is limited by tissue attenuation (scattering and absorption of the excitation or the emission light) and by tissue autofluorescence<sup>6-7</sup>. To minimize tissue attenuation effects, researchers have concentrated on near-infrared (NIR) fluorophores that are excited and emit in the spectral window between wavelengths of 650 - 950 nm<sup>8-11</sup>. However, tissue autofluorescence still produces a substantial background signal in this spectral range that severely limits the quality of images, especially when very low concentrations of the fluorescent probe accumulate at the target site<sup>12</sup>.

The endogenous fluorophores responsible for tissue autofluorescence have decay lifetimes of  $\sim 1 - 10$  ns, depending on the type of tissue<sup>7</sup>. It has been proposed that late time-gating (i.e., capturing the signal at a delayed time after excitation) could be used to image molecular or quantum dot imaging probes in the presence of this interference<sup>13-15</sup>. However, there is a lack of biocompatible NIR fluorophores with fluorescence lifetimes significantly greater than 1-10 ns, due to the quantum mechanical selection rules associated with organic molecules or direct gap semiconductors<sup>7, 16</sup>.

Electrochemically etched porous silicon has shown considerable potential for *in vivo* applications due to its biodegradability, its low toxicity, its large specific capacity for drug loading, and its intrinsic photoluminescence<sup>17-24</sup>. We have recently developed porous silicon nanoparticles (LPSiNPs) that have intrinsic NIR photoluminescence ( $\sim 650 - 900$  nm)<sup>25</sup>. They show low systemic toxicity and can degrade *in vivo* into renally cleared components. The porous nanostructure of LPSiNPs also enables the incorporation and delivery of drug payloads<sup>21, 25</sup>. Here, we report biodegradable NIR LPSiNPs with tunable long luminescence lifetimes (5.1-13.4  $\mu$ s). Using a commercial time-domain

imager (eXplore Optix) followed by a late time-gating algorithm, interference from endogenous or exogenous fluorophores are eliminated from the signal of LPSiNPs. An example of tumor imaging with this method show much improved sensitivity.

### 3.3 Experimental

*Preparation of polyethylene glycol-coated luminescent porous silicon nanoparticles (PEG-LPSiNPs):* LPSiNPs were prepared following a previously described method<sup>25-26</sup>: (100)-oriented p-type single-crystal Si wafers (0.8-1.1 m $\Omega$ -cm resistivity, obtained from Siltronic, Inc.) were electrochemically etched by application of a constant current density of 200 mA/cm<sup>2</sup> for 150 s in an electrolyte containing aqueous 48% hydrofluoric acid and ethanol in a 3:1 ratio. The resulting porous Si films were lifted from the Si substrate by application of a current pulse of 4 mA/cm<sup>2</sup> for 250 s in a solution containing 3.3% (by volume) of 48% aqueous HF in ethanol. The porous Si film was fractured by ultrasound and filtered through a 0.22  $\mu$ m membrane. Finally, the nanoparticles were mildly oxidized by soaking in deionized water for 2 weeks to activate photoluminescence. The activated nanoparticles were rinsed with deionized water 3 times by centrifugation. LPSiNP samples were prepared at the following etching current densities: 50 mA/cm<sup>2</sup> for 300 s, 200 mA/cm<sup>2</sup> for 150 s, or 400 mA/cm<sup>2</sup> for 150 s. The activation step involved soaking of the LPSiNPs in deionized water for various periods of time: 2 weeks, 6 weeks, or 10 weeks. To prepare PEG-LPSiNPs, a 0.6 mL aliquot of an ethanolic dispersion (0.5 mg/mL LPSiNPs) was mixed with a 0.5 mL aliquot of 6 mg/mL mPEG-Silane (MW 5k, Laysan Bio, Inc.) in ethanol. The mixture was stirred for 16 h at

room temperature. The nanoparticles were rinsed 3 times with ethanol and then 3 times with water. The samples were collected by centrifugation between each rinsing step.

*Size, photoluminescence, and decay lifetime measurement of LPSiNPs:* Dynamic light scattering (Zetasizer Nano ZS90, Malvern Instruments) was used to determine the hydrodynamic size of the nanoparticles. Transmission electron microscope (TEM) images were obtained with a FEI Tecnai G<sup>2</sup> Sphera. Scanning electron microscope (SEM) images were obtained using a Philips XL30 field emission ESEM operating in secondary electron emission mode. The photoluminescence (PL,  $\lambda_{\text{ex}} = 370$  nm, 460 nm long pass emission filter) spectra of LPSiNPs or PEG-LPSiNPs were obtained using a Princeton Instruments/Acton spectrometer fitted with a liquid nitrogen-cooled silicon charge-coupled device (CCD) detector. The PL decay data of the nanoparticles were acquired using a Horiba Scientific FluoroLog-3 spectrofluorometer using a time correlated single photon counting (TCSPC) method. A 456 nm NanoLED (Horiba Scientific) at 10 kHz repetition rate was used as the excitation source. The photon signal was collected at 650 nm at 22 °C. Although the decay curves were nonexponential, the time at which the PL intensity of the nanoparticles decreased to  $1/e$  of the initial value after excitation was used as the average decay lifetime.

*Cell lines and mice:* Two human ovarian carcinoma cell lines SKOV3 and 2008 were used in this study. 2008 cells were transduced with lentiviral vectors containing the red fluorescent protein mCherry sequence (pLVX-mCherry, Clontech). The cells expressing mCherry (2008-mCherry) were sorted by flow cytometry and maintained in

RPMI-1640 medium with 10% fetal calf serum (Invitrogen). Female nu/nu nude mice (Charles River) were maintained in specific pathogen-free facilities at the University of California, San Diego. Animal protocols were approved by the Institutional Animal Care and Use Committee.

*In vitro and in vivo fluorescence imaging:* A time-domain fluorescence imaging system eXplore Optix (ART Advanced Research Technologies, Inc.) was used to image fluorophore solutions and cell suspensions *in vitro*, and mice *in vivo*. A 470 nm laser with 40 MHz repetition rate was used as the excitation source and a 590 nm longpass filter was used as the emission filter for all imaging experiments.

*Comparing PEG-LPSiNPs and Cy3.5 in the time-domain:* For *in vitro* imaging, an aliquot of PEG-LPSiNPs in aqueous dispersion (50  $\mu$ L, 0.1 mg/mL) was placed in a microtube, and an aliquot of Cy3.5 NHS ester (GE Healthcare) in aqueous solution (50  $\mu$ L, 0.01 mg/mL) was placed in a separate microtube. The microtubes were placed next to each other and imaged at the same time with the Optix imaging system. For *in vivo* imaging, PEG-LPSiNPs (20  $\mu$ L, 0.5 mg/mL) and Cy3.5 (20  $\mu$ L, 0.02 mg/mL) were injected subcutaneously into the right and left shoulder of a nude mouse, respectively. The mouse was imaged with the Optix imaging system immediately after injection.

*Comparing PEG-LPSiNPs and mCherry in the time-domain:* For *in vitro* imaging, aliquots of PEG-LPSiNPs (20  $\mu$ L, 0.2 mg/mL) and 2008-mCherry cell suspension (20  $\mu$ L, ~1 million cells) were placed in separate microtubes and imaged at the same time with



the Optix imaging system. For *in vivo* imaging, a nude mouse bearing a 2008-mCherry tumor (~0.7 cm) on each side of the shoulder was used. An aliquot of PEG-LPSiNPs dispersion (50  $\mu$ L, 0.2 mg/mL) was injected into the tumor on the right shoulder of the mouse, and the mouse was imaged with the Optix imaging system immediately after injection.

*In vivo fluorescence imaging of tumor:* a nude mouse bearing a SKOV3 tumor (~0.5 cm, left flank) was used in this study. A PEG-LPSiNPs saline dispersion was injected intravenously into the mouse at a dose of 10 mg/kg body mass through the tail vein. The mouse was imaged at several different time points for 24 h post-injection. The tumor and muscle in the vicinity of the tumor were harvested and imaged 24 h after injection.

*Data analysis and time gating:* The Optix imaging system data were analyzed using OptiView (ART Advanced Research Technologies, Inc.) to calculate the *in vivo* decay lifetimes of the fluorophores or tissue autofluorescence. Continuous wave (CW) fluorescence images were obtained by reconstructing the fluorescent signal collected within the full 25 ns imaging time-window from the data using MATLAB (MathWorks, Inc.). Time-gated (TG) fluorescence images were generated by extracting the fluorescent signal collected between 20.5 and 21.5 ns of the imaging time-window (18-19 ns after the excitation pulse) from the data with MATLAB.

### **3.4 Results and Discussion**

LPSiNPs were prepared by electrochemical etching of single-crystal Si in HF-containing electrolyte, followed by lifting-off of the porous layer, ultrasonic fracture, filtration of the resulting nanoparticles through a 0.22  $\mu\text{m}$  filter membrane, and finally activation of luminescence by treatment in an aqueous solution following the published procedure<sup>25</sup>. To prepare LPSiNPs with various luminescence lifetimes, we used three different etching current densities: 50  $\text{mA}/\text{cm}^2$ , 200  $\text{mA}/\text{cm}^2$ , and 400  $\text{mA}/\text{cm}^2$ . The resulting nanoparticles have similar mean hydrodynamic sizes (Fig. 3.1a), and all three types of LPSiNPs display NIR photoluminescence ( $\lambda_{\text{max}} \sim 800 \text{ nm}$ , Fig. 3.2). The luminescence of porous Si is attributed to quantum confinement effects and interface defects<sup>27-29</sup>. However, different with conventional II-VI quantum dots, porous Si has much longer luminescence lifetime ( $\mu\text{s}$  -  $\text{ms}$  for porous silicon vs. tens of ns for quantum dots) due to the indirect band gap<sup>30</sup>. Furthermore, because the porous Si matrix is an assembly of “Si dots” and contains a distribution of interface states, its luminescence decay is multiexponential<sup>30</sup>. Here, we use the time at which the photoluminescence intensity decreases to  $1/e$  of the initial value after excitation as the average decay lifetime<sup>30-31</sup>. The decay lifetime of LPSiNPs is on the microsecond timescale and tunable by simply adjusting the etching conditions without changing the overall size of the nanoparticles (Fig. 3.1a and Fig. 3.3). In addition, their decay lifetime can be further fine tuned by adjusting the aqueous activation process post-etching (Table 3.1). We hypothesize that the NIR photoluminescence and long decay lifetime of LPSiNPs would allow complete rejection of tissue autofluorescence and other short-lived fluorescent interference using a late time-gating method.

For the time-gated fluorescence imaging study presented here, the LPSiNPs were prepared using electrochemical etching at a current density of 200 mA/cm<sup>2</sup> with a two-week aqueous activation treatment. The nanoparticles were coated with 5 kDa polyethylene glycol (PEG) by reaction with a PEG-silane (PEG-LPSiNP, Fig. 3.1b). The mean hydrodynamic diameter of the PEG-LPSiNP formulation (measured by dynamic light scattering, DLS) was 168 nm, consistent with transmission electron microscopy (TEM) measurements (Fig. 3.4). The photoluminescence spectrum from the PEG-LPSiNPs ( $\lambda_{\text{ex}} = 370$  nm) appeared at wavelengths between 600 and 900 nm (Fig. 3.1c), and the decay lifetime was 12  $\mu\text{s}$  ( $\lambda_{\text{em}} = 650$  nm, 22 °C). This lifetime is >1000 times larger than that typical of tissue autofluorescence or common fluorescent imaging dyes (Fig. 3.1d and 3.1e).

We first tested whether the long-lived photoluminescence from PEG-LPSiNPs could be separated from the fluorescence of conventional fluorophores in the time domain. To demonstrate the potential for practical applications, we used a commercial *in vivo* imaging system (eXplore Optix, ART Inc.). This instrument uses pulsed laser diodes and time-correlated single photon counting (TCSPC) to quantify fluorescence intensity and lifetime<sup>32</sup>. When imaged using a 470 nm excitation laser and a 590 nm longpass emission filter, the intensity of fluorescence from an aqueous solution 10  $\mu\text{g/mL}$  of the common imaging dye Cy3.5 was comparable to an aqueous suspension 100  $\mu\text{g/mL}$  in PEG-LPSiNPs (Fig. 3.5a). The laser we used operates at a repetition rate of 40 MHz, corresponding to a time window between pulses of 25 ns. The duration of an individual pulse from the laser is < 0.1 ns. Although the Cy3.5 sample and the PEG-LPSiNP sample showed similar fluorescence intensity when integrated over the entire 25 ns

window (Fig. 3.5a), gating of the signal at times between 20.5 and 21.5 ns of the imaging window (18 and 19 ns post-pulse after correcting for synchronization) yielded a strong signal from the PEG-LPSiNP sample (50 times greater than background), while the signal from the Cy3.5 sample was at or below the noise level of the instrument (Fig. 3.5b and 3.5c). This improvement in image contrast is due to the rapid decay of fluorescence from the organic fluorophore (0.6 ns lifetime); the signal from the nanoparticle is essentially constant for the duration of the 25 ns period between pulses (Fig. 3.5b). As a result, only the PEG-LPSiNP sample was visible under late time-gating conditions (Fig. 3.5c).

We next investigated the possibility of eliminating tissue autofluorescence or interference from exogenous fluorophores when imaging PEG-LPSiNPs *in vivo*. A 20  $\mu$ L aliquot of PEG-LPSiNPs (0.5 mg/mL) and a 20  $\mu$ L aliquot of Cy3.5 (0.02 mg/mL) in normal saline were injected subcutaneously into the right and left shoulder of a nude mouse, respectively (Fig. 3.5d). When imaged under pseudo continuous wave (CW), or steady-state conditions (i.e., no time gating), the two injection points had intensities comparable to the brighter autofluorescent tissues (Fig. 3.5e). However, the fluorescence intensity-time decay curves of the relevant regions reveal a distinct persistence of signal only for the PEG-LPSiNPs (Fig. 3.5g). Application of the late time-gating algorithm (1 ns gate, 18 ns post-excitation) revealed a distinct spot in the PEG-LPSiNP injection point, with negligible intensity from the Cy3.5 injection or from background tissue autofluorescence (Fig. 3.5f). Simple analysis of pixel intensities revealed a 20-fold increase in image contrast with the time-gated (TG) image relative to the CW image (Fig. 3.5e and 3.5f). It is possible that excitation crossover (bleed-through of the excitation

source scattered from the tissues), a common problem for *in vivo* fluorescence imaging, may also contribute to the background signals in the CW fluorescence images. Since the pulse width of the excitation laser was  $<0.1$  ns, the time-gating method was also able to remove this potential interference.

Genetically expressed fluorophores such as fluorescent proteins are widely used in biomedical research, so we next tested time-gated imaging of PEG-LPSiNPs in the human ovarian carcinoma 2008 cell line expressing the red fluorescent protein mCherry (2008-mCherry), Fig. 3.6a. The fluorescence lifetime of mCherry is  $\sim 1.4$  ns<sup>33</sup>, Fig. 3.6b. *In vitro* imaging of PEG-LPSiNPs and 2008-mCherry cells showed that the signal from the nanoparticles was readily distinguishable using late time-gated imaging (Fig. 3.6c and 3.6d).

The PEG-LPSiNPs were also readily distinguishable from mCherry *in vivo*. A nude mouse bearing a 2008-mCherry tumor xenograft on each shoulder was imaged. The CW image displayed fluorescence from both tumors as well as strong tissue autofluorescence (Fig. 3.7a and 3.7b). Late time-gated imaging was not able to distinguish the fluorescence of mCherry from tissue autofluorescence due to their similar short fluorescence lifetimes (Fig. 3.7b). PEG-LPSiNPs (50  $\mu$ L, 0.2 mg/mL) were then injected into the tumor on the right shoulder of the mouse, and the mouse was imaged again under CW conditions. The tumor injected with nanoparticles was brighter than the control tumor in the CW image, but tissue autofluorescence and the signal from the control tumor were still clearly visible (Fig. 3.7c). In contrast, signals from both the control tumor and tissue autofluorescence were completely eliminated in the time-gated image (Fig. 3.7c). *Ex vivo* fluorescence images confirmed the presence of PEG-LPSiNPs

in the tumor, and they demonstrated the effectiveness of time-gated imaging of PEG-LPSiNPs in *ex vivo* tissues (Fig. 3.7d to 3.7f).

Finally, we evaluated the potential of imaging tumors using intravenously injected circulating PEG-LPSiNPs as the fluorescent probe. Intravenously injected nanoparticles can passively accumulate in tumor tissues due to the enhanced permeability and retention (EPR) effect<sup>34-36</sup>. However, the efficiency of this process is low and generally only a small fraction of injected nanoparticles accumulates in a tumor<sup>37-38</sup>. This creates a challenge for *in vivo* optical imaging because tissue autofluorescence can overwhelm the signals from the fluorescent probe. To evaluate the ability of late time-gated PEG-LPSiNPs to remove tissue autofluorescence in this situation, PEG-LPSiNPs (10 mg/kg) were injected intravenously into a nude mouse bearing a human ovarian carcinoma SKOV3 xenograft tumor (Fig. 3.8a). Fluorescent images of the mouse were intermittently acquired over a 24 h time period post-injection. No signal from the nanoparticles was observed in either the CW or the TG images immediately after injection (Fig. 3.8b), and only weak fluorescence was detected in the tumor 1 h after injection. However, the signal from the nanoparticles was too low to be differentiated from tissue autofluorescence even with time-gating (Fig. 3.8c). As time progressed more PEG-LPSiNPs accumulated at the tumor, and the TG image obtained 4 h post-injection clearly revealed the site of the tumor (Fig. 3.8d). No contrast between tumor and normal tissue was observed in the CW image due to the pronounced autofluorescence signals. The intensity ratio between the tumor and normal tissues increased from ~1 in the CW image to 3 in the TD image (Fig. 3.8d). The signal from the tumor then decreased substantially 24 h post-injection (Fig. 3.8e) as the nanoparticles degraded and cleared from the host<sup>25</sup>. *Ex vivo* fluorescence images

indicated that a small, but detectable quantity of PEG-LPSiNPs remained in the tumor 24 h post-injection (Fig. 3.9).

### 3.5 Conclusions

Although the commercial time-domain imager used in the present study to identify and track the silicon-based nanoparticles has very good (sub-nanosecond) time resolution and excellent detector sensitivity, it is limited in the delay time that can be applied due to the repetition rate of the pulsed laser. A less sophisticated imaging system, with an ability to gate at a modest ( $>100$  ns or even longer) delay time, is expected to yield even better image quality from PEG-LPSiNPs due to the long (microseconds) emission lifetimes of this probe (Fig. 3.1d). If we assume tissue autofluorescence has a single exponential decay with 10 ns lifetime, then its intensity would drop to the order of  $10^{-44}$  times of its initial value 1 microsecond after excitation; whereas PEG-LPSiNPs would still remain  $> 80\%$  of its initial intensity at the same time (Fig. 3.1d).

In contrast to conventional molecular probes, the decay lifetime of LPSiNPs can be flexibly tuned without changing the chemical nature of the probe, using a mild aqueous treatment (Table 3.1). This provides the possibility of multiplex imaging using multiple nanoparticle probes and various time gates. Furthermore, the slow change in emission lifetime that occurs upon degradation in aqueous media allows the nanoparticle to report on its age in the system. In addition to their unique optical properties, the low toxicity and biodegradable characteristics of LPSiNPs overcomes some of the disadvantages of cytotoxic or non-biodegradable fluorescent probes currently used for *in vitro* or *in vivo* imaging.

### 3.6 References

1. Ntziachristos, V. Fluorescence molecular imaging. *Annual review of biomedical engineering* **8**, 1-33 (2006).
2. Leblond, F., Davis, S.C., Valdes, P.A. & Pogue, B.W. Pre-clinical whole-body fluorescence imaging: Review of instruments, methods and applications. *Journal of Photochemistry and Photobiology B-Biology* **98**, 77-94 (2010).
3. Corlu, A. et al. Three-dimensional in vivo fluorescence diffuse optical tomography of breast cancer in humans. *Optics Express* **15**, 6696-6716 (2007).
4. Nguyen, Q.T. et al. Surgery with molecular fluorescence imaging using activatable cell-penetrating peptides decreases residual cancer and improves survival. *Proceedings of the National Academy of Sciences of the United States of America* **107**, 4317-4322 (2010).
5. Kelly, K., Alencar, H., Funovics, M., Mahmood, U. & Weissleder, R. Detection of invasive colon cancer using a novel, targeted, library-derived fluorescent peptide. *Cancer Research* **64**, 6247-6251 (2004).
6. Richards-Kortum, R. & Sevick-Muraca, E. Quantitative optical spectroscopy for tissue diagnosis. *Annu Rev Phys Chem* **47**, 555-606 (1996).
7. Berezin, M.Y. & Achilefu, S. Fluorescence Lifetime Measurements and Biological Imaging. *Chemical Reviews* **110**, 2641-2684 (2010).
8. Weissleder, R. A clearer vision for in vivo imaging. *Nature Biotechnology* **19**, 316-317 (2001).
9. Bashkatov, A.N., Genina, E.A., Kochubey, V.I. & Tuchin, V.V. Optical properties of human skin, subcutaneous and mucous tissues in the wavelength range from 400 to 2000 nm. *Journal of Physics D-Applied Physics* **38**, 2543-2555 (2005).
10. Hilderbrand, S.A. & Weissleder, R. Near-infrared fluorescence: application to in vivo molecular imaging. *Current Opinion in Chemical Biology* **14**, 71-79 (2010).
11. Kobayashi, H., Ogawa, M., Alford, R., Choyke, P.L. & Urano, Y. New Strategies for Fluorescent Probe Design in Medical Diagnostic Imaging. *Chemical Reviews* **110**, 2620-2640 (2010).
12. Gao, X.H., Cui, Y.Y., Levenson, R.M., Chung, L.W.K. & Nie, S.M. In vivo cancer targeting and imaging with semiconductor quantum dots. *Nature Biotechnology* **22**, 969-976 (2004).



13. Cubeddu, R., Canti, G., Taroni, P. & Valentini, G. TIME-GATED FLUORESCENCE IMAGING FOR THE DIAGNOSIS OF TUMORS IN A MURINE MODEL. *Photochemistry and Photobiology* **57**, 480-485 (1993).
14. Dahan, M. et al. Time-gated biological imaging by use of colloidal quantum dots. *Optics Letters* **26**, 825-827 (2001).
15. Hall, D.J., Sunar, U., Farshchi-Heydari, S. & Han, S.-H. In vivo simultaneous monitoring of two fluorophores with lifetime contrast using a full-field time domain system. *Applied Optics* **48**, D74-D78 (2009).
16. Berezin, M.Y. et al. Long Fluorescence Lifetime Molecular Probes Based on Near Infrared Pyrrolopyrrole Cyanine Fluorophores for In Vivo Imaging. *Biophysical Journal* **97**, L22-L24 (2009).
17. Anderson, S.H.C., Elliott, H., Wallis, D.J., Canham, L.T. & Powell, J.J. Dissolution of different forms of partially porous silicon wafers under simulated physiological conditions. *Physica Status Solidi a-Applied Research* **197**, 331-335 (2003).
18. Low, S.P., Voelcker, N.H., Canham, L.T. & Williams, K.A. The biocompatibility of porous silicon in tissues of the eye. *Biomaterials* **30**, 2873-2880 (2009).
19. Salonen, J., Kaukonen, A.M., Hirvonen, J. & Lehto, V.P. Mesoporous silicon in drug delivery applications. *J. Pharm. Sci.* **97**, 632-653 (2008).
20. Tasciotti, E. et al. Mesoporous silicon particles as a multistage delivery system for imaging and therapeutic applications. *Nature Nanotechnology* **3**, 151-157 (2008).
21. Gu, L., Park, J.-H., Duong, K.H., Ruoslahti, E. & Sailor, M.J. Magnetic Luminescent Porous Silicon Microparticles for Localized Delivery of Molecular Drug Payloads. *Small* **6**, 2546-2552 (2010).
22. Gelloz, B., Kojima, A. & Koshida, N. Highly efficient and stable luminescence of nanocrystalline porous silicon treated by high-pressure water vapor annealing. *Applied Physics Letters* **87** (2005).
23. Anglin, E.J., Cheng, L., Freeman, W.R. & Sailor, M.J. Porous silicon in drug delivery devices and materials. *Advanced Drug Delivery Reviews* **60**, 1266-1277 (2008).
24. Cheng, L. et al. Intravitreal properties of porous silicon photonic crystals: A potential self-reporting intraocular drugdelivery vehicle. *British Journal of Ophthalmology* **92**, 705-711 (2008).
25. Park, J.-H. et al. Biodegradable luminescent porous silicon nanoparticles for in vivo applications. *Nature Materials* **8**, 331-336 (2009).

26. Sailor, M.J. Porous Silicon in Practice: Preparation, Characterization, and Applications. (Wiley-VCH, Weinheim, Germany; 2012).
27. Canham, L.T. SILICON QUANTUM WIRE ARRAY FABRICATION BY ELECTROCHEMICAL AND CHEMICAL DISSOLUTION OF WAFERS. *Applied Physics Letters* **57**, 1046-1048 (1990).
28. Lehmann, V. & Gosele, U. POROUS SILICON FORMATION - A QUANTUM WIRE EFFECT. *Applied Physics Letters* **58**, 856-858 (1991).
29. Wolkin, M.V., Jorne, J., Fauchet, P.M., Allan, G. & Delerue, C. Electronic states and luminescence in porous silicon quantum dots: The role of oxygen. *Physical Review Letters* **82**, 197-200 (1999).
30. Cullis, A.G., Canham, L.T. & Calcott, P.D.J. The structural and luminescence properties of porous silicon. *Journal of Applied Physics* **82**, 909-965 (1997).
31. Xie, Y.H. et al. LUMINESCENCE AND STRUCTURAL STUDY OF POROUS SILICON FILMS. *Journal of Applied Physics* **71**, 2403-2407 (1992).
32. Gallant, P. et al. in Biomedical Topical Meeting, Vol. OSA Technical Digest (Optical Society of America, 2004), paper WD2. 2004).
33. Merzlyak, E.M. et al. Bright monomeric red fluorescent protein with an extended fluorescence lifetime. *Nature Methods* **4**, 555-557 (2007).
34. Iyer, A.K., Khaled, G., Fang, J. & Maeda, H. Exploiting the enhanced permeability and retention effect for tumor targeting. *Drug Discovery Today* **11**, 812-818 (2006).
35. Peer, D. et al. Nanocarriers as an emerging platform for cancer therapy. *Nature Nanotechnology* **2**, 751-760 (2007).
36. Brigger, I., Dubernet, C. & Couvreur, P. Nanoparticles in cancer therapy and diagnosis. *Advanced Drug Delivery Reviews* **54**, 631-651 (2002).
37. Ruoslahti, E., Bhatia, S.N. & Sailor, M.J. Targeting of drugs and nanoparticles to tumors. *Journal of Cell Biology* **188**, 759-768 (2010).
38. Minchinton, A.I. & Tannock, I.F. Drug penetration in solid tumours. *Nature Reviews Cancer* **6**, 583-592 (2006).
39. Buschmann, V., Weston, K.D. & Sauer, M. Spectroscopic study and evaluation of red-absorbing fluorescent dyes. *Bioconjugate Chemistry* **14**, 195-204 (2003).
40. Sa'ar, A. Photoluminescence from silicon nanostructures: The mutual role of quantum confinement and surface chemistry. *Journal of Nanophotonics* **3** (2009).

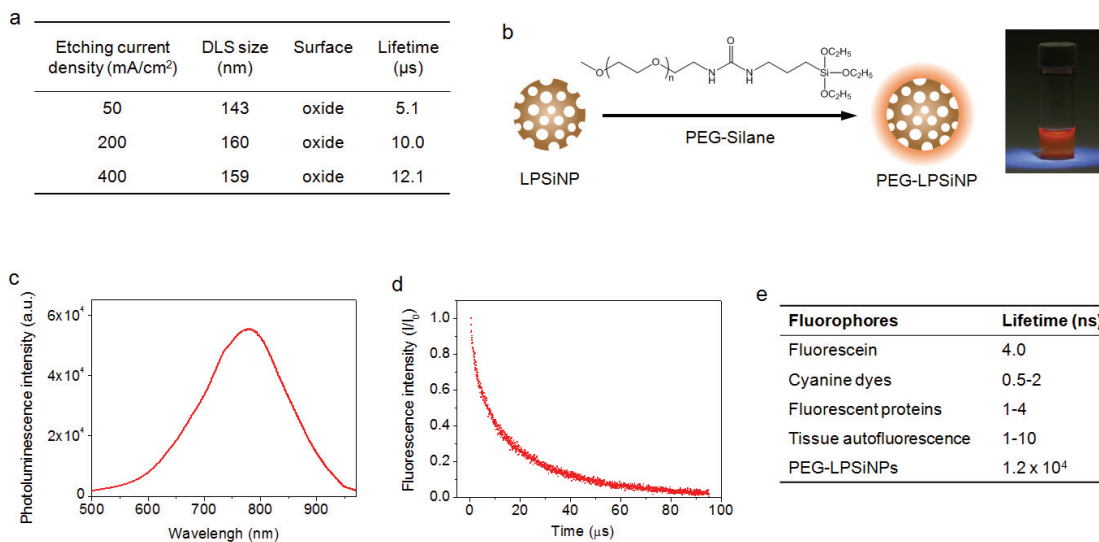


**Figure 3.1 Characterization of polyethylene glycol-conjugated luminescent porous silicon nanoparticles (PEG-LPSiNPs).** (a) Table comparing hydrodynamic diameter, surface chemistry, and emission lifetime of LPSiNPs prepared at the indicated etch current densities. (b) Schematic diagram depicting the PEG surface chemistry on the LPSiNPs. Photograph of PEG-LPSiNPs in water, obtained under UV light illumination. (c) Steady-state photoluminescence spectrum of PEG-LPSiNPs ( $\lambda_{\text{ex}} = 370$  nm). (d) Normalized photoluminescence intensity-time trace for PEG-LPSiNPs after pulsed excitation ( $\lambda_{\text{ex}} = 456$  nm,  $\lambda_{\text{em}} = 650$  nm, 22 °C). (e) Fluorescence lifetimes of commonly used fluorophores and tissue autofluorescence<sup>7, 39</sup>.

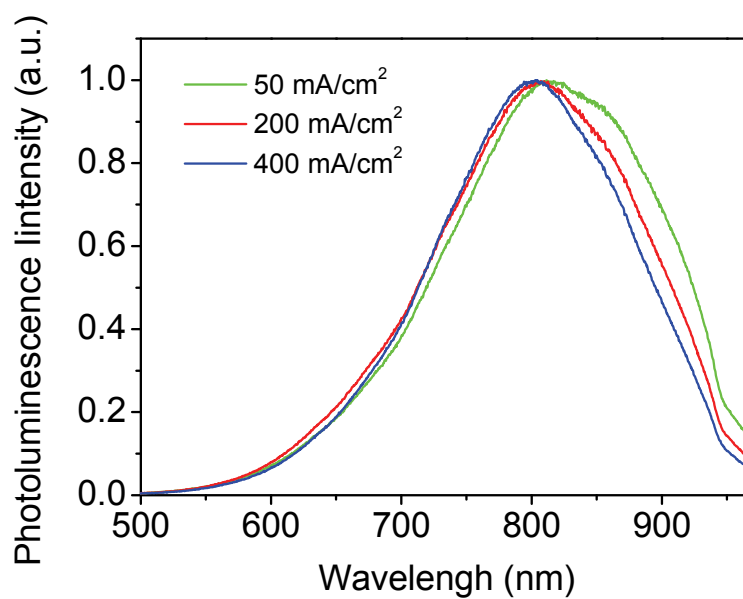


**Figure 3.2** Steady-state photoluminescence (PL) spectra of LPSiNPs in deionized water. Samples were prepared at etching current densities of 50 mA/cm<sup>2</sup>, 200 mA/cm<sup>2</sup>, or 400 mA/cm<sup>2</sup> as indicated. All samples were activated in deionized water for 2 weeks prior to data acquisition. Excitation wavelength was  $\lambda_{\text{ex}} = 370$  nm.

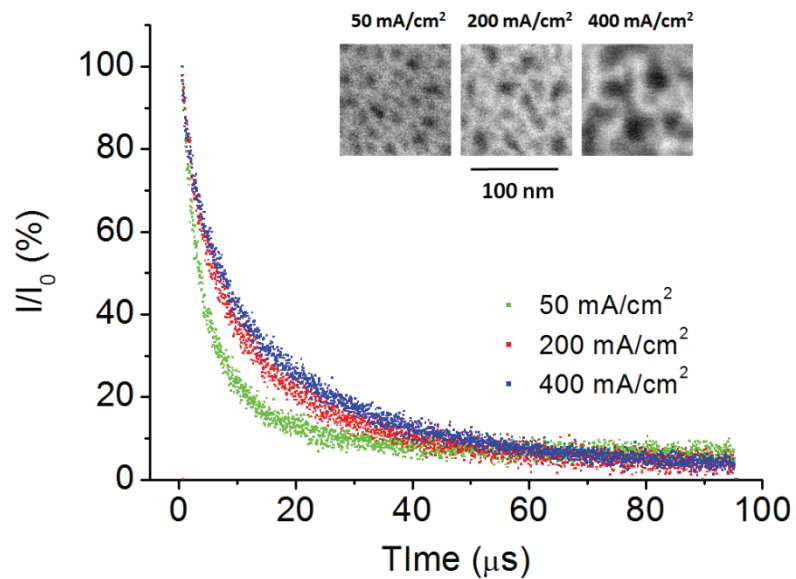


**Figure 3.3** Photoluminescence decay curves for LPSiNPs prepared at etching current densities of 50  $\text{mA}/\text{cm}^2$ , 200  $\text{mA}/\text{cm}^2$ , or 400  $\text{mA}/\text{cm}^2$ , as indicated. Inset shows scanning electron microscope (SEM) images of the porous nanostructures of the porous Si films prior to nanoparticle formation.

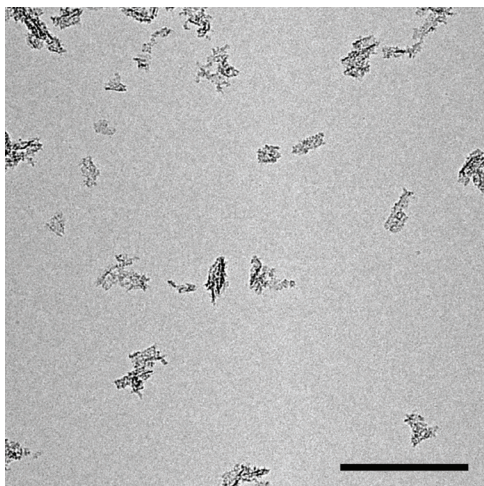


**Figure 3.4** Transmission electron microscope image of polyethylene glycol coated LPSiNPs (PEG-LPSiNPs). Scale bar is 500 nm.

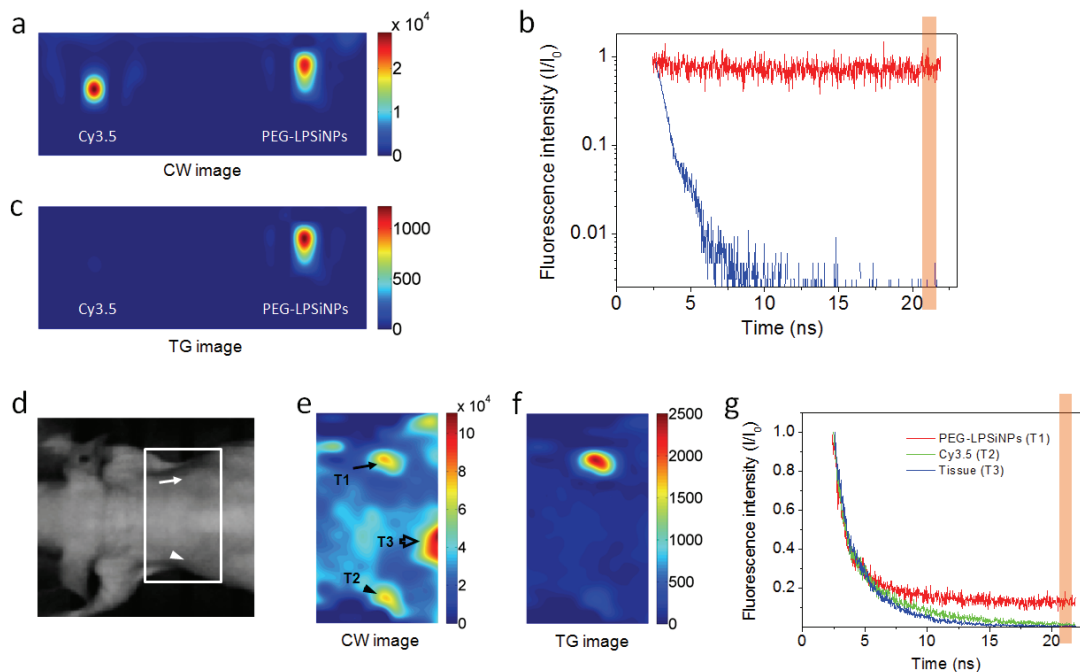


**Figure 3.5** *In vitro* and *in vivo* comparison of time-domain fluorescence characteristics of porous Si nanoparticles (PEG-LPSiNPs) and the common imaging fluorophore Cy3.5. **a**, Steady-state, or continuous wave (CW) fluorescence images of Cy3.5 (0.01 mg/mL) and PEG-LPSiNPs (0.1 mg/mL) samples in microtubes ( $\lambda_{\text{ex}} = 470$  nm,  $\lambda_{\text{em}} = 590$  nm longpass). **b**, Normalized intensity decay of the fluorescence signals from the Cy3.5 and PEG-LPSiNPs samples shown in (a) as a function of time after excitation pulse. The vertical orange bar depicts the time window used in the time-gating algorithm (20.5-21.5 ns of the 25 ns imaging window, which is 18-19 ns after excitation pulse) to obtain time-gated (TG) fluorescence images. **c**, The same image shown in (a), but with the time-gating algorithm applied. The image of the Cy3.5 sample almost completely disappears. **d**, Bright field image of a nude mouse injected subcutaneously with PEG-LPSiNPs (20  $\mu$ L, 0.5 mg/mL) and Cy3.5 (20  $\mu$ L, 0.02 mg/mL). The arrow indicates the injection site of PEG-LPSiNPs, and the arrowhead indicates the injection site of Cy3.5. **e**, CW fluorescence image of the region of the mouse indicated by the white box in (d), obtained with the Optix imaging system. Regions identified as T1, T2, and T3 are the injection site of PEG-LPSiNPs, the injection site of Cy3.5, and the abdomen, respectively. **f**, The same image shown in (e), but with the time-gating algorithm applied. Signals from the Cy3.5 dye (T2) and from tissue autofluorescence (T3) almost disappear. The intensity ratio of PEG-LPSiNPs to tissue autofluorescence was calculated by comparing the CW to the TG signal intensities of PEG-LPSiNPs (T1, arrow) and tissue autofluorescence (T3, hollow arrow) as indicated in (e). **g**, Normalized intensity decay of the fluorescence signals from T1, T2, and T3 in (e), as indicated. The vertical orange bar depicts the time window used in the time-gating algorithm for (f).

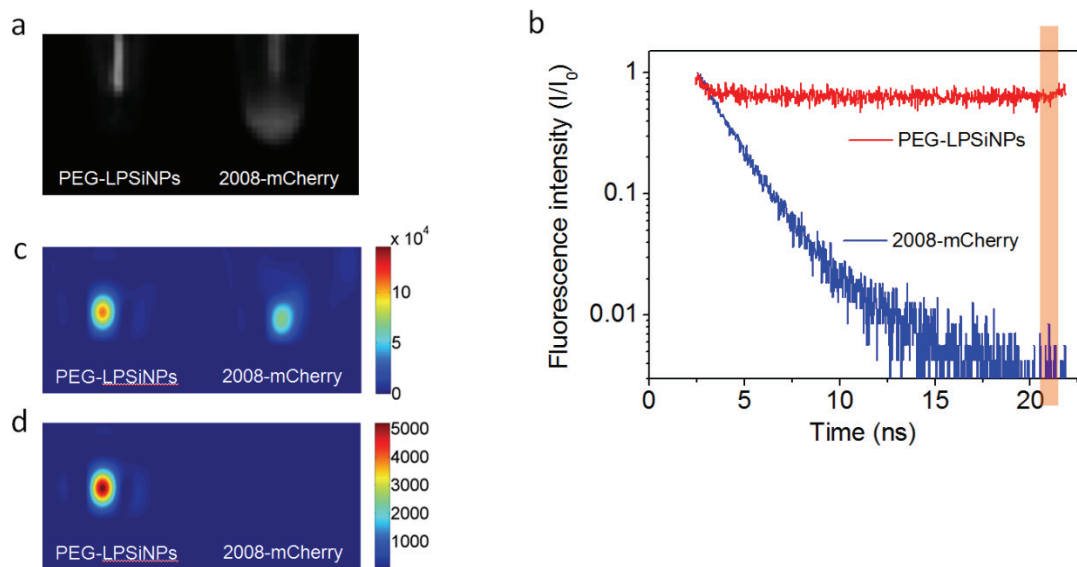


**Figure 3.6 Comparison of PEG-LPSiNPs and mCherry in the time-domain.** **a**, Bright field image of microtubes containing an aqueous dispersion of PEG-LPSiNPs (left, 20  $\mu$ L, 0.2 mg/mL) or 2008-mCherry cell suspension (right, 20  $\mu$ L,  $\sim$ 1 million cells). **b**, Fluorescence decay of above samples measured with Optix imaging system. **c**, Continuous wave (CW) fluorescence image of the PEG-LPSiNPs and 2008-mCherry samples in (a). **d**, Time-gated (TG) fluorescence image of the PEG-LPSiNPs and 2008-mCherry samples in (a).



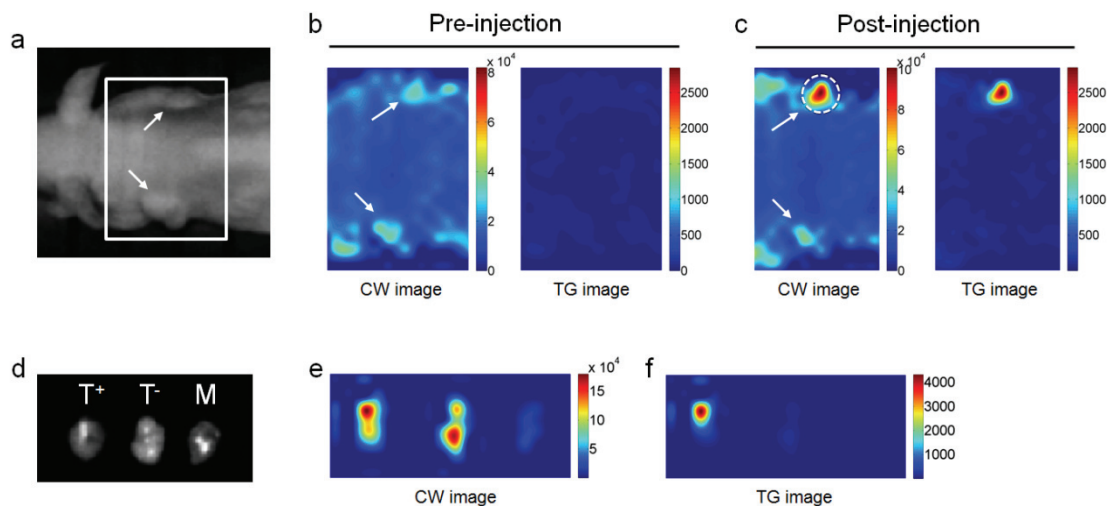


**Figure 3.7 Time-gated fluorescence images comparing PEG-LPSiNP with fluorescent protein mCherry in a nude mouse bearing mCherry-expressing tumors.** **a**, Bright field photograph of mouse containing two tumors, one on each shoulder. Tumors are indicated with white arrows. **b**, CW and TG fluorescence images of the tumors, showing low differentiation of the expressed mCherry and tissue autofluorescence in the time-domain. **c**, CW and TG fluorescence images of the tumors after injection of PEG-LPSiNPs (50  $\mu$ L, 0.2 mg/mL) into the right shoulder tumor (on the top of the image, indicated with dashed white circle). **d**, Ex vivo bright field image of the PEG-LPSiNP-injected tumor (T<sup>+</sup>), a control tumor (T<sup>-</sup>) and muscle tissue excised from the animal post-injection. **e**, CW fluorescence image of the excised tissues in (**d**). **f**, TG fluorescence image of the tissues in (**d**).

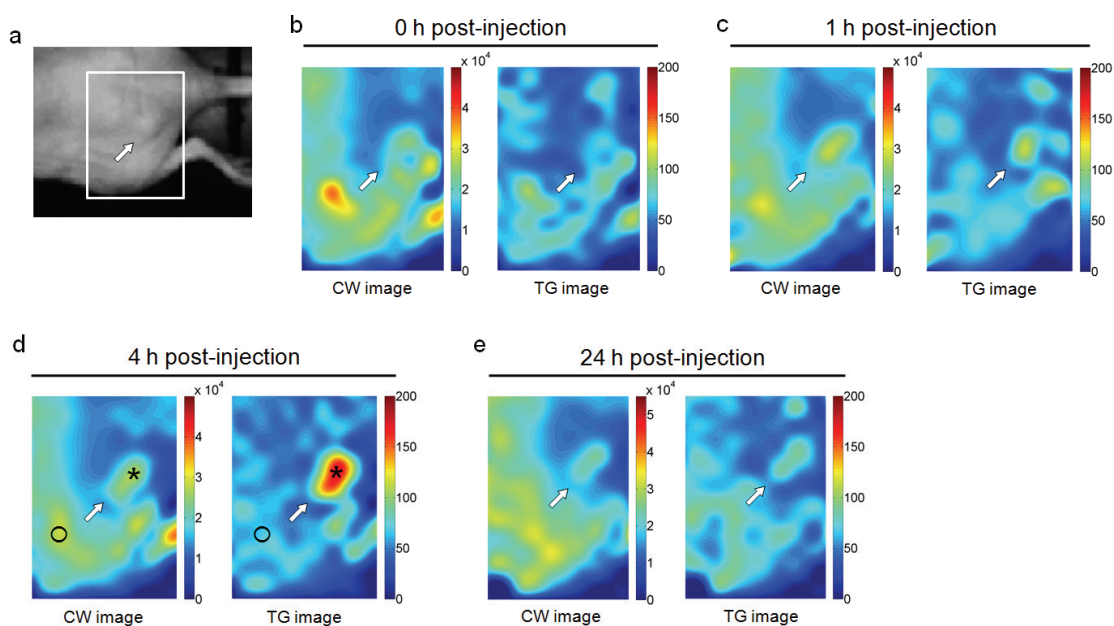


**Figure 3.8 Time-gated fluorescence images of mouse bearing SKOV3 xenograft tumor after IV (tail vein) injection of PEG-LPSiNPs, as indicated. a,** Bright field image of a nude mouse bearing a tumor at the flank. The arrow indicates the site of the tumor. **b-e,** CW and TG fluorescence images of the region indicated with the white box in (a) immediately (b), 1h (c), 4 h (d), or 24 h (e) post-injection of PEG-LPSiNPs (10 mg/kg body weight). The signal to background (tissue autofluorescence) ratio described in the text was calculated by comparing signal intensities at the sites indicated by the black asterisk (PEG-LPSiNPs) and the black circle (tissue autofluorescence) as indicated in (d) in both CW and TG images.

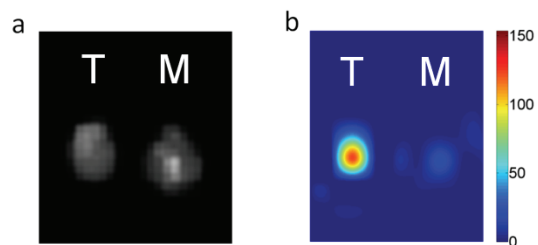


**Figure 3.9** *Ex vivo* fluorescence images of SKOV3 xenograft tumor and muscle in the vicinity of the tumor. The tissues were harvested from the mouse intravenously injected with PEG-LPSiNPs 24 h post-injection. **a**, Bright field image of the SKOV3 tumor (T) and muscle (M) in the vicinity of the tumor. **b**, Time-gated fluorescence image of the tissues in (a).

**Table 3.1 Photoluminescence decay lifetimes of LPSiNPs prepared at different etching current densities and activation durations.**

Etching current density (mA/cm <sup>2</sup> )	DLS size (nm)	Surface	Lifetime ( $\mu$ s)		
			2 weeks activation	6 weeks activation	10 weeks activation
50	143	oxide	5.1	6.6	6.9
200	160	oxide	10.0	10.7	11.1
400	159	oxide	12.1	13.2	13.4

The luminescence of porous Si is attributed to a combination of quantum confinement effects and interface defects<sup>40</sup>. Because the porous Si matrix is an assembly of “Si dots” and contains a distribution of interface states, its luminescence decay is multiexponential. Here, we use the time at which the photoluminescence intensity decreases to  $1/e$  of the initial value after excitation as the average decay lifetime<sup>30-31</sup>.

Chapter three, in part of full, is a reprint (with co-author permission) of the material as it appears in the following publication: **Gu, Luo**; Hall, David J.; Qin, Zhengtao; Howell, Stephen B.; Sailor, Michael J., “In Vivo Time-gated Fluorescence Imaging with Biodegradable Luminescent Porous Silicon Nanoparticles”, *submitted*. The author of this dissertation is the primary author of this manuscript.

## **CHAPTER IV:**

# **Magnetic Luminescent Porous Silicon Microparticles for Localized Delivery of Molecular Drug Payloads**

#### 4.1 Abstract

Magnetic manipulation, fluorescent tracking, and localized delivery of a drug payload to cancer cells in vitro is demonstrated, using nanostructured porous silicon microparticles as a carrier. The multifunctional microparticles are prepared by electrochemical porosification of a silicon wafer in a hydrofluoric acid-containing electrolyte, followed by removal and fracture of the porous layer into particles using ultrasound. The intrinsically luminescent particles are loaded with superparamagnetic iron oxide nanoparticles and the anti-cancer drug doxorubicin. The drug-containing particles are delivered to human cervical cancer (HeLa) cells in vitro, under the guidance of a magnetic field. The high concentration of particles in the proximity of the magnetic field results in a high concentration of drug being released in that region of the Petri dish, and localized cell death is confirmed by cellular viability assay (Calcein AM).

#### 4.2 Introduction

Multifunctional microparticles that are simultaneously magnetic and fluorescent have attracted interest because they can be manipulated with an external magnetic field while being tracked by fluorescence imaging in real time.<sup>1-7</sup> Several examples of potential uses have been demonstrated: immunoassays for bacterial spores or explosives,<sup>8-9</sup> cell-based or DNA assays,<sup>10-13</sup> gene expression profiling,<sup>14</sup> chemical sensing,<sup>15</sup> and safety controls of medical devices.<sup>16</sup> Preparation of such multifunctional microparticles generally involves incorporating the fluorescent (organic fluorophore, quantum dot) and magnetic (iron oxide nanoparticle) components into a non-functional matrix like silica spheres or polystyrene beads.<sup>1-2,7,13,17-19</sup> Issues associated with this

approach include quenching or leakage of the luminescent species,<sup>6,12,17-18</sup> as well as photobleaching (in the case of organic fluorophores).<sup>20-21</sup> Although quantum dots typically display greater stability than organic dyes, toxicity of heavy-metal-containing quantum dots<sup>22</sup> limits their use in many biological applications.

Intrinsically luminescent silicon nanostructures offer an alternative fluorophore that can be as photostable as the conventional II-VI quantum dots,<sup>23-25</sup> but with lower *in-vivo* or *in-vitro* toxicity.<sup>24-29</sup> Silicon is an essential trace element that is widely distributed in various mammalian (including human) tissues<sup>30-31</sup> in the form of orthosilicate ( $\text{SiO}_4^{4-}$ ). Orthosilicate is the primary product of porous Si degradation *in vitro* and *in vivo*, and the low toxicity and biocompatibility of porous Si has been demonstrated.<sup>32-33</sup> Moreover, porous Si nanostructures can act as a host matrix for molecules, enzymes, proteins, magnetic nanoparticles, or other species.<sup>34-37</sup> In this work, magnetic luminescent Si microparticles with porous nanostructures are prepared by incorporating superparamagnetic iron oxide nanoparticles into the intrinsically luminescent porous Si matrix to provide a composite that is simultaneously fluorescent and magnetic. The anticancer drug doxorubicin is loaded into the dual-functional microparticles, and the drug is delivered to human cervical cancer (HeLa) cells *in vitro* under the guidance of a magnetic field, demonstrating magnetic manipulation, fluorescent tracking, and localized delivery of a molecular payload.

### 4.3 Experimental

*Preparation of Luminescent Porous Si Microparticles:* Porous silicon samples were prepared by an anodic electrochemical etch of boron doped p-type Si wafers



(0.0008-0.0012  $\Omega$ -cm resistivity, <100> orientation, Siltronix, inc.) in 3:1 (v:v) 48 % aqueous HF:ethanol. A Teflon etch cell that exposed 8.8 cm<sup>2</sup> of the polished Si wafer surface was used. Samples were etched at a constant current density of 200 mA cm<sup>-2</sup> for 150 s. The porous Si film was then removed from the crystalline Si substrate by application of a current pulse of 4 mA cm<sup>-2</sup> for 250 s in a solution of 3.3 % aqueous HF in ethanol. The free-standing porous Si film was immersed in a sodium borate buffer solution (6.2 mg mL<sup>-1</sup>, pH = 9.2) for 5 min to activate the visible to near-IR emission, and it was then washed with deionized water several times. The luminescent porous Si film was placed in deionized water and fractured into microparticles by ultrasonication for 5 h (FS5, Fisher Scientific). The small fragments were removed by filtration through a 5  $\mu$ m filter membrane (Millipore).

*Preparation of Magnetic, Luminescent Porous Si Microparticles:*

Superparamagnetic iron oxide (Fe<sub>3</sub>O<sub>4</sub>) nanoparticles were synthesized following a published method.<sup>40</sup> The iron oxide nanoparticle suspension was diluted with 3 parts acetone to 1 part nanoparticle suspension in order to make the final concentration of iron oxide  $\sim$ 0.6 mg mL<sup>-1</sup>. The luminescent porous Si microparticles were then added to the iron oxide nanoparticle suspension and stirred for 5 min in air at room temperature. The particulate product was isolated from solution by centrifugation and rinsed several times with acetone and water to remove the free iron oxide nanoparticles. The porous Si/iron oxide composite was then thermally oxidized and dehydrated in air at 100 °C overnight to further trap the iron oxide nanoparticles in the porous Si matrix.

*Characterization:* Scanning electron microscope (SEM) images were obtained using a Philips XL30 field emission ESEM operating in secondary electron emission mode. N<sub>2</sub> adsorption isotherms (interpreted with the BET and BJH models)<sup>50</sup> were measured on a Micromeritics ASAP2020 analyzer. The photoluminescence spectra were obtained using a Princeton Instruments/Acton spectrometer fitted with a liquid nitrogen-cooled silicon charge-coupled device detector ( $\lambda_{\text{ex}} = 370$  nm and 460 nm longpass emission filter). The size of the iron oxide nanoparticles was characterized by transmission electron microscopy (2000EX, JEOL) and by dynamic light scattering (DLS) (Zetasizer Nano ZS90, Malvern Instruments). Magnetization data were collected using a Quantum Design MPMS2 SQUID magnetometer operating at 298 K. To quantify the amount of iron oxide contained in the composite particles, they were dissolved in hydrofluoric acid and the iron concentration of the solution was measured by atomic emission using an inductively coupled plasma instrument fitted with an optical emission spectrometer (ICP-OES, Optima 3000DV, Perkin Elmer). The Fourier-transform infrared (FTIR) spectra of as-etched porous silicon films and luminescent porous Si microparticles were obtained in absorption mode using a Thermo Scientific Nicolet 6700 FTIR spectrometer equipped with a diamond attenuated total reflectance (ATR) accessory. N<sub>2</sub> adsorption isotherms (interpreted with the BET and BJH models) were measured on a Micromeritics ASAP2020 analyzer. The photostability of magnetic, luminescent porous Si microparticles was evaluated relative to the organic fluorophore fluorescein absorbed on silica microbeads. Both samples were dispersed on glass slides and were illuminated with a 100 W mercury lamp, and fluorescence intensities were monitored periodically (1 m intervals) during the experiment using a fluorescence

microscope (Eclipse LV150, Nikon) equipped with a thermoelectrically cooled CCD camera (CoolSNAP HQ2, Photometrics). Excitation ( $355 \pm 25$  nm for magnetic, luminescent porous Si microparticles,  $480 \pm 20$  nm for fluorescein) and emission (435 nm long pass for magnetic, luminescent porous Si microparticles,  $535 \pm 25$  nm for fluorescein) filters were used for these experiments.

*Drug loading and release:* Doxorubicin (DOX) was loaded into the magnetite-containing porous Si microparticles by mixing 1 mg of particles with 0.5 mL of an aqueous solution that was  $1 \text{ mg mL}^{-1}$  in DOX for 1 h in air at room temperature. The particles were harvested from the solution using a permanent rare earth magnet and rinsed 5 times with water to remove free DOX. The amount of DOX incorporated into the microparticles was determined by extracting the drug into a 1:1 water:ethanol solution 0.5 M in HCl and comparing the optical absorbance with a standard curve ( $\lambda = 480$  nm, SpectraMax Plus 384, Molecular Devices). HPLC-MS was used to compare the structure of DOX extracted from porous Si microparticles (by ethanol) and DOX standard. A Thermo LCQdeca mass spectrometer coupled with an HP1100 LC system was employed for LC-UV-MS analysis. Electrospray ionization (ESI) was used and operated under positive ion mode. The UV detection wavelength was set to monitor 480 nm. A Shiseido C-18 column (MGIII, 2.0mm ID x 50 mm) was used for separation with a flow rate of  $0.20 \text{ ml min}^{-1}$ . LC mobile phase A consisted of 5% methanol in water with 0.1% formic acid, and LC mobile phase B consisted of pure methanol with 0.1% formic acid. The LC gradient started from 20% B and was increased to 95% B in 18 min, then reduced to 20% B in 2 min, and then held at 20% B for 3 min. An Xcalibur 1.2 system was used for data

acquisition and processing. The release of adsorbed DOX into aqueous buffer solution was studied by incubating 0.2 mg of DOX-loaded magnetic, luminescent porous Si microparticles in 1 mL of phosphate buffered saline (PBS) at 37 °C, with the solution replaced daily. At each time point, the particles were isolated from the aqueous phase by centrifugation, and the optical absorbance of the supernatant was measured to determine the amount of released DOX. Because DOX is moderately unstable under physiological conditions,<sup>45, 51-52</sup> the stability and degradation profile of free DOX in PBS under the above release conditions was determined by monitoring its optical absorbance. The drug release data were corrected using the degradation profile at each time point. Fluorescence microscopy images of the DOX-loaded microparticles were acquired using a fluorescence microscope (Eclipse LV150, Nikon) fitted with a thermoelectrically cooled CCD camera (CoolSNAP HQ<sup>2</sup>, Photometrics), using an excitation wavelength of 360 nm and an emission filter with a bandpass at  $720 \pm 80$  nm.

*In vitro cytotoxicity of DOX and DOX with magnetite:* HeLa cells were incubated with different concentrations of free DOX or a mixture of DOX and iron oxide nanoparticles for 48 h. Cytotoxicity was evaluated using MTS assay (Promega). The mass ratio of DOX to iron oxide was fixed at 98:8, which is the same as in the loaded porous Si microparticles.

*Localized delivery of DOX to HeLa cells:* HeLa cells were seeded into 60-mm Petri dishes with 4 mL of cell media and cultured for 2 days (the cell confluency was ~ 90%). The DOX-loaded magnetic luminescent porous Si microparticles (0.1 mg to 0.4

mg, depending on the experiment) were then added and attracted to an edge of the Petri dish with a rare-earth permanent magnet. The Petri dish was agitated for 1 min with the magnet attached and then incubated at 37 °C for 8 or 24 hours without any agitation. A comparison of non-guided DOX delivery was conducted by incubating 0.1 mg of DOX-loaded magnetic luminescent porous Si microparticles with HeLa cells using the procedure described above but without the use of a magnet. Cell viability was examined by observing morphology of the cells using a phase contrast microscope (TE 300, Nikon) and by a fluorescent viability stain assay (Calcein AM, Invitrogen, inc.).

#### 4.4 Results and Discussion

Magnetic, luminescent porous Si microparticles were prepared as outlined in Fig. 4.1a. Electrochemical etching of highly doped p-type single-crystal Si wafers in an aqueous HF solution containing ethanol produces a porous layer, which is removed from the Si substrate with a secondary current pulse. In order to activate photoluminescence, the porous Si layer is mildly oxidized in an aqueous borate buffer solution (pH = 9.2). The film is then fractured by ultrasonication and filtered to remove fragments < 5 μm in size. Scanning electron microscopy (SEM) reveals uniform microparticles, with an average size of  $19 \pm 4 \mu\text{m}$  (n = 50, S.D.) and an average pore diameter of  $21 \pm 4 \text{ nm}$  (Fig. 4.1b). Fourier-transform infrared (FTIR) spectroscopy indicates that the oxidation step removes surface Si-H species from the material, generating a silicon oxide shell (Fig. 4.2).

The microparticles display a strong orange to near-IR photoluminescence (Fig. 4.3a), which is attributed to quantum confinement effects in the silicon cores and to Si-SiO<sub>2</sub> interfacial defects generated during the activation step.<sup>27,38-39</sup> Nitrogen

adsorption/desorption measurements reveal a type IV isotherm with a pronounced hysteresis loop, indicating the nanostructure of the microparticles is mesoporous (pore diameters 2-50 nm). The specific surface area (BET method) and pore volume (BJH method) are  $520 \text{ m}^2 \text{ g}^{-1}$  and  $0.712 \text{ cm}^3 \text{ g}^{-1}$ , respectively (Fig. 4.4a).

Magnetic properties were imparted to the luminescent porous Si microparticles by infusion of iron oxide nanoparticles. Superparamagnetic  $\text{Fe}_3\text{O}_4$  nanoparticles with mean diameters of  $13 \pm 2 \text{ nm}$  (measured by transmission electron microscopy) were synthesized following a published method.<sup>40</sup> The nanoparticles were infused into the luminescent porous Si microparticles by placing the microparticles in an aqueous solution of iron oxide nanoparticles as described previously.<sup>34, 41</sup> Once loaded, the microparticles were harvested from the suspension by centrifugation, and the iron oxide nanoparticles were trapped in the porous Si matrix by thermal oxidation/dehydration of the isolated particles in air at  $100 \text{ }^\circ\text{C}$  for 8 h.

The luminescent microparticles retain their overall size upon infusion of iron oxide nanoparticles. However, the average pore diameter ( $12 \pm 3 \text{ nm}$ ), surface area ( $373 \text{ m}^2 \text{ g}^{-1}$ ) and pore volume ( $0.577 \text{ cm}^3 \text{ g}^{-1}$ ) are reduced compared to the iron-free microparticles (Fig. 4.1c and Fig. 4.4b). The intrinsic photoluminescence of the iron oxide-containing microparticles is similar to the iron-free microparticles, although a slight blue shift in the emission spectrum is consistently observed. This blue shift is attributed to a decrease in size of the emissive Si nanoparticles within the porous Si matrix, caused by the oxidation process (Fig. 4.3a).<sup>42</sup> The magnetic composite materials exhibit similar photostability to other inorganic solid state nanoparticles. Like quantum dots deriving from II-VI compounds, the porous Si microparticles are significantly more

photostable compared with fluorescent organic dye molecules, and they are resistant to photobleaching when exposed to UV light (Fig. 4.5). The quantity of iron oxide nanoparticles loaded in the porous Si microparticle carriers is 0.8 % by weight (based on mass of  $\text{Fe}_3\text{O}_4$ , measured by inductively coupled plasma-optical emission spectrometry, ICP-OES). Superconducting quantum interference device (SQUID) data indicates that the magnetic nanoparticles retain their superparamagnetic characteristic when incorporated in the luminescent porous Si host, with a saturation magnetization value of  $0.37 \text{ emu g}^{-1}$  (based on mass of the composite microparticles, Fig. 4.3b). Because the microparticles contain both magnetic and fluorescent functions, they can be manipulated with an external magnetic field and tracked by fluorescence imaging (Fig. 4.3c-f).

As indicated by the BET data, the microparticles still possess free open volume after loading of the iron oxide nanoparticles. This potentially allows the incorporation of an additional payload. In this work, the anticancer drug doxorubicin (DOX) was loaded as a test molecule payload, using a simple adsorption protocol. The iron oxide containing porous Si microparticles were exposed to an aqueous solution of DOX for 1 h, and the particles were harvested from the solution with the aid of a rare earth permanent magnet. The DOX molecules are sufficiently strongly adsorbed that they are not readily removed by rinsing with pure water. However, the DOX molecules are slowly leached into a phosphate buffered saline solution over a period of several days (Fig. 4.6c). Approximately 0.109 mg of DOX was loaded per milligram of magnetic luminescent porous Si microparticles (9.8% by mass). Based on the measured (BET) surface area, the theoretical percent loading of a monolayer of DOX, is 4.4%, which is significantly smaller than the experimental result. The larger loading of DOX measured

experimentally represents multilayer adsorption, attributed to electrostatic interactions between the positively charged DOX molecules and the negatively charged silicon oxide pore walls, and self-association via  $\pi$  -  $\pi$  stacking interactions between DOX molecules.<sup>43-44</sup>

It has been reported that freshly etched porous Si (H-terminated) is a strong reducing agent that can react with molecular drugs such as DOX.<sup>45</sup> Therefore, UV-Vis spectroscopy and high-performance liquid chromatography-mass spectrometry (HPLC-MS) were performed to determine if the chemical composition and the structure of the DOX molecules loaded into the magnetic luminescent porous Si microparticles remain intact. The UV-Vis absorption spectrum of DOX extracted from the porous Si microparticles is identical with the DOX standard (Fig. 4.7). In addition, DOX extracted from the porous Si microparticles displays a single peak in the HPLC trace, with a retention time identical to that of the DOX standard (Fig. 4.6a). Finally, mass spectrometry yields a spectrum identical to the DOX standard (Fig. 4.6b), indicating that there is no significant chemical reaction between DOX and the porous Si matrix in the timescale and conditions of the present study. This lack of reactivity is attributed to the fact that the microparticles used in the present study are more extensively oxidized, presenting an inert SiO<sub>2</sub> surface to the DOX molecules (Fig. 4.2).

The DOX-loaded magnetic luminescent porous Si microparticles exhibit a continuous release at physiological pH and temperature; 90% of the adsorbed drug is released in 9 days (Fig. 4.6c). Fluorescence microscope images indicate degradation of the porous Si matrix during the release period (Fig. 4.6d), and no particles were observable by optical microscopy after day 9 under these release conditions. The



degradation and dissolution process provides a mechanism by which the mesoporous drug carrier can be eliminated once it has performed its function, and this process can be monitored through the intrinsic luminescence of the porous Si matrix.

Free radical formation by means of cellular reduction of Fe (III) has been implicated in the observed cardiotoxicity of doxorubicin.<sup>46</sup> Cell viability assays were performed to determine if the iron oxide nanoparticles co-loaded with DOX increase the overall cytotoxicity of the formulation. HeLa (human cervical cancer) cells were incubated with free DOX together with iron oxide nanoparticles (using the same DOX:Fe<sub>3</sub>O<sub>4</sub> ratio as that in the loaded porous Si microparticles) for 48 h, and the cell viability was evaluated by MTS (3-(4,5-dimethylthiazol-2-yl)-5-(3-carboxymethoxyphenyl)-2-(4-sulfophenyl)-2H-tetrazolium) assay. No significant difference in cytotoxicity was observed for the experiments with or without Fe<sub>3</sub>O<sub>4</sub> nanoparticles (Fig. 4.8). This is attributed to the relatively small iron content in the microparticle formulations (Fe<sub>3</sub>O<sub>4</sub>:DOX mass ratio = 8:98).

The ability of the magnetic, luminescent porous Si microparticles to deliver DOX to HaLa cells *in vitro* under magnetic guidance was assessed. HeLa cells were seeded and cultured in a 60-mm Petri dish. A 0.10 mg quantity of DOX-loaded magnetic luminescent porous Si microparticles were added and attracted to one edge of the Petri dish using a rare earth permanent magnet. The Petri dish was agitated for 1 min with the magnet in place and then incubated for 24 h without agitation.

After incubation, the particles were still accumulated at the edge of the Petri dish in the vicinity of the magnet, and cell death was apparent in a small region (diameter ~1 cm) surrounding the particles (Figure 4.9a-d). Phase contrast microscope images obtained

along a radius of the Petri dish, beginning at a spot 1 mm from the magnet location and ending at the center of the dish (Fig. 4.9i), reveal the distance dependence of cell death. Few live cells, and a large quantity of light-refracting dead cells<sup>47-48</sup> are detected at the spot closest to the magnet, where the DOX-loaded microparticles are concentrated (Fig. 4.9a). The ratio of live to dead cells increases further away from the edge where the microparticles are located, and the ratio increases dramatically at a distance >10 mm from the microparticles; the center of the dish contains what appears to be only live cells (Fig. 4.9b-d). The phase contrast microscopy results are supported by fluorescence microscopy, using the fluorogenic viability stain calcein acetoxymethylester (Calcein AM), an intracellular esterase activity probe (Fig. 4.9e-h).<sup>49</sup> The data indicate that the porous Si microparticles can deliver and release the drug doxorubicin to kill HeLa cells, and that the effect can be localized under the influence of an external magnetic field and reduce unintended systemic toxicity of the drug.

As a control, a Petri dish containing HeLa cells was incubated with the same quantity of DOX-loaded magnetic, luminescent porous Si microparticles, but in the absence of an applied magnetic field. A uniformly dispersed and relatively lower density of dead cells was observed in the Petri dish after 24 h incubation in this control experiment (Fig. 4.9j and 4.9k). Similarly, HeLa cells incubated with  $1 \mu\text{g mL}^{-1}$  of free DOX (equal to the quantity of DOX released from 0.10 mg of microparticles within 24 h) showed dispersed cell death throughout the Petri dish, consistent with the known cytotoxicity of the drug (Fig. 4.10). To verify the localized death of cells was not caused by the particles themselves, drug-free magnetic, luminescent porous Si microparticles were incubated with HeLa cells under the influence of a magnet. No dead cells were

observed and the morphology of the cells remained normal (Supplementary Information, Fig. 4.11).

The effect of the quantity of particles on cell viability was also tested. A series of experiments employing 0.1, 0.2, and 0.4 mg of DOX-loaded microparticles were incubated in separate Petri dishes, each containing a similar quantity HeLa cells for 8 h under the influence of a magnetic field. The quantity of dead cells was observed to increase with increasing concentration of microparticles (Fig. 4.12).

#### **4.5 Conclusions**

In summary, microparticles containing both fluorescent and magnetic functions have been prepared by incorporating iron oxide nanoparticles into an intrinsically luminescent porous silicon matrix. A large quantity of doxorubicin (9.8% by mass) can be loaded into the composite microparticles, and a prolonged release of the drug is observed that is coincident with the physical degradation of the microparticulate carriers. Under the guidance of a magnetic field, *in vitro* localized delivery of the drug to cancer cells can be achieved, which provides a strategy to decrease the systemic toxicity of molecular drugs. Moreover, the low toxicity of the silicon and iron constituents of the composite microparticles, and the ability to load very dissimilar payloads into the porous Si matrix suggest that the approach may be of use for bioassay and therapeutic applications such as regional chemotherapy for the treatment of ovarian cancer through intraperitoneal administration.

#### **4.6 References**

1. Sathe, T.R., Agrawal, A. & Nie, S. Mesoporous Silica Beads Embedded with Semiconductor Quantum Dots and Iron Oxide Nanocrystals: Dual-Function Microcarriers for Optical Encoding and Magnetic Separation. *Anal. Chem.* **78**, 5627-5632 (2006).
2. Insin, N. et al. Incorporation of iron oxide nanoparticles and quantum dots into silica microspheres. *Acs Nano* **2**, 197-202 (2008).
3. Zebli, B., Susha, A.S., Sukhorukov, G.B., Rogach, A.L. & Parak, W.J. Magnetic targeting and cellular uptake of polymer microcapsules simultaneously functionalized with magnetic and luminescent nanocrystals. *Langmuir* **21**, 4262-4265 (2005).
4. Mandal, S.K. et al. Encapsulation of magnetic and fluorescent nanoparticles in emulsion droplets. *Langmuir* **21**, 4175-4179 (2005).
5. Yang, C.H. et al. Microfluidic assisted synthesis of multi-functional polycaprolactone microcapsules: incorporation of CdTe quantum dots, Fe<sub>3</sub>O<sub>4</sub> superparamagnetic nanoparticles and tamoxifen anticancer drugs. *Lab on a Chip* **9**, 961-965 (2009).
6. Corr, S.A., Rakovich, Y.P. & Gun'ko, Y.K. Multifunctional magnetic-fluorescent nanocomposites for biomedical applications. *Nanoscale Research Letters* **3**, 87-104 (2008).
7. Zhang, P.F. et al. Fabrication of fluorescent and magnetic multifunctional polystyrene microbeads with carboxyl ends. *Chemistry Letters* **36**, 1458-1459 (2007).
8. Mulvaney, S.P., Mattoussi, H.M. & Whitman, L.J. Incorporating fluorescent dyes and quantum dots into magnetic microbeads for immunoassays. *Biotechniques* **36**, 602-+ (2004).
9. Wilson, R., Spiller, D.G., Prior, I.A., Bhatt, R. & Hutchinson, A. Magnetic microspheres encoded with photoluminescent quantum dots for multiplexed detection. *Journal of Materials Chemistry* **17**, 4400-4406 (2007).
10. Pappas, D. & Wang, K. Cellular separations: A review of new challenges in analytical chemistry. *Analytica Chimica Acta* **601**, 26-35 (2007).
11. Dubus, S. et al. PCR-free DNA detection using a magnetic bead-supported polymeric transducer and microelectromagnetic traps. *Analytical Chemistry* **78**, 4457-4464 (2006).
12. Cao, Y.C. et al. Preparation of silica encapsulated quantum dot encoded beads for multiplex assay and its properties. *Analytical Biochemistry* **351**, 193-200 (2006).
13. Muller-Schulte, D., Schmitz-Rode, T. & Borm, P. Ultra-fast synthesis of magnetic and luminescent silica beads for versatile bioanalytical applications. *Journal of Magnetism and Magnetic Materials* **293**, 135-143 (2005).

14. Eastman, P.S. et al. Qdot nanobarcodes for multiplexed gene expression analysis. *Nano Letters* **6**, 1059-1064 (2006).
15. Anker, J.N., Koo, Y.E. & Kopelman, R. Magnetically controlled sensor swarms. *Sensors and Actuators B-Chemical* **121**, 83-92 (2007).
16. Ettenauer, M., Posniecek, T., Brandl, M., Weber, V. & Falkenhagen, D. Magnetic fluorescent microparticles as markers for particle transfer in extracorporeal blood purification. *Biomacromolecules* **8**, 3693-3696 (2007).
17. Quarta, A., Di Corato, R., Manna, L., Ragusa, A. & Pellegrino, T. Fluorescent-magnetic hybrid nanostructures: Preparation, properties, and applications in biology. *Ieee Transactions on Nanobioscience* **6**, 298-308 (2007).
18. Ma, Q., Wang, C. & Su, X.G. Synthesis and application of quantum dot-tagged fluorescent microbeads. *Journal of Nanoscience and Nanotechnology* **8**, 1138-1149 (2008).
19. Guo, J., Yang, W.L., Deng, Y.H., Wang, C.C. & Fu, S.K. Organic-dye-coupled magnetic nanoparticles encaged inside thermoresponsive PNIPAM microcapsules. *Small* **1**, 737-743 (2005).
20. Chan, W.C.W. & Nie, S. Quantum dot bioconjugates for ultrasensitive nonisotopic detection. *Science* **281**, 2016-2018 (1998).
21. Dubertret, B. et al. In vivo imaging of quantum dots encapsulated in phospholipid micelles. *Science* **298**, 1759-1762 (2002).
22. Derfus, A.M., Chan, W.C.W. & Bhatia, S.N. Intracellular delivery of quantum dots for live cell labeling and organelle tracking. *Advanced Materials* **16**, 961-+ (2004).
23. Bauer, S. et al. Size selective behavior of mesenchymal stem cells on ZrO<sub>2</sub> and TiO<sub>2</sub> nanotube arrays. *Integr. Biol.* **1**, 525-532 (2009).
24. Li, Z.F. & Ruskenstein, E. Water-soluble poly(acrylic acid) grafted luminescent silicon nanoparticles and their use as fluorescent biological staining labels. *Nano Lett.* **4**, 1463-1467 (2004).
25. Warner, J.H., Hoshino, A., Yamamoto, K. & Tilley, R.D. Water-soluble photoluminescent silicon quantum dots. *Angewandte Chemie-International Edition* **44**, 4550-4554 (2005).
26. Mangolini, L. & Kortshagen, U. Plasma-assisted synthesis of silicon nanocrystal inks. *Adv. Mater.* **19**, 2513-2519 (2007).

27. Park, J.-H. et al. Biodegradable luminescent porous silicon nanoparticles for in vivo applications. *Nature Mater.* **8**, 331-336 (2009).
28. Erogbogbo, F. et al. Biocompatible luminescent silicon quantum dots for imaging of cancer cells. *ACS Nano* **2**, 873-878 (2008).
29. Wang, L., Reipa, V. & Blasic, J. Silicon nanoparticles as a luminescent label to DNA. *Bioconjugate Chem.* **15**, 409-412 (2004).
30. Mertz, W. The Essential Trace-Elements. *Science* **213**, 1332-1338 (1981).
31. Yoo, Y.C. et al. Organ distribution of heavy metals in autopsy material from normal Korean. *Journal of Health Science* **48**, 186-194 (2002).
32. Bayliss, S.C., Heald, R., Fletcher, D.I. & Buckberry, L.D. The culture of mammalian cells on nanostructured silicon. *Adv. Mater.* **11**, 318-321 (1999).
33. Canham, L.T. Bioactive Silicon Structure Fabrication Through Nanoetching Techniques. *Adv. Mater.* **7**, 1033-1037 (1995).
34. Dorvee, J.R., Derfus, A.M., Bhatia, S.N. & Sailor, M.J. Manipulation of liquid droplets using amphiphilic, magnetic 1-D photonic crystal chaperones. *Nature Mater.* **3**, 896-899 (2004).
35. Tasciotti, E. et al. Mesoporous silicon particles as a multistage delivery system for imaging and therapeutic applications. *Nature Nanotechnology* **3**, 151-157 (2008).
36. Lin, V.S.Y., Motesharei, K., Dancil, K.P.S., Sailor, M.J. & Ghadiri, M.R. A porous silicon-based optical interferometric biosensor. *Science* **278**, 840-843 (1997).
37. Salonen, J., Kaukonen, A.M., Hirvonen, J. & Lehto, V.-P. Mesoporous Silicon in Drug Delivery Applications. *J. Pharm. Sci.* **97**, 632-653 (2008).
38. Godefroy, S. et al. Classification and control of the origin of photoluminescence from Si nanocrystals. *Nature Nanotechnology* **3**, 174-178 (2008).
39. Wilson, W.L., Szajowski, P.F. & Brus, L.E. Quantum Confinement in Size Selected, Surface-Oxidized Si Nanocrystals. *Science* **262**, 1242-1244 (1993).
40. Berger, P. et al. Preparation and properties of an aqueous ferrofluid. *J. Chem. Educ.* **76**, 943-948 (1999).
41. Park, J.-H. et al. Local Heating of Discrete Droplets Using Magnetic Porous Silicon-Based Photonic Crystals. *J. Am. Chem. Soc.* **128** 7938-7946 (2006).

42. Wolkin, M.V., Jorne, J., Fauchet, P.M., Allan, G. & Delerue, C. Electronic states and luminescence in porous silicon quantum dots: The role of oxygen. *Phys. Rev. Lett.* **82**, 197-200 (1999).
43. Prokopowicz, M. & Przyjazny, A. Synthesis of sol-gel mesoporous silica materials providing a slow release of doxorubicin. *J. Microencapsul.* **24**, 694-713 (2007).
44. Eksborg, S. Extraction of Daunorubicin and Doxorubicin and Their Hydroxyl Metabolites - Self-Association in Aqueous-Solution. *J. Pharm. Sci.* **67**, 782-785 (1978).
45. Wu, E.C. et al. Oxidation-Triggered Release of Fluorescent Molecules or Drugs from Mesoporous Si Microparticles. *ACS Nano* **2**, 2401-2409 (2008).
46. Minotti, G., Menna, P., Salvatorelli, E., Cairo, G. & Gianni, L. Anthracyclines: molecular advances and pharmacologic developments in antitumor activity and cardiotoxicity. *Pharmacol. Rev.* **56**, 185-229 (2004).
47. Scuderi, A.C., Paladino, G.M., Marino, C. & Trombetta, F. In vitro toxicity of netilmicin and ofloxacin on corneal epithelial cells. *Cornea* **22**, 468-472 (2003).
48. Alfonso, E.C. et al. Invitro Toxicity of Gentamicin to Corneal Epithelial-Cells. *Cornea* **9**, 55-61 (1990).
49. Wang, X.M. et al. A New Microcellular Cytotoxicity Test Based on Calcein Am Release. *Human Immunology* **37**, 264-270 (1993).
50. Gregg, S.J. & Sing, K.S.W. Adsorption, Surface Area and Porosity, Edn. 2nd. (Academic Press Inc., London; 1982).
51. Beijnen, J.H., Vanderhouwen, O. & Underberg, W.J.M. Aspects of the Degradation Kinetics of Doxorubicin in Aqueous-Solution. *International Journal of Pharmaceutics* **32**, 123-131 (1986).
52. Chavanpatil, M.D. et al. Polymer-surfactant nanoparticles for sustained release of water-soluble drugs. *J. Pharm. Sci.* **96**, 3379-3389 (2007).

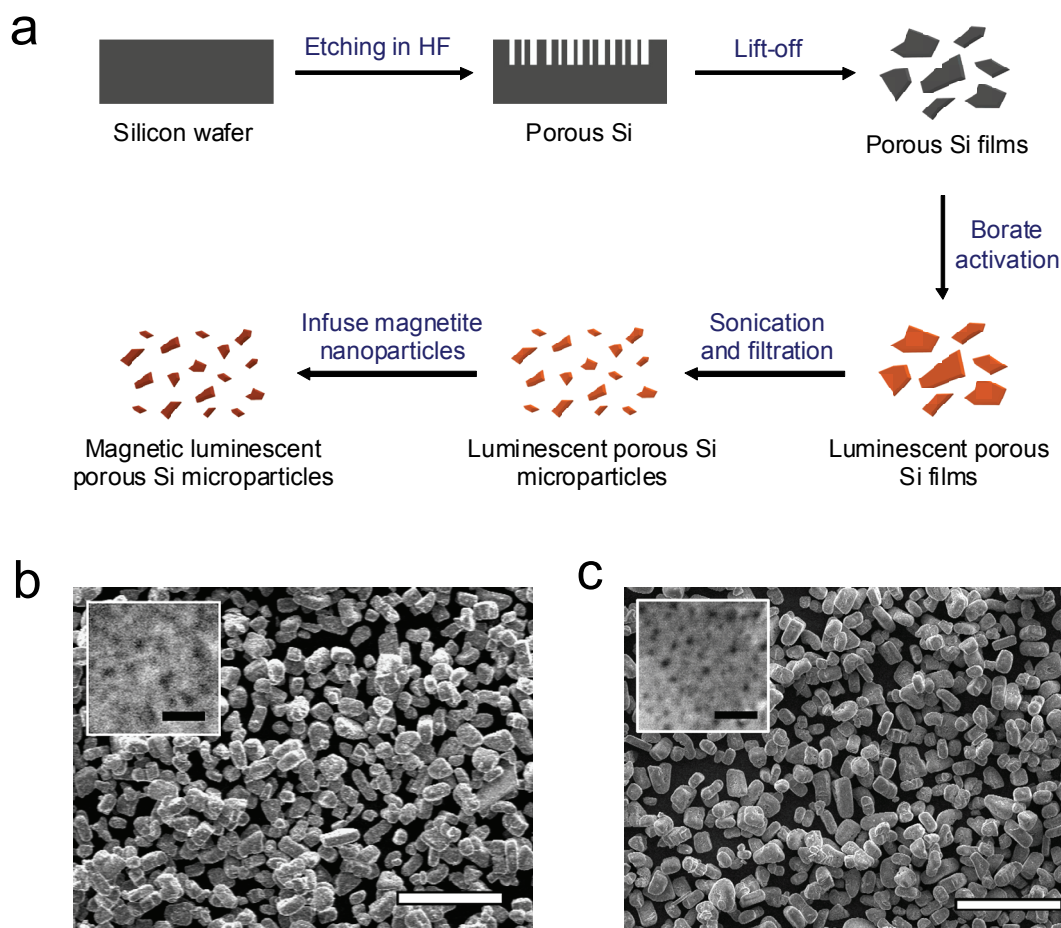


**Figure 4.1 Preparation and characterization of magnetic luminescent porous Si microparticles.** (a) Schematic depicting the synthesis of magnetic luminescent porous Si microparticles. A porous Si layer is first etched into a single-crystal Si wafer in ethanolic HF solution. The porous layer is removed from the substrate by application of a current pulse (“Lift-off”), and the freestanding porous Si fragments are then dispersed in a mild oxidant (aqueous borate) to activate photoluminescence. The luminescent fragments are then fractured into microparticles by ultrasonication. Finally, magnetite nanoparticles are loaded into the microparticles and locked into place by mild oxidation in air (100 °C). Scanning electron microscope (SEM) images of luminescent porous Si microparticles before (b) and after (c) loading of magnetite nanoparticles. Insets of both images reveal the porous nanostructures. Pore sizes before and after magnetite loading are  $21 \pm 4$  nm and  $12 \pm 3$  nm, respectively. The diameter of the magnetite nanoparticles used in this experiment is  $13 \pm 2$  nm. The scale bars are 100  $\mu\text{m}$  (100 nm for the insets).



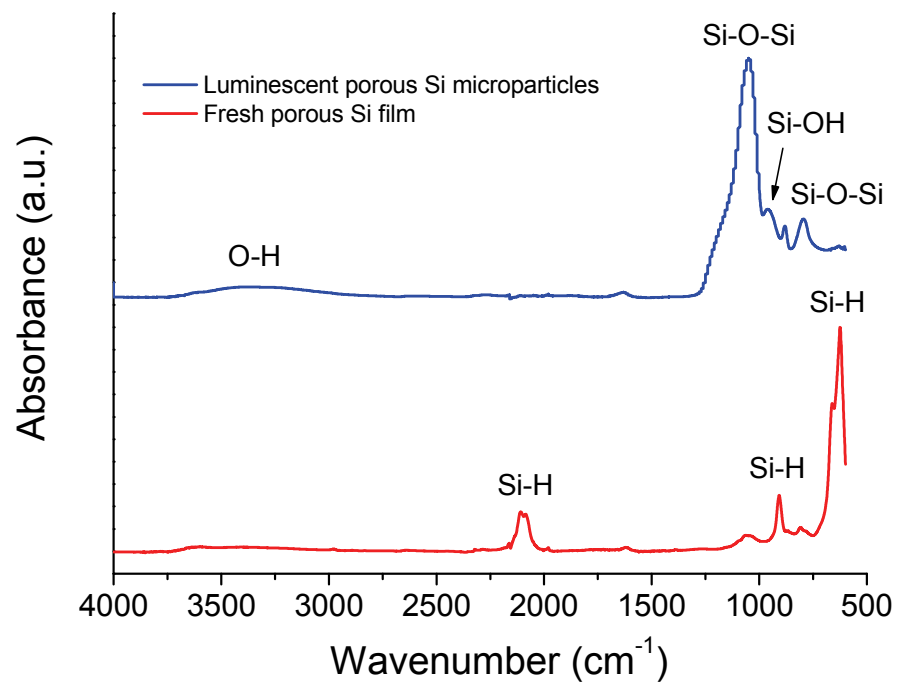


**Figure 4.2 FTIR spectra of porous silicon film and luminescent porous silicon microparticles, prior to loading of magnetite nanoparticles.** Oxidation of the porous Si film during microparticle production removes the surface Si-H species and generates a surface oxide.

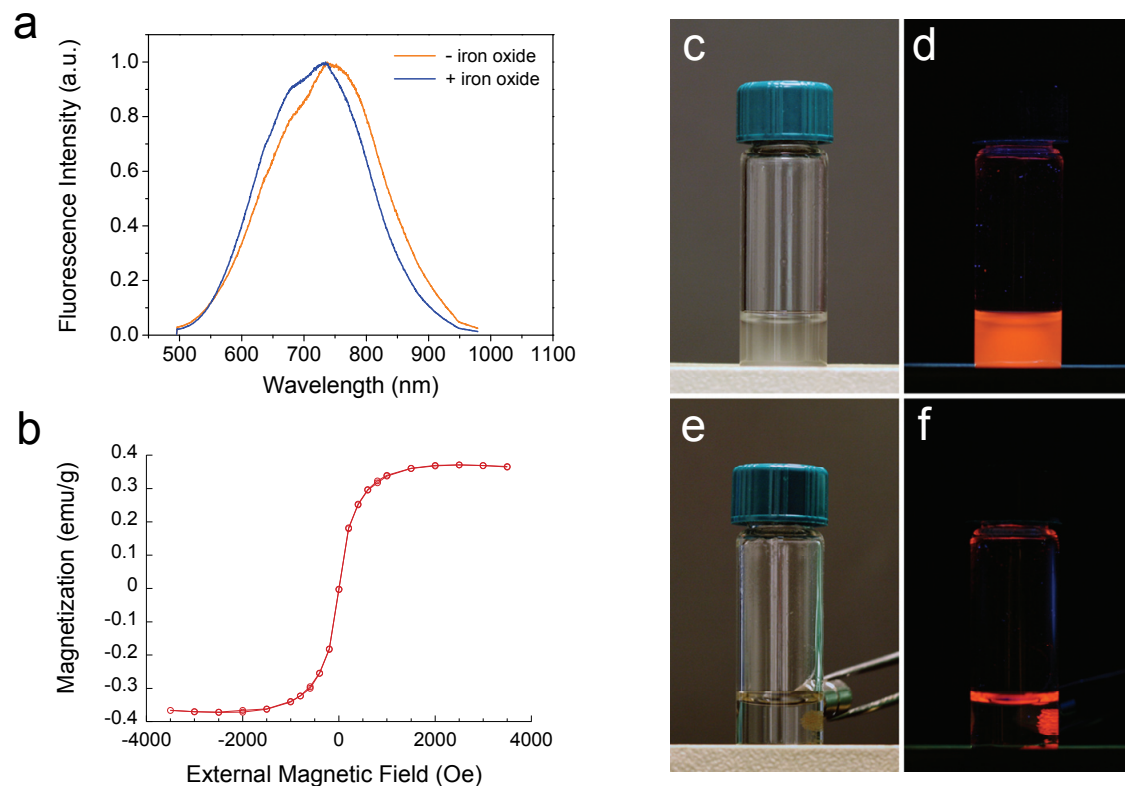


**Figure 4.3 Optical and magnetic characterization of porous Si microparticles.** (a) Photoluminescence emission spectra of porous Si microparticles before and after loading of magnetite nanoparticles (excitation wavelength 370 nm). The intrinsic photoluminescence of the Si nanostructure is not significantly altered upon loading of iron oxide nanoparticles. (b) Room-temperature magnetization curve of porous Si microparticles loaded with iron oxide (magnetite) nanoparticles. Magnetization data are based on total mass of the composite microparticles. (c) Photograph of magnetic, luminescent microparticles suspended in water. (d) Corresponding image obtained under UV light. (e) The microparticles from (c) are attracted to a rare earth magnet and can be pinned to the side of the glass vial. (f) Corresponding image obtained under UV light. The appearance of orange color at the meniscus of the liquid is due to luminescence light emanating from the pinned particles refracting at the air/water interface.

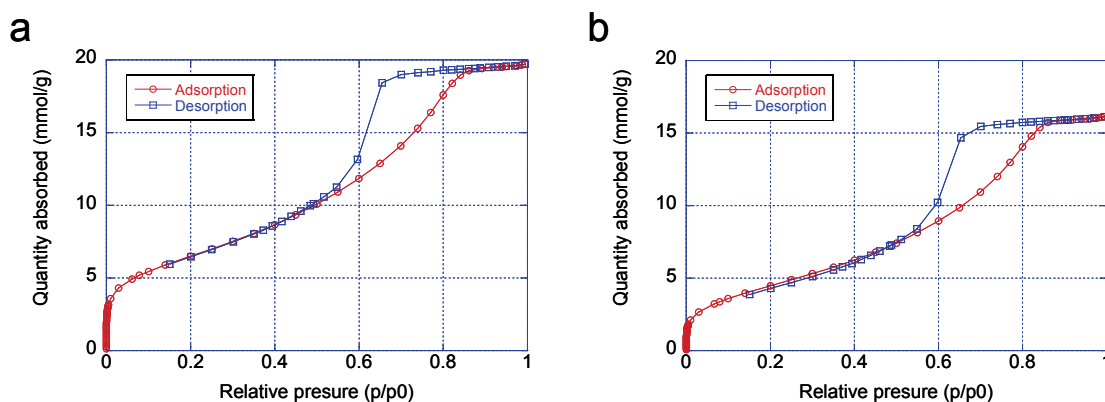


**Figure 4.4** N<sub>2</sub> adsorption/desorption isotherms of porous Si microparticles before (a) and after (b) loading of magnetite nanoparticles. The adsorption/desorption measurements reveal a type IV isotherm with a pronounced hysteresis loop, indicating the nanostructure of the microparticles is mesoporous (pore diameters 2-50 nm). The specific surface area (BET method) and pore volume (BJH method) are 520 m<sup>2</sup>/g and 0.712 cm<sup>3</sup>/g, respectively for the material before loading of magnetite. After loading of magnetite, the specific surface area (373 m<sup>2</sup>/g) and pore volume (0.577 cm<sup>3</sup>/g) are decreased. Based on the BJH model, the average pore size of the luminescent porous Si microparticles does not change significantly upon loading of iron oxide nanoparticles: calculated diameters before and after loading are 4.67 and 4.95 nm, respectively. Note: the calculated pore sizes are different from the SEM results because the BJH model includes the branched pores inside the microparticles and it may not be an ideal fitting for this material.

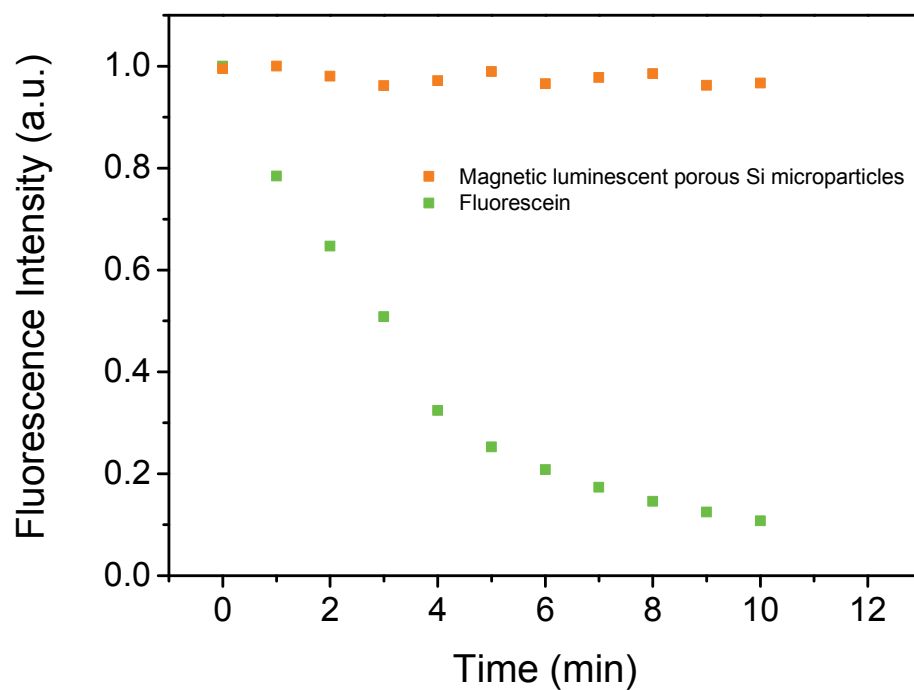


**Figure 4.5 Photostability of porous Si microparticles.** Intensity of fluorescence as a function of time for magnetic, luminescent porous Si microparticles compared with the organic dye fluorescein absorbed on silica microbeads. Both samples were dispersed on glass slides and exposed to a 100 W mercury lamp for the duration of the experiment. The significant decrease of fluorescence intensity of the fluorescein sample is attributed to photobleaching induced by oxygen and oxygen-induced free radicals.

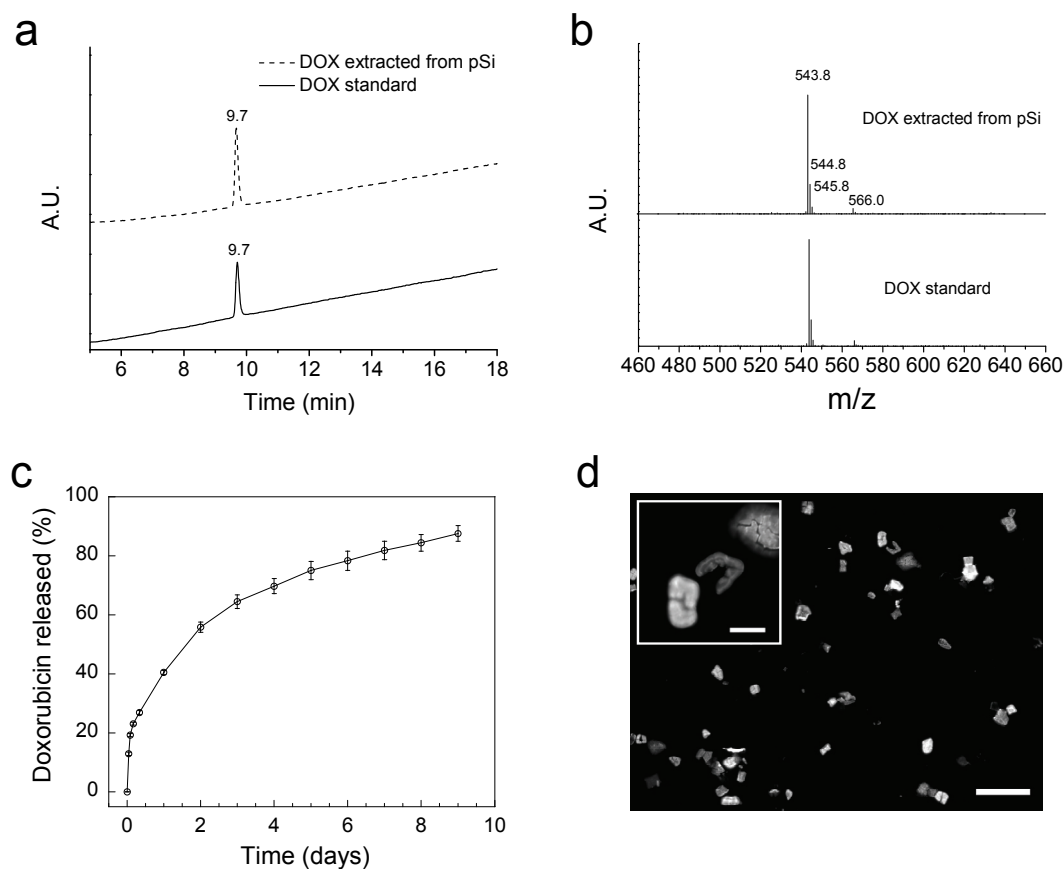


**Figure 4.6 Characterization of DOX loaded magnetic, luminescent porous Si microparticles.** (a) HPLC analysis of DOX standard and DOX extracted from magnetic luminescent porous Si microparticles (UV-Vis detection wavelength at 480 nm). (b) Mass spectra of above samples separated by HPLC at retention time of 9.7 min. The signals at  $m/z$  543.8 and 566.0 are  $[\text{DOX} + \text{H}]^+$  and  $[\text{DOX} + \text{Na}]^+$ , respectively; the signals at  $m/z$  544.8 and 545.8 correspond to the expected isotopic pattern for  $[\text{DOX} + \text{H}]^+$ . (c) Cumulative release of DOX from magnetic luminescent porous Si microparticles in aqueous PBS buffer solution (error bars indicate 1 S.D.). Data obtained from optical absorbance measurement (480 nm) of the supernatant. (d) Fluorescence microscope images of the microparticles after 6 days under release conditions (excitation wavelength 360 nm, emission filter bandpass  $720 \pm 80$  nm). Scale bar is 100  $\mu\text{m}$  (20  $\mu\text{m}$  for the inset).

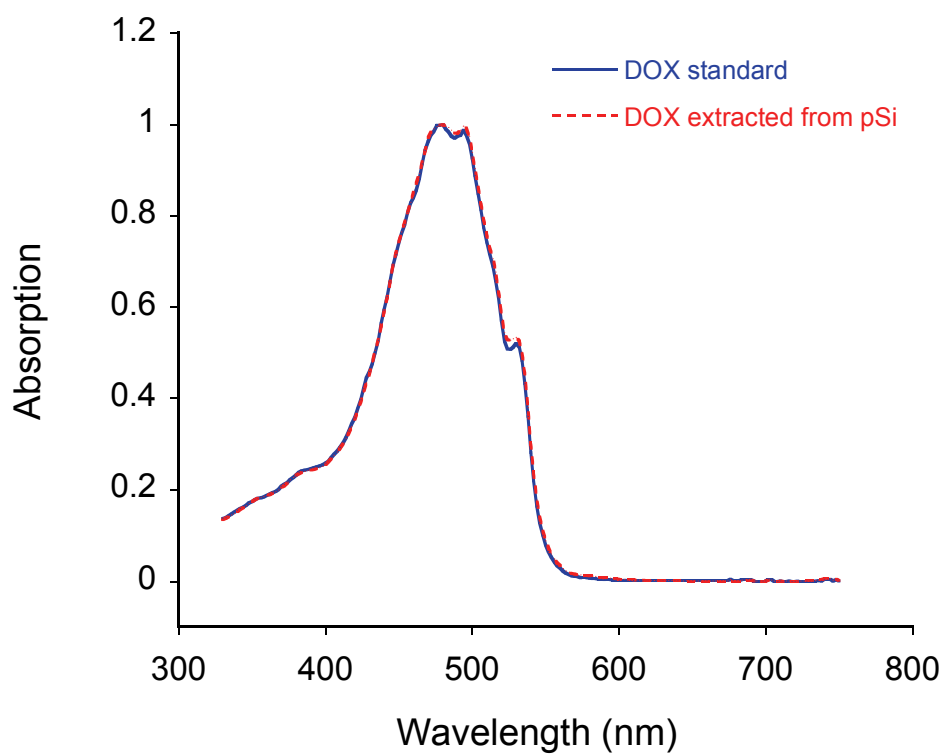


**Figure 4.7** UV-Vis absorption spectra of DOX standard in ethanol and DOX extracted from DOX loaded magnetic luminescent porous Si microparticles in ethanol. The spectra are normalized for comparison.

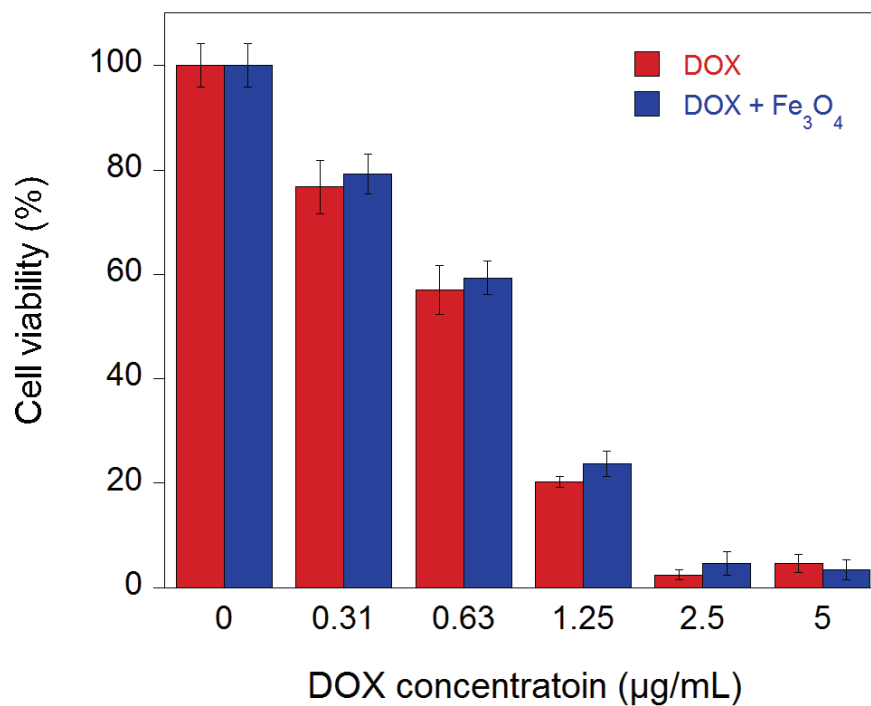


**Figure 4.8** In vitro cytotoxicity of doxorubicin (DOX) alone compared to DOX plus iron oxide nanoparticles towards HeLa cells. The mass ratio of DOX to Fe<sub>3</sub>O<sub>4</sub> is 98:8, which is the same as that loaded in the porous Si particles. The cytotoxicity was determined by MTS assay.

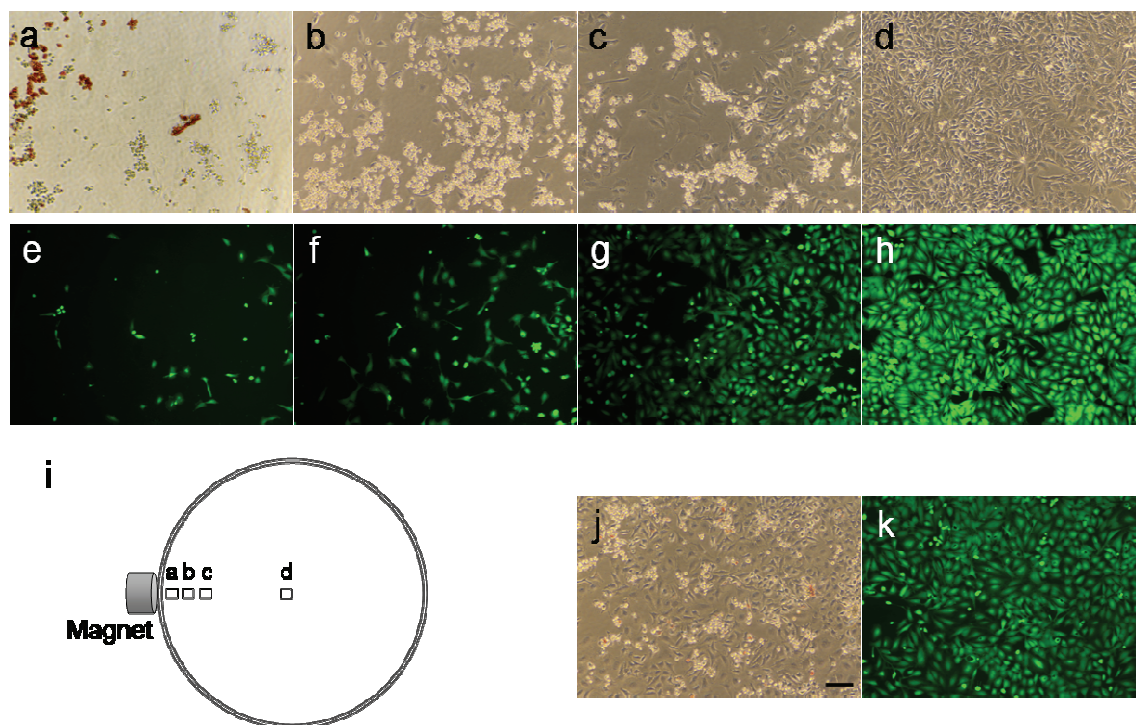


**Figure 4.9 Magnetic field guided delivery of DOX using magnetic luminescent porous Si microparticles.** (a-d) Phase contrast microscope images of HeLa cells 24 h after incubation with DOX-loaded magnetic luminescent porous Si microparticles, showing magnetically guided delivery of doxorubicin. The position of each image relative to the external magnet is depicted in image (i). The microparticles were attracted to an edge of the Petri dish during incubation by means of a rare earth magnet placed external to the dish. (e-h) Fluorescence microscope images of HeLa cells stained with Calcein AM. Each image e-h is obtained at the approximate location as image a-d, respectively. (j, k) Phase contrast and fluorescence microscope images of a control dish of HeLa cells (24 h incubation with DOX-loaded magnetic luminescent porous Si microparticles) obtained without magnetic guidance. The image is representative of the entire dish, which shows no significant variation in cell morphology or fluorescence intensity as a function of position. Scale bar for all images is 100  $\mu\text{m}$ .



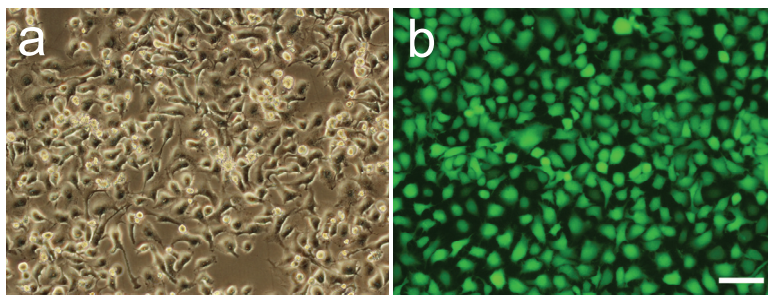


**Figure 4.10 (a) Phase contrast and (b) fluorescence microscope images of a control dish of HeLa cells (24 h incubation with 1  $\mu\text{g}/\text{mL}$  free DOX).** The image is representative of the entire dish, which shows no significant variation in cell morphology or fluorescence intensity as a function of position. Scale bar for all images is 100  $\mu\text{m}$ .

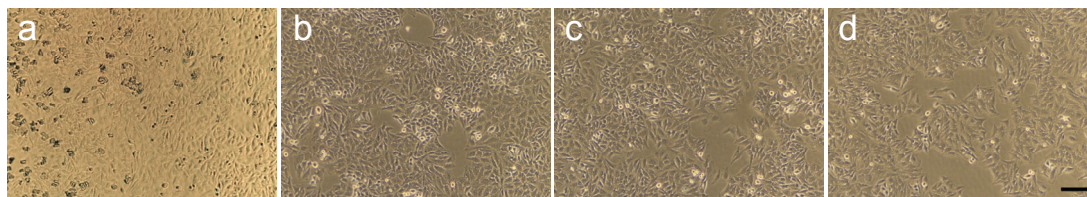


**Figure 4.11 Phase contrast microscope images of HeLa cells after 24 h incubation with drug-free magnetic, luminescent porous Si microparticles.** The particles were accumulated at the edge of the Petri dish under the influence of a magnet, similar to the experiment represented by Figure 4. Images (a-d) were obtained at the same locations of the Petri dish as illustrated in Figure 4i. Scale bar is 100  $\mu\text{m}$ .

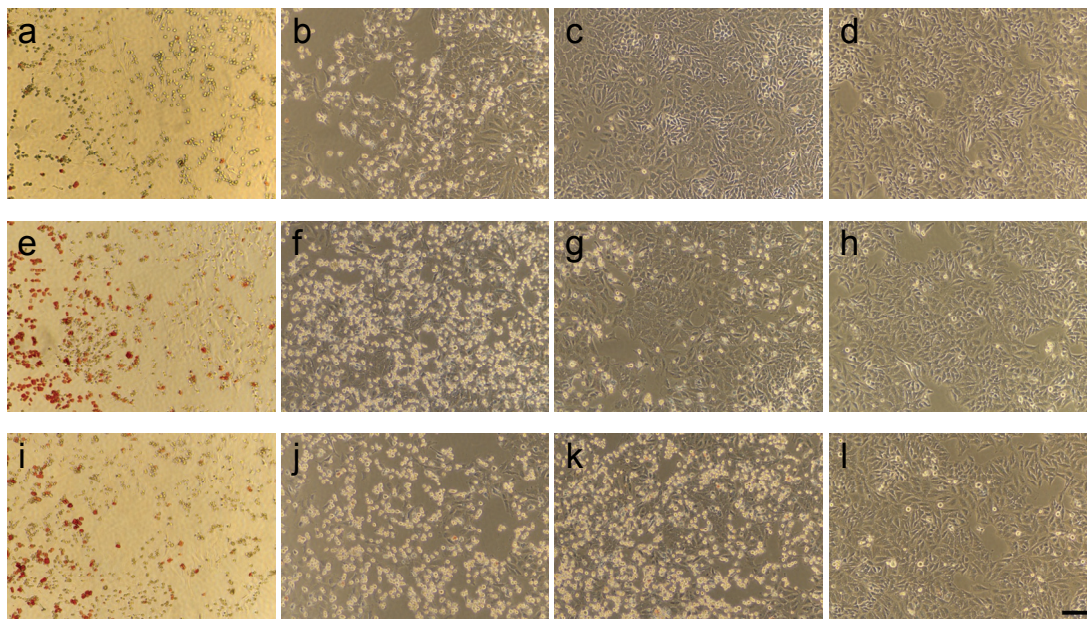


**Figure 4.12** Phase contrast microscope images of HeLa cells after 8 h incubation with different quantities of DOX-loaded magnetic, luminescent porous Si microparticles. (a-d): 0.1 mg particles; (e-h): 0.2 mg; (i-l): 0.4 mg. The microparticles, visible as reddish flakes on the left hand side of images (a), (e), and (i), were attracted with a magnet to an edge of the Petri dish during incubation. Images (a-d) were obtained at different locations of the Petri dish as illustrated in Figure 4i. Images (e-h) and (i-l) were obtained at locations corresponding to (a-d), respectively. Scale bar is 100  $\mu\text{m}$ .

Chapter four, in part of full, is a reprint (with co-author permission) of the material as it appears in the following publication: **Gu, Luo.**; Park, Ji-Ho; Duong, Kim H.; Ruoslahti, Erkki; Sailor, Michael J., “Magnetic Luminescent Porous Silicon Microparticles for Localized Delivery of Molecular Drug Payloads”. *Small* 2010, 6 (22), 2546-2552. The author of this dissertation is the primary author of this manuscript.

## **CHAPTER V:**

### **The Phototoxicity of Porous Silicon Nanoparticle**

#### **Photosensitizers against Cancer Cells**

## 5.1 Abstract

Porous Si nanoparticles, prepared from electrochemically etched single crystal Si wafers, function as photosensitizers to generate  $^1\text{O}_2$  in ethanol and in aqueous media. The preparation conditions for the porous Si nanoparticles were optimized to maximize (1) the yield of material; (2) its quantum yield of  $^1\text{O}_2$  production; and (3) its *in vitro* degradation properties. The optimal formulation was determined to consist of nanoparticles  $146 \pm 7$  nm in diameter, with nominal pore sizes of  $12 \pm 4$  nm. The quantum yield for  $^1\text{O}_2$  production is  $0.10 \pm 0.02$  in ethanol and  $0.17 \pm 0.01$  in  $\text{H}_2\text{O}$ . Human cervical cancer HeLa cells treated with  $200 \mu\text{g/mL}$  porous Si nanoparticles and exposed to  $48 \text{ J/cm}^2$  white light (infrared filtered,  $80 \text{ mW/cm}^2$  for 10 min) exhibit  $> 40\%$  cell death *in vitro*, while controls containing no nanoparticles show 10% cell death. The dark control experiment only yields  $< 2\%$  cytotoxicity.

## 5.2 Introduction

Photodynamic therapy (PDT) can be an effective clinical treatment for certain types of cancer because of its relatively low systemic toxicity and its non-invasive nature.<sup>1</sup> The operational principle for PDT involves the conversion of ground-state molecular oxygen ( $^3\text{O}_2$ ) to singlet oxygen ( $^1\text{O}_2$ ) by energy transfer from a photoexcited molecule (a photosensitizer). The highly reactive  $^1\text{O}_2$  causes lethal damage to cancer cells and destruction of tumor vasculature.<sup>2,3</sup> Despite the advantages of the therapy itself, photosensitizers in use today display toxic or other side effects that limit their use. For example, the first-generation photosensitizer Photofrin® lacks a long wavelength absorption band and it exhibits prolonged residence time in the normal tissues of the

body. If not protected from sunlight and other forms of bright light, the skin and eyes of the patient can become severely damaged. It takes only a few minutes of exposure to induce a light sensitivity response, and this sensitivity can persist for 4–12 weeks after administration of the therapeutic.<sup>4</sup> More promising second-generation photosensitizers, such as Photosens®, are based on a phthalocyanine motif with a strong long wavelength absorption band. However, most phthalocyanines and their relatives are hydrophobic, requiring delivery systems for clinical use,<sup>5,6</sup> and patient photosensitivity remains a problem.<sup>7</sup> Third-generation photosensitizers involve second-generation photosensitizers modified with targeting molecules for better tumor selectivity.<sup>8</sup>

Recent studies using nanoparticle hosts containing conventional organic photosensitizers have demonstrated improved water solubility and biocompatibility.<sup>9-15</sup> However, most of these approaches use non-functional silica or polymer-based nanomaterials as the carriers, and there is still a risk of the photosensitizer payload leaking from the carriers into the body before reaching the target. Nanomaterials that can intrinsically generate  $^1\text{O}_2$  when photoexcited, such as  $\text{TiO}_2$ <sup>16,17</sup> and quantum dots,<sup>18,19</sup> can overcome such problems. However, concerns regarding biodegradability,<sup>20</sup> toxicity of degradation by-products<sup>21-24</sup> and relatively low  $^1\text{O}_2$  quantum yield<sup>18</sup> of such materials have impeded their clinical application.

It has been recently discovered that the quantum-confined domains in porous Si films can generate  $^1\text{O}_2$  when excited with visible light, and this energy transfer process is very efficient due to the extremely long lifetime of the excitons and the large specific surface area of porous Si.<sup>25,26</sup> Porous Si has low toxicity, and most importantly, it is biodegradable and biocompatible.<sup>27-31</sup> Silicon is a common trace element in humans and

the primary biodegradation product of porous Si, orthosilicic acid ( $\text{Si}(\text{OH})_4$ ), is the form predominantly absorbed by humans and is naturally present in numerous tissues.<sup>32-34</sup> We have previously found that porous Si nanoparticles administered *in vivo* (mouse model) can accumulate in tumors and then degrade into components that are rapidly cleared by the kidneys in a relatively short period of time.<sup>35</sup> In this study, we show that porous Si nanoparticles can generate  $^1\text{O}_2$  and kill cancer cells *in vitro* following illumination with a commercial halogen light or a light-emitting diode (LED) panel. This study represents the first *in vitro* demonstration of photodynamic killing of cancer cells using porous Si nanoparticles, and it illustrates the potential for this nanomaterial as a non-toxic, biodegradable alternative to molecular PDT agents used in the clinic today.

### 5.3 Experimental

*Reagents:* Boron-doped p-type Si wafers (0.0008-0.0012 $\Omega$ -cm resistivity, <100> orientation) were obtained from Siltronix. Aqueous hydrofluoric acid was purchased from EMD Chemicals. Methylene blue (MB), Rose Bengal (RB) and 1,3-diphenylisobenzofuran (DPBF) were obtained from Sigma-Aldrich Chemicals. Singlet oxygen sensor green (SOSG) reagent was purchased from Molecular Probes, inc. RPMI-1640 cell media, fetal bovine serum (FBS), trypsin and Dulbecco's phosphate buffered saline (DPBS) were obtained from Thermo Scientific. CellTiter 96® Aqueous MTS Reagent Powder was purchased from Promega.

*Preparation of Porous Si Nanoparticles:* Porous Si nanoparticles were prepared by anodic electrochemical etch of Si in 3:1 (v/v) 48 % aqueous HF:ethanol. A Teflon etch



cell that exposed  $8.8 \text{ cm}^2$  of the polished Si wafer surface was used. Samples were etched at a constant current density of 50, 100, 200, 300, or  $400 \text{ mA/cm}^2$  for 150 s. The porous Si film was then removed from the crystalline Si substrate by application of a current pulse of  $4 \text{ mA/cm}^2$  for 250 s in a solution of 3.3% aqueous HF in ethanol. The freestanding porous silicon film was fractured into nanoparticles by ultrasonication for  $\sim 16$  h in ethanol under a nitrogen gas atmosphere. The large fragments were removed by filtration through a  $0.45 \text{ }\mu\text{m}$  nylon filter membrane (GE Osmonics Labstore). The porous Si nanoparticles were collected on a 100 kDa Amicon Ultra-4 membrane (Millipore) and washed 3 times with ethanol. FT-IR spectra were acquired using a Nicolet 6700 spectrometer equipped with a Smart-iTR attenuated total reflectance attachment.

*Characterization of Porous Si Nanoparticles:* Scanning electron microscope (SEM) images were obtained using a Philips XL30 field emission ESEM. Dynamic light scattering (Zetasizer Nano ZS90, Malvern Instruments) was used to determine the hydrodynamic size of the porous Si nanoparticles.

*Detection of Singlet Oxygen by Chemical Trapping:* DPBF was used as a  $^1\text{O}_2$  trapping reagent in ethanol solution. In a typical experiment, 2 mL of an ethanol solution containing 0.08 mM DPBF and  $10 \text{ }\mu\text{g/mL}$  porous Si nanoparticles was placed in a sealed quartz cuvette. A 150 W tungsten halogen lamp (Fiber-Lite MI-150, Dolan-Jenner Industries) filtered through a short pass infrared and a bandpass filter (454 – 500 nm) was used as the light source. The absorbance of the solution at 410 nm was measured every 1 min for a 10 min period with an ultraviolet-visible spectrophotometer (SpectraMax Plus

384, Molecular Devices). The decrease of the absorbance caused by photobleaching of DPBF was measured and corrected in all experiments. The natural logarithm values of absorption of DPBF at 410 nm were plotted against the irradiation time and fit by a first-order linear least-squares model to get the decay rate of the photosensitized process. The  $^1\text{O}_2$  quantum yield of porous Si nanoparticles in ethanol was calculated using rose bengal as a standard ( $\Phi_{\text{RB}} = 0.86$  in ethanol). The  $^1\text{O}_2$  quantum yield of porous Si nanoparticles in aqueous solution was determined using the SOSG assay for  $^1\text{O}_2$ ; the fluorescence spectrum (LS50B spectrofluorimeter, Perkin-Elmer instruments) was integrated in the wavelength range from 500 nm to 570 nm for solutions containing 5  $\mu\text{M}$  SOSG and 10  $\mu\text{g/mL}$  PSiNP in water, using an excitation wavelength of 488 nm. The absolute quantum yield for  $^1\text{O}_2$  generation by porous Si nanoparticles in  $\text{H}_2\text{O}$  was calculated using rose bengal as a standard and assuming  $\Phi_{\text{RB}} = 0.75$  in  $\text{H}_2\text{O}$ .

*Cell Culture and In Vitro PDT:* Human cervical cancer HeLa cells were cultured in RPMI 1640 medium supplemented with 10% fetal bovine serum (FBS) at 37 °C in a 5%  $\text{CO}_2$  atmosphere. For *in vitro* PDT tests, the cells were seeded in 96-well plates at a density of  $1 \times 10^4$  cells/well and cultured for 24 h. An aliquot of 200 mL of PBS buffer containing 0, 50, 100 or 200  $\mu\text{g/mL}$  of porous Si nanoparticles was injected, and immediately afterwards the cells were exposed to a 150 W tungsten halogen lamp filtered with a shortpass infrared (IR) filter for 10 min at different intensities to apply a total light dose of 30 or 48  $\text{J/cm}^2$ . Alternatively, an LED panel ( $\lambda_{\text{max}} = 458$  nm, FWHM = 22 nm) at a light dose of 6, 12, or 18  $\text{J/cm}^2$  was used. The control cells were maintained in the dark for the same period of time. After exposure, the buffer containing the nanoparticles was

removed, the cells were washed twice with PBS solution, and they were then either subjected to cell viability assays or placed under the microscope for observation of morphology. For the cell viability experiments, the plates were further incubated in RPMI 1640 medium supplemented with 10% FBS for 24 h and assayed using the CellTiter 96® AQueous One Solution Cell Proliferation (MTS) assay according to the instructions provided by the vendor.

## 5.4 Results and Discussion

Porous Si nanoparticles were prepared by electrochemical etching of single-crystal silicon wafers in ethanolic HF solution, lift-off the porous Si film, ultrasonication, and finally filtration of the formed particles through a 0.45  $\mu\text{m}$  membrane (Fig. 5.1). To study the effect of the pore size in the nanoparticles on the generation of singlet oxygen, porous Si nanoparticles with different average pore sizes (7.9–17.6 nm) were prepared by using various etching current densities from 50  $\text{mA}/\text{cm}^2$  to 400  $\text{mA}/\text{cm}^2$  (Table 5.1). The as-prepared nanoparticles possess a hydrogen-terminated surface (Fig. 5.2), and their average hydrodynamic size measured by dynamic light scattering (DLS) is  $\sim 100$ –200 nm. Scanning electron microscope (SEM) images reveal a well-ordered mesoporous nanostructure (Table 5.1).

The generation of  $^1\text{O}_2$  by photoexcited porous Si nanoparticles in ethanol was detected using the chemical trapping reagent 1,3-diphenylisobenzofuran (DPBF). DPBF reacts with  $^1\text{O}_2$  irreversibly, undergoing a 1,4-cycloaddition that is detected as a decrease in the intensity of the DPBF absorption band at 410 nm.<sup>36,37</sup> As shown in Fig. 5.3a, the absorption intensity of the solution containing porous Si nanoparticles and DPBF

decreases gradually as a function of time under light irradiation (halogen lamp fitted with an IR filter and a 454–500 nm bandpass filter), while the change is negligibly small in the absence of light (Fig. 5.3b). DPBF was observed to undergo slight decomposition under the irradiation conditions (in air), even in the absence of porous Si nanoparticles (Fig. 5.4). The data presented here are corrected for this self-photobleaching. To confirm that the decomposition of DPBF is caused by  $^1\text{O}_2$  instead of a direct reaction with photoexcited porous Si nanoparticles, the photolysis reaction was carried out in a solution depleted of  $\text{O}_2$  (by  $\text{N}_2$  purge for 30 min). The decrease of the absorption of DPBF in  $\text{O}_2$ -depleted solution was negligible compared to that of the air-saturated solution (Fig 5.3d). The dependence of the reaction on dissolved  $\text{O}_2$  provides clear evidence that  $^1\text{O}_2$  is generated by the porous Si nanoparticles in the photosensitized process. The photosensitization reaction accelerates with increasing nanoparticle concentration (Fig. 5.5).

The quantum yield for  $^1\text{O}_2$  generation by porous Si nanoparticles was determined using a comparative method.<sup>38</sup> A plot of optical absorbance at 410 nm as a function of irradiation time is consistent with a first order reaction (Fig. 5.3c). The  $^1\text{O}_2$  quantum yield was calculated by comparison with a standard photosensitizer,<sup>39</sup>

$$\Phi_{\text{PSiNP}} = \Phi_s \cdot \frac{k_{\text{PSiNP}}}{I_{\text{PSiNP}}} \cdot \frac{I_s}{k_s} \quad (1)$$

where  $k_{\text{PSiNP}}$  and  $k_s$  are the rate constants for decomposition of DPBF by porous Si nanoparticles and by a standard photosensitizer, respectively.  $I_{\text{PSiNP}}$  and  $I_s$  represent light absorbed by the porous Si nanoparticles and by the photosensitizer standard, respectively, which are determined by integration of the optical absorption bands in the wavelength

range 454–500 nm. In order to evaluate the method and our experimental setup, the  $^1\text{O}_2$  quantum yield of methylene blue (MB) was determined to be 0.53 using rose bengal (RB,  $\Phi_{\text{RB}} = 0.86$  in ethanol<sup>40</sup>) as a standard, which is in good agreement with the published data ( $\Phi_{\text{MB}} = 0.52$  in ethanol<sup>40</sup>). Similarly, by taking RB as a standard, the  $^1\text{O}_2$  quantum yield of the porous Si nanoparticles as a function of average pore size was determined. As reported in Table 5.1, the intermediate pore size of 9.2~11.8 nm appears to be optimal for  $^1\text{O}_2$  generation. In the present study, nanoparticles made using an etching current density of 200 mA/cm<sup>2</sup> were chosen for the *in vitro* tests, because this preparation provided a compromise between maximizing the total yield of nanoparticles and maximizing the  $^1\text{O}_2$  quantum yield.

Singlet oxygen generation by porous Si has been studied,<sup>26</sup> and it is thought to undergo the following processes: (1) porous Si is photoexcited into a singlet energy state; (2) the material undergoes intersystem crossing to a long-lived triplet state; (3) energy transfer from the excited triplet state on porous Si to the triplet ground state of oxygen ( $^3\text{O}_2$ ), generating singlet oxygen ( $^1\text{O}_2$ ). The  $^1\text{O}_2$  excited state can then relax back to the ground state  $^3\text{O}_2$  via radiative or nonradiative (collisional) deactivation.<sup>26</sup> For gas-phase oxygen, the efficiency of  $^1\text{O}_2$  generation has been reported to increase with increasing porosity of the porous Si film.<sup>41</sup> Moreover, for gas-phase oxygen the radiative deexcitation route dominates, while nonradiative relaxation is the main relaxation pathway for  $^1\text{O}_2$  in solution.<sup>42</sup> In the present work, no specific dependence of  $^1\text{O}_2$  quantum yield on porosity was observed. This is attributed to the process by which the nanoparticles are prepared; ultrasonic fracture of the porous Si film into particles changes

the pore morphology and it generates fresh reactive surfaces that are readily oxidized. The degree of oxidation is dependent on pore size,<sup>43</sup> and surface oxides may enhance nonradiative pathways and hinder triplet-triplet energy transfer.<sup>44</sup>

The concentration of  $^1\text{O}_2$  in aqueous solution was further quantified using singlet oxygen sensor green (SOSG) reagent, which is highly selective for  $^1\text{O}_2$  and does not have any appreciable response to hydroxyl radical ( $\cdot\text{OH}$ ) or superoxide ( $\cdot\text{O}_2^-$ ) species.<sup>45</sup> In the presence of  $^1\text{O}_2$ , SOSG emits strong green fluorescence (excitation/emission maxima  $\sim 504/525$  nm), which corresponds to the formation of an endoperoxide by the reaction of  $^1\text{O}_2$  with the anthracene component of SOSG.<sup>46</sup> When the assay solution containing porous Si nanoparticles was irradiated with light from a tungsten halogen lamp (filtered through a short pass infrared and a 454–500 nm bandpass filters), the fluorescence emission intensity at 520 nm was observed to increase gradually (Fig. 5.6a). An equivalent sample maintained in the dark showed no increase in fluorescence signal (Fig. 5.6b). The rate of SOSG endoperoxide formation followed first order kinetics (Fig. 5.7),<sup>47</sup> and the quantum yield for  $^1\text{O}_2$  generation by porous Si nanoparticles in water was determined to be  $0.17 \pm 0.01$  using Eq. 1 (relative to  $\Phi_{\text{RB}} = 0.75$  in  $\text{H}_2\text{O}$ <sup>40</sup>). In support of the conclusion that the observed signal was due to  $^1\text{O}_2$  generation from photoexcited porous Si nanoparticles, no increase in fluorescence was observed for an irradiated sample that had been deoxygenated (by sparging with nitrogen gas for 30 min), or that contained SOSG alone (no nanoparticles, Fig. 5.7).

The phototoxicity of porous Si nanoparticles toward cancer cells was tested *in vitro* using the MTS (3-(4,5-dimethylthiazol-2-yl)-5-(3-carboxymethoxyphenyl)-2-(4-sulfophenyl)-2H-tetrazolium) cell viability assay. HeLa cells were irradiated for 10 min

in a PBS buffer containing 0, 50, 100 and 200  $\mu\text{g/mL}$  porous Si nanoparticles. As shown in Fig. 5.8, cell viability decreased with increasing concentration of porous Si nanoparticles and with increasing light intensity. The maximum degree of cell death observed with the experimental protocol of Fig. 5.8 was  $\sim 41\%$ . Minimal cytotoxicity was observed in the dark, even with porous Si nanoparticle concentrations as large as 200  $\mu\text{g/mL}$ , indicating a low level of dark toxicity for the nanoparticles themselves. The morphology of HeLa cells exposed to 100  $\mu\text{g/mL}$  porous Si nanoparticles in the dark for 10 min, or with light exposure up to 60  $\text{J/cm}^2$  (100  $\text{mw/cm}^2$ , 10 min) but without nanoparticles, showed no significant change compared to an untreated control (Fig. 5.9). However, under the same light exposure conditions, HeLa cells in the presence of porous Si nanoparticles lost their adherent nature and shrank to assume a spherical-like morphology (Fig. 5.9d). Similar phototoxicity characteristics were observed using a blue ( $\lambda_{\text{max}} = 458 \text{ nm}$ , FWHM = 22 nm) LED panel as the light source.

## 5.5 Conclusions

In conclusion, porous Si nanoparticles function as intrinsic photosensitizers to generate measurable quantities of  $^1\text{O}_2$ . The measured quantum yield of  $^1\text{O}_2$  by photoexcited porous Si nanoparticles was  $0.10 \pm 0.02$  in ethanol and  $0.17 \pm 0.01$  in  $\text{H}_2\text{O}$ . Porous Si nanoparticles irradiated with blue light show phototoxicity toward human cancer cells (HeLa) *in vitro*. Although the porous Si nanoparticles used in this study are not as effective as conventional molecular PDT agents (based on  $\text{IC}_{50}$  values), they overcome some of their shortcomings: (1) the nanoparticles are not cytotoxic in the absence of light; and (2) they degrade quickly to apparently non-toxic byproducts in

buffer or culture media, minimizing the possibility of long-term patient photosensitivity. However, the rapid dissolution of the nanoparticle formulation used in this study limits its prospects for *in vivo* studies.

## 5.6 References

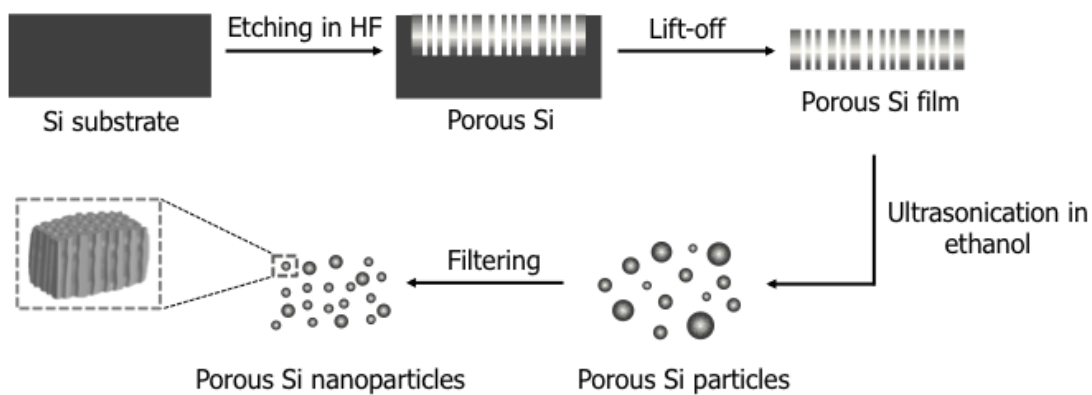
1. Sharman, W. M.; Allen, C. M.; Van Lier, J. E. Photodynamic Therapeutics: Basic Principles and Clinical Applications. *Drug Discovery Today* **1999**, *4*, 507-517.
2. Dougherty, T. J.; Gomer, C. J.; Henderson, B. W.; Jori, G.; Kessel, D.; Korbek, M.; Moan, J.; Peng, Q. Photodynamic Therapy. *J. Natl. Cancer Inst.* **1998**, *90*, 889-905.
3. Dolmans, D. E.; Fukumura, D.; Jain, R. K. Photodynamic Therapy for Cancer. *Nat. Rev. Cancer* **2003**, *3*, 380-387.
4. Sibata, C. H.; Colussi, V. C.; Oleinick, N. L.; Kinsella, T. J. Photodynamic Therapy in Oncology. *Expert Opin. Pharmacother.* **2001**, *2*, 917-927.
5. Allison, R. R.; Downie, G. H.; Cuenca, R.; Hu, X.-H.; Childs, C. J. H.; Sibata, C. H. Photosensitizers in Clinical PDT. *Photodiagn. Photodyn. Ther.* **2004**, *1*, 27-42.
6. Allen, C. M.; Sharman, W. M.; Van Lier, J. E. Current Status of Phthalocyanines in the Photodynamic Therapy of Cancer. *J. Porphyrins Phthalocyanines* **2001**, *5*, 161-169.
7. Zharkova, N. N.; Sokolov, V. V.; Chissov, V. I.; Aristarkhova, E. I.; Kozlov, D. N.; Smirnov, V. V. Fluorescence Examinations of Patients with Tumors of Different Localizations in the Course of Photodynamic Therapy with Photosensitizer Photosens. In *Photochemotherapy: Photodynamic Therapy and Other Modalities*; Benjamin, E., Giulio, J., Johan, M., Eds.; Proc. SPIE, 1995; pp 476-481.
8. Josefsen, L. B.; Boyle, R. W. Photodynamic Therapy: Novel Third-Generation Photosensitizers One Step Closer? *Br. J. Pharmacol.* **2008**, *154*, 1-3.
9. Bechet, D.; Couleaud, P.; Frochet, C.; Viriot, M. L.; Guillemin, F.; Barberi-Heyob, M. Nanoparticles as Vehicles for Delivery of Photodynamic Therapy Agents. *Trends Biotechnol.* **2008**, *26*, 612-621.
10. Wang, S. Z.; Gao, R. M.; Zhou, F. M.; Selke, M. Nanomaterials and Singlet Oxygen Photosensitizers: Potential Applications in Photodynamic Therapy. *J. Mater. Chem.* **2004**, *14*, 487-493.



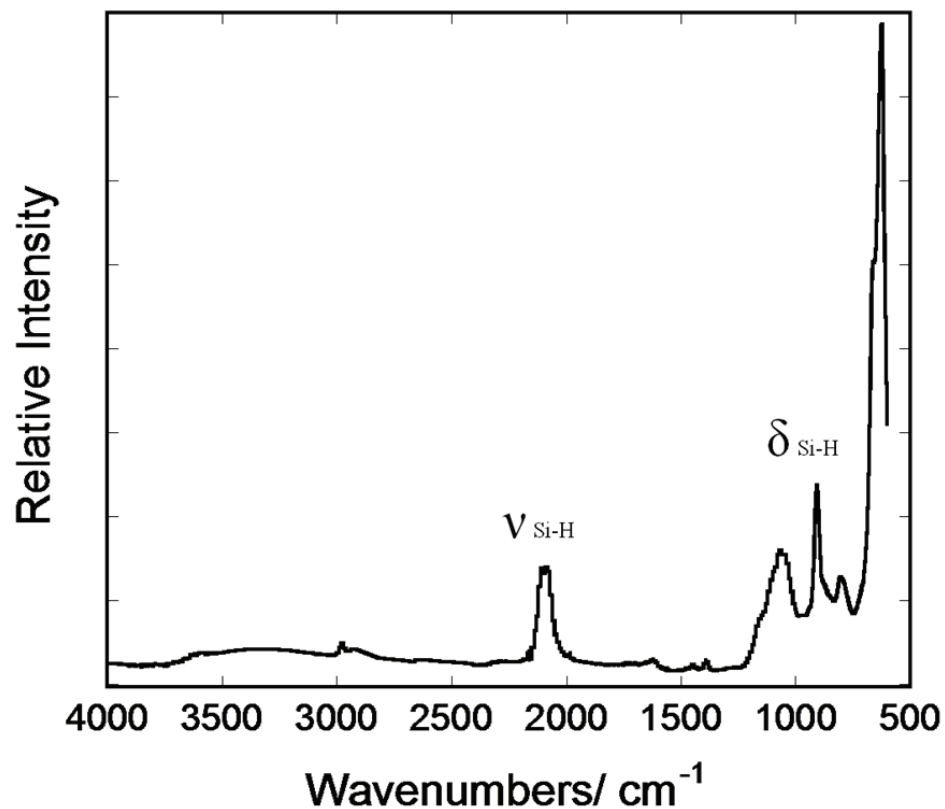
11. Zhao, B. Z.; Yin, J. J.; Bilski, P. J.; Chignell, C. F.; Roberts, J. E.; He, Y. Y. Enhanced Photodynamic Efficacy towards Melanoma Cells by Encapsulation of Pc4 in Silica Nanoparticles. *Toxicol. Appl. Pharmacol.* **2009**, *241*, 163-172.
12. Ohulchanskyy, T. Y.; Roy, I.; Goswami, L. N.; Chen, Y.; Bergey, E. J.; Pandey, R. K.; Oseroff, A. R.; Prasad, P. N. Organically Modified Silica Nanoparticles with Covalently Incorporated Photosensitizer for Photodynamic Therapy of Cancer. *Nano Lett.* **2007**, *7*, 2835-2842.
13. He, X. X.; Wu, X.; Wang, K. M.; Shi, B. H.; Hai, L. Methylene Blue-Encapsulated Phosphonate-Terminated Silica Nanoparticles for Simultaneous *In Vivo* Imaging and Photodynamic Therapy. *Biomaterials* **2009**, *30*, 5601-5609.
14. Tu, H. L.; Lin, Y. S.; Lin, H. Y.; Hung, Y.; Lo, L. W.; Chen, Y. F.; Mou, C. Y. *In Vitro* Studies of Functionalized Mesoporous Silica Nanoparticles for Photodynamic Therapy. *Adv. Mater.* **2009**, *21*, 172-177.
15. Jang, W. D.; Nishiyama, N.; Zhang, G. D.; Harada, A.; Jiang, D. L.; Kawauchi, S.; Morimoto, Y.; Kikuchi, M.; Koyama, H.; Aida, T.; *et al.* Supramolecular Nanocarrier of Anionic Dendrimer Porphyrins with Cationic Block Copolymers Modified with Polyethylene Glycol to Enhance Intracellular Photodynamic Efficacy. *Angew. Chem., Int. Ed.* **2005**, *44*, 419-423.
16. Naito, K.; Tachikawa, T.; Cui, S. C.; Sugimoto, A.; Fujitsuka, M.; Majima, T. Single-Molecule Detection of Airborne Singlet Oxygen. *J. Am. Chem. Soc.* **2006**, *128*, 16430-16431.
17. Daimon, T.; Nosaka, Y. Formation and Behavior of Singlet Molecular Oxygen in TiO<sub>2</sub> Photocatalysis Studied by Detection of Near-Infrared Phosphorescence. *J. Phys. Chem. C* **2007**, *111*, 4420-4424.
18. Juzenas, P.; Chen, W.; Sun, Y. P.; Coelho, M. A.; Generalov, R.; Generalova, N.; Christensen, I. L. Quantum Dots and Nanoparticles for Photodynamic and Radiation Therapies of Cancer. *Adv. Drug Delivery Rev.* **2008**, *60*, 1600-1614.
19. Samia, A. C.; Chen, X.; Burda, C. Semiconductor Quantum Dots for Photodynamic Therapy. *J. Am. Chem. Soc.* **2003**, *125*, 15736-15737.
20. Wang, J. X.; Liu, Y.; Jiao, F.; Lao, F.; Li, W.; Gu, Y. Q.; Li, Y. F.; Ge, C. C.; Zhou, G. Q.; Li, B.; *et al.* Time-Dependent Translocation and Potential Impairment on Central Nervous System by Intranasally Instilled TiO<sub>2</sub> Nanoparticles. *Toxicology* **2008**, *254*, 82-90.
21. Warheit, D. B.; Webb, T. R.; Sayes, C. M.; Colvin, V. L.; Reed, K. L. Pulmonary Instillation Studies with Nanoscale TiO<sub>2</sub> Rods and Dots in Rats: Toxicity Is Not Dependent upon Particle Size and Surface Area. *Toxicol. Sci.* **2006**, *91*, 227-236.

22. Wu, J. H.; Liu, W.; Xue, C. B.; Zhou, S. C.; Lan, F. L.; Bi, L.; Xu, H. B.; Yang, X. L.; Zeng, F. D. Toxicity and Penetration of TiO<sub>2</sub> Nanoparticles in Hairless Mice and Porcine Skin after Subchronic Dermal Exposure. *Toxicol. Lett.* **2009**, *191*, 1-8.
23. Hardman, R. A Toxicologic Review of Quantum Dots: Toxicity Depends on Physicochemical and Environmental Factors. *Environ. Health Perspect.* **2006**, *114*, 165-172.
24. Bakalova, R.; Ohba, H.; Zhelev, Z.; Ishikawa, M.; Baba, Y. Quantum Dots as Photosensitizers? *Nat. Biotechnol.* **2004**, *22*, 1360-1361.
25. Fujii, M.; Minobe, S.; Usui, M.; Hayashi, S.; Gross, E.; Diener, J.; Kovalev, D. Generation of Singlet Oxygen at Room Temperature Mediated by Energy Transfer from Photoexcited Porous Si. *Phys. Rev. B* **2004**, *70*, 085311.
26. Kovalev, D.; Fujii, M. Silicon Nanocrystals: Photosensitizer for Oxygen Molecules. *Adv. Mater.* **2005**, *17*, 2531-2544.
27. Bayliss, S. C.; Buckberry L. D.; Harris, P. J.; Tobin, M. Nature of the Silicon-Animal Cell Interface. *J. Porous Mater.* **2000**, *7*, 191-195.
28. Foraker, A. B.; Walczak, R. J.; Cohen, M. H.; Boiarski, T. A.; Grove, C. F.; Swaan, P. W. Microfabricated Porous Silicon Particles Enhance Paracellular Delivery of Insulin across Intestinal Caco-2 Cell Monolayers. *Pharm. Res.* **2003**, *20*, 110-116.
29. Canham, L. T. Bioactive Silicon Structure Fabrication through Nanoetching Techniques. *Adv. Mater.* **1995**, *7*, 1033-1037.
30. Canham, L. T. Porous Silicon as a Therapeutic Biomaterial. In *Microtechnologies in Medicine and Biology, 1st Annual International Conference*; Lyon, 2000; pp 109-112.
31. Low, S. P.; Voelcker, N. H.; Canham, L. T.; Williams, K. A. The Biocompatibility of Porous Silicon in Tissues of the Eye. *Biomaterials* **2009**, *30*, 2873-2880.
32. Jugdaohsingh, R. Silicon and Bone Health. *J. Nutr., Health Aging* **2007**, *11*, 99-110.
33. Mertz, W. The Essential Trace Elements. *Science* **1981**, *213*, 1332-1338.
34. Yoo, Y.C.; Lee, S. K.; Yang, J. Y.; In, S. W.; Kima, K. W.; Chung, K. H.; Chung, M. G.; Choung, S. Y. Organ Distribution of Heavy Metals in Autopsy Material from Normal Korean. *J. Health Sci.* **2002**, *48*, 186-194.
35. Park, J. H.; Gu, L.; Von Maltzahn, G.; Ruoslahti, E.; Bhatia, S. N.; Sailor, M. J. Biodegradable Luminescent Porous Silicon Nanoparticles for *In Vivo* Applications. *Nat. Mater.* **2009**, *8*, 331-336.

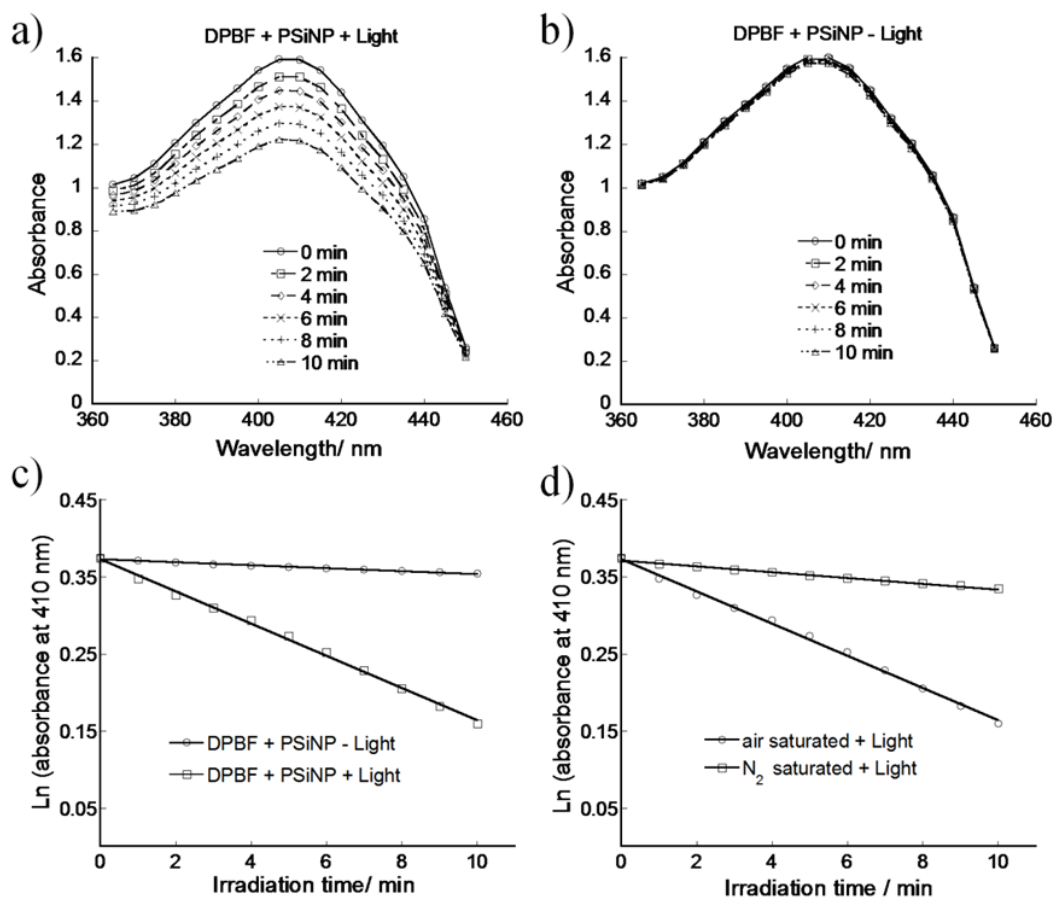
36. Howard, J. A.; Mendenhall, G. D. Autoxidation and Photooxidation of 1,3-Diphenylisobenzofuran: A kinetic and Product Study. *Can. J. Chem.* **1975**, *53*, 2199-2201.
37. Fujii, M.; Usui, M.; Hayashi, S.; Gross, E.; Kovalev, D.; Kunzner, N.; Diener, J.; Timoshenko, V. Y. Chemical Reaction Mediated by Excited States of Si Nanocrystals – Singlet Oxygen Formation in Solution. *J. Appl. Phys.* **2004**, *95*, 3689-3693.
38. Hoebeke, M.; Damoiseau, X. Determination of the Singlet Oxygen Quantum Yield of Bacteriochlorin a: A Comparative Study in Phosphate Buffer and Aqueous Dispersion of Dimiristoyl-L-alpha-Phosphatidylcholine Liposomes. *Photochem. Photobiol. Sci.* **2002**, *1*, 283-287.
39. Venkatesan, R.; Periasamy, N.; Srivastava, T. S. Singlet Molecular-Oxygen Quantum Yield Measurements of Some Porphyrins and Metalloporphyrins. *Proc. Indian Acad. Sci. Chem. Sci.* **1992**, *104*, 713-722.
40. Redmond, R. W.; Gamlin, J. N. A Compilation of Singlet Oxygen Yields from Biologically Relevant Molecules. *Photochem. Photobiol.* **1999**, *70*, 391-475.
41. Timoshenko, V. Light-Induced Generation of Singlet Oxygen in Porous Silicon. In *Sensors for Environment, Health and Security*; Baraton, M.I., Ed.; Springer Netherlands, 2009; pp 125-139.
42. Hurst, J. R.; Schuster, G. B. Nonradiative Relaxation of Singlet Oxygen in Solution. *J. Am. Chem. Soc.* **1983**, *105*, 5756-5760.
43. Ghulinyan, M.; Gelloz, B.; Ohta, T.; Pavesi, L.; Lockwood, D. J.; Koshida, N., Stabilized Porous Silicon Optical Superlattices with Controlled Surface Passivation. *Appl. Phys. Lett.* **2008**, *93*, 061113.
44. Fujii, M.; Nishimura, N.; Fumon, H.; Hayashi, S.; Kovalev, D.; Goller, B.; Diener, J., Dynamics of Photosensitized Formation of Singlet Oxygen by Porous Silicon in Aqueous Solution. *J. Appl. Phys.* **2006**, *100*, 124302.
45. Flors, C.; Fryer, M. J.; Waring, J.; Reeder, B.; Bechtold, U.; Mullineaux, P. M.; Nonell, S.; Wilson, M. T.; Baker, N. R. Imaging the Production of Singlet Oxygen *In Vivo* Using a New Fluorescent Sensor, Singlet Oxygen Sensor Green®. *J. Exp. Bot.* **2006**, *57*, 1725-1734.
46. Ragàs, X.; Jiménez-Banzo, A.; Sánchez-García, D.; Batllori, X.; Nonell, S. Singlet Oxygen Photosensitisation by the Fluorescent Probe Singlet Oxygen Sensor Green®. *Chem. Commun.* **2009**, 2920-2922.
47. Yan, F.; Zhang, Y.; Kim, K. S.; Yuan, H. K.; Vo-Dinh, T. Cellular Uptake and Photodynamic Activity of Protein Nanocages Containing Methylene Blue Photosensitizing Drug. *Photochem. Photobiol.* **2010**, *86*, 662-666.



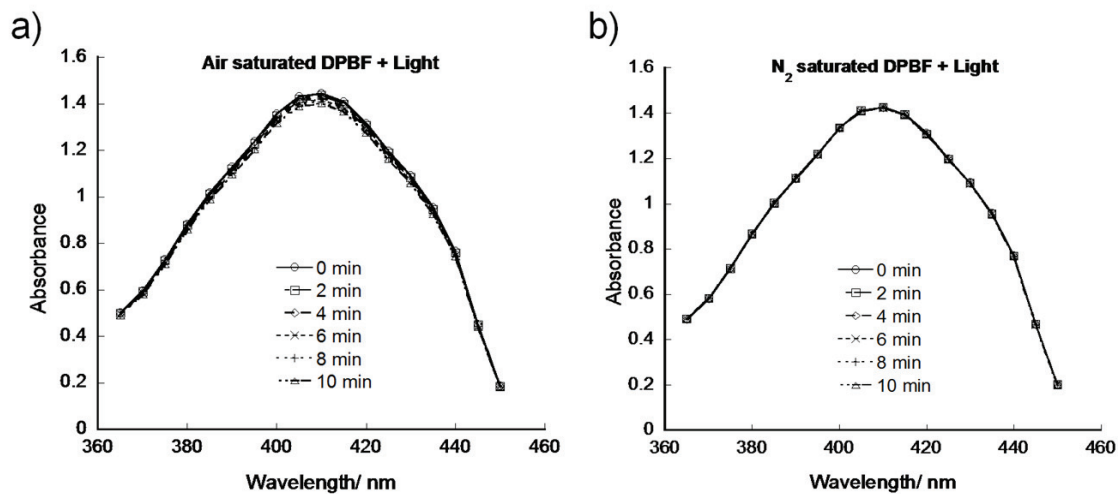
**Figure 5.1 Synthetic procedure followed to prepare porous Si nanoparticles from a single crystal silicon substrate.**



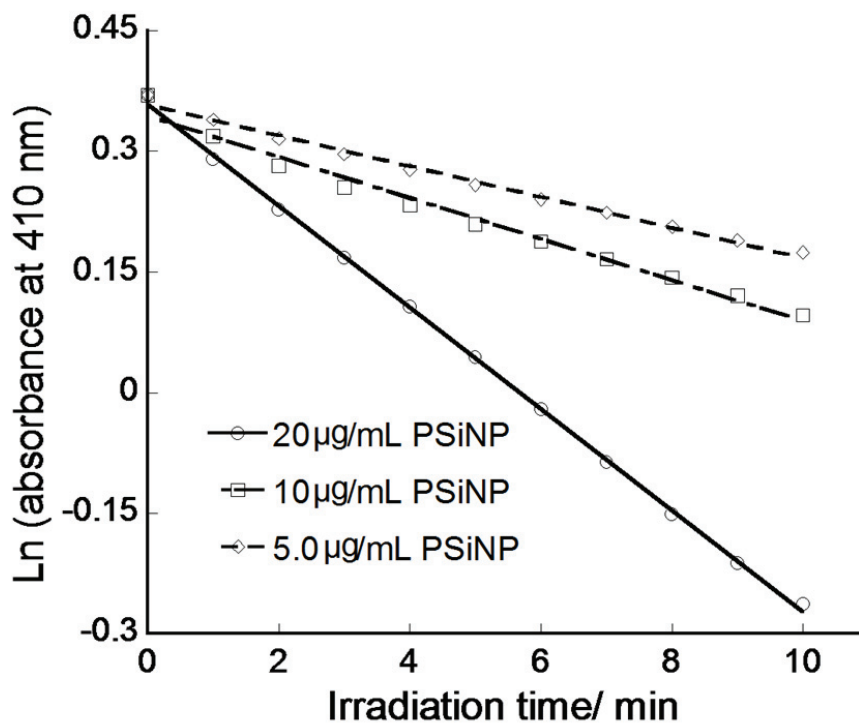
**Figure 5.2** Fourier-transform infrared (FT-IR) spectrum of a typical porous Si nanoparticle preparation. The dry nanoparticle sample was measured using an attenuated total reflectance (diamond ATR) attachment.



**Figure 5.3 Generation of singlet oxygen from porous Si nanoparticles.** Time course of the absorption spectrum of the singlet oxygen indicator DPBF with porous Si nanoparticles (PSiNP) (a) in the presence of and (b) in the absence of light. Solution measurements were obtained in air-saturated ethanol. (c) Decay curves of the (background-corrected) 410-nm absorption bands from (a) and (b). (d) Decay curves of the (background-corrected) 410-nm absorption band from DPBF in irradiated solutions containing PSiNP, in either air-saturated or N<sub>2</sub>-saturated solutions.

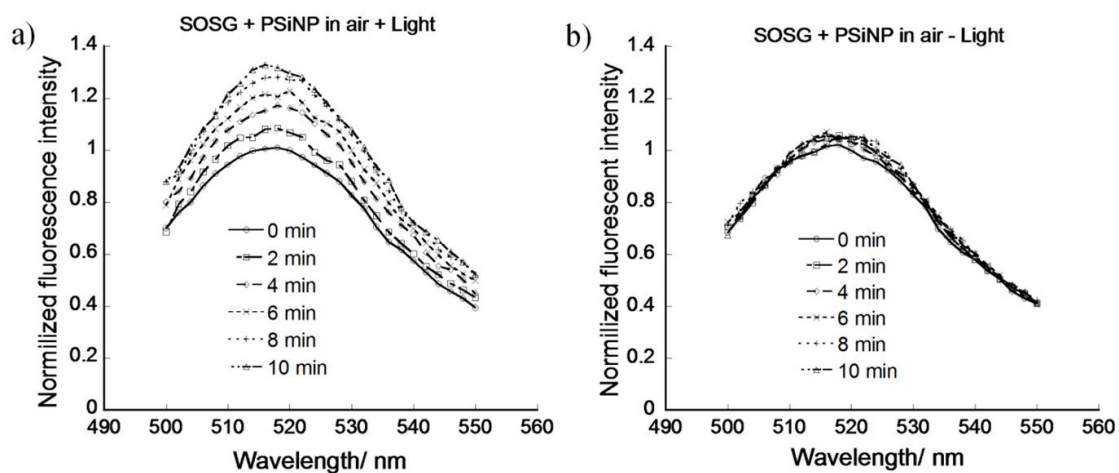


**Figure 5.4** Time course of the absorption spectrum of (a) air-saturated DPBF and (b) N<sub>2</sub>-saturated DPBF (0.08 mM) under irradiation (IR filtered halogen lamp, same conditions as in Fig 5.3). Solution measurements were obtained in ethanol.

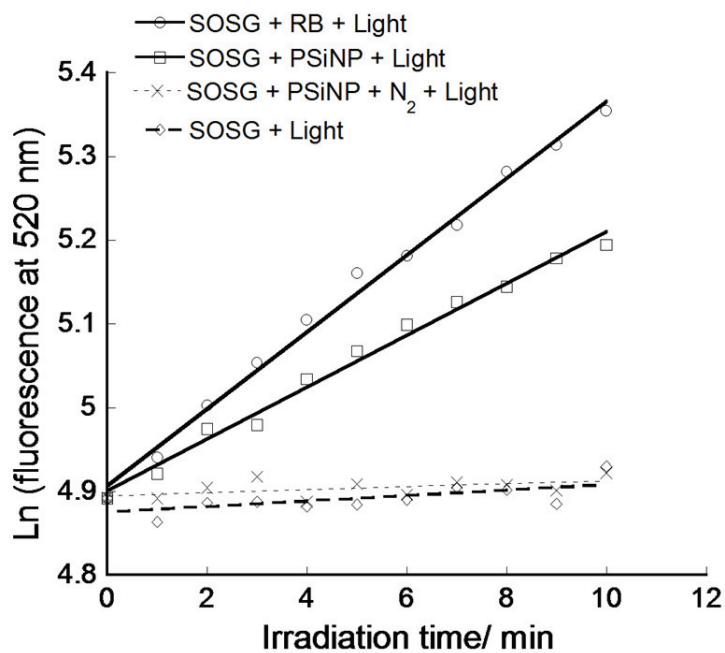


**Figure 5.5** Decay curves of DPBF optical absorption at 410 nm in the presence of 5, 10, and 20 µg/mL of porous Si nanoparticles (background-corrected) as a function of irradiation time.

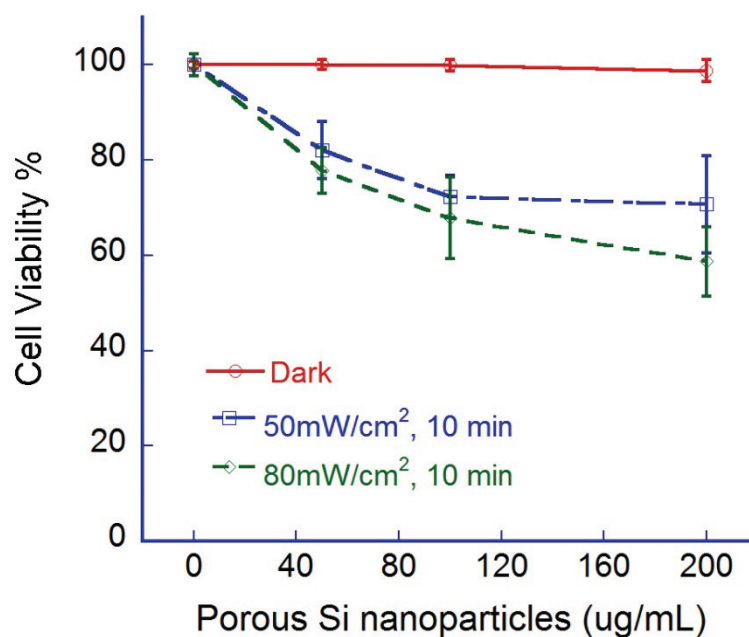




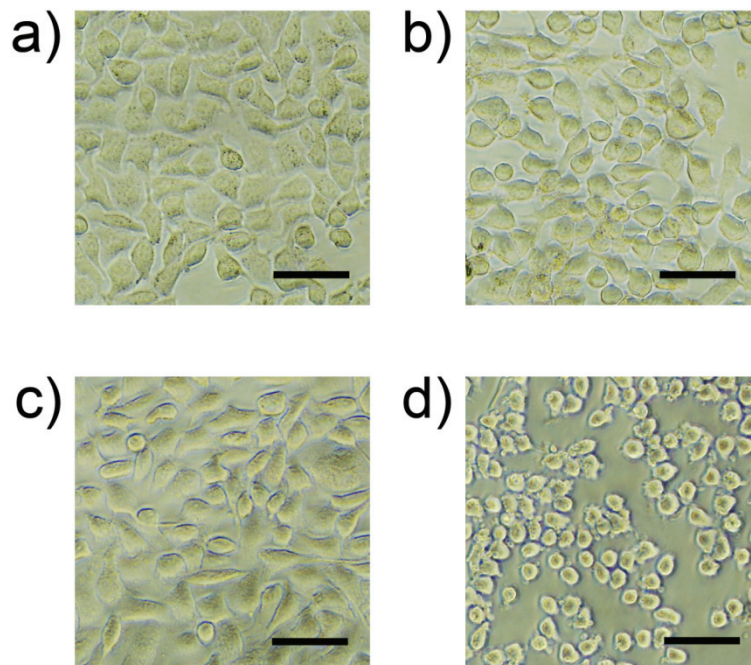
**Figure 5.6** Normalized fluorescence spectra of SOSG incubated (25 °C) with porous Si nanoparticles (PSiNP) (a) in the presence and (b) in the absence of light.



**Figure 5.7 Detection of singlet oxygen generation from porous Si using SOSG.** Increase in fluorescence intensity of SOSG endoperoxide as a function of irradiation time in the presence of SOSG alone, SOSG with RB and SOSG with porous Si nanoparticles (PSiNP) in air and in N<sub>2</sub> saturated solution, respectively.

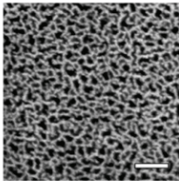
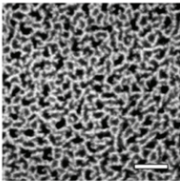
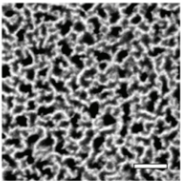
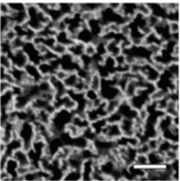
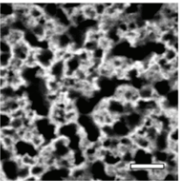
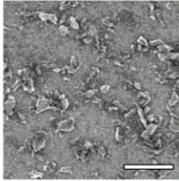
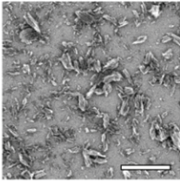
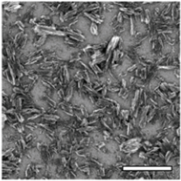
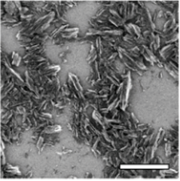
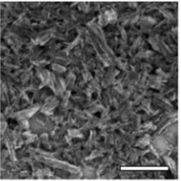


**Figure 5.8 Photoinduced toxicity exhibited by HeLa cells treated with porous Si nanoparticles.** The medium containing the porous Si nanoparticles (PBS buffer) was replaced with cell growth medium (RPMI-1640 medium supplemented with 10% FBS) immediately after irradiation. Cell viability quantified by MTS assay. Illumination was accomplished with a (IR filtered) halogen lamp. Each data point represents the mean of three independent experiments.



**Figure 5.9 Phase contrast microscope images of HeLa cells treated with porous Si nanoparticles (PSiNP) and control experiment.** HeLa cells were treated with (a) PBS in the dark for 10 min (dark control), (b) 100 µg/mL PSiNP in the dark for 10 min, (c) PBS under 60 J/cm<sup>2</sup> light irradiation for 10 min (light control), and (d) 100 µg/mL PSiNP under 60 J/cm<sup>2</sup> light irradiation for 10 min. The scale bars are 50 µm.

**Table 5.1 Characteristics of porous Si nanoparticles (PSiNP) prepared with different etching current densities.**

	50 mA/cm <sup>2</sup>	100 mA/cm <sup>2</sup>	200 mA/cm <sup>2</sup>	300 mA/cm <sup>2</sup>	400 mA/cm <sup>2</sup>
PSiNP size <sub>[a]</sub> (nm)	109.7 ± 11.6	129.6 ± 5.5	146.4 ± 6.6	170.5 ± 4.3	157.8 ± 1.5
Pore size (nm) <sub>[b]</sub>	7.9 ± 2.9	9.2 ± 1.8	11.8 ± 3.8	13.1 ± 5.1	17.9 ± 9.3
Pore <sub>[c]</sub>					
PSiNP <sub>[d]</sub>					
$\Phi_{\text{PSiNP}}$ <sub>[e]</sub>	0.07 ± 0.02	0.12 ± 0.03	0.10 ± 0.02	0.05 ± 0.01	0.05 ± 0.01

[a] PSiNP size (nm) represents the average hydrodynamic size measured by DLS. [b] Pore size (nm) represents the average pore size of the freestanding film measured by SEM. [c] Plan-view images of freestanding porous Si films, showing the pore morphology scale bar is 50 nm. [d] Morphology of porous Si nanoparticles prepared from the films in [c]. Scale bar is 1  $\mu\text{m}$ . [e] <sup>1</sup>O<sub>2</sub> quantum yield of the porous Si nanoparticles.

Chapter five, in part of full, is a reprint (with co-author permission) of the material as it appears in the following publication: Xiao, Ling; **Gu, Luo**; Howell, Stephen B.; Sailor, Michael J., “Porous Silicon Nanoparticle Photosensitizers for Singlet Oxygen and Their Phototoxicity Against Cancer Cells”, *ACS Nano* 2011, 5 (5), 3651-3659. The author of this dissertation is a co-author of this manuscript.

## **CHAPTER VI:**

### **Multivalent Porous Silicon Nanoparticles Enhance the Immune Activation Potency of Agonistic CD40 Antibody**

## 6.1 Abstract

One of the fundamental paradigms in the use of nanoparticles to treat disease is to evade or suppress the immune system in order to minimize systemic side effects and deliver sufficient nanoparticle quantities to the intended tissues. However, the immune system is the body's most important and effective defense against diseases. It protects the host by identifying and eliminating foreign pathogens as well as self-malignancies. Here we report a nanoparticle engineered to work *with* the immune system, enhancing the intended activation of antigen presenting cells (APCs). We show that luminescent porous silicon nanoparticles (LPSiNPs), each containing multiple copies of an agonistic antibody (FGK45) to the APC receptor CD40, greatly enhance activation of B cells. The cellular response to the nanoparticle-based stimulators is equivalent to a 30-40 fold larger concentration of free FGK45. The intrinsic near-infrared photoluminescence of LPSiNPs is used to monitor degradation and track the nanoparticles inside APCs.

## 6.2 Introduction

Nanomaterials of porous silicon have attracted intense interest for imaging and treatment of diseases including cancer due to their biocompatibility, large specific capacity for drug loading, non-toxic degradation products, and efficient photoluminescence<sup>1-9</sup>. One of the main barriers to any nanoparticle intended for *in vivo* use is the surveillance by the immune system<sup>10-12</sup>. For example, the mononuclear phagocyte system (MPS) recognizes and intercepts substantial quantities of systemically administered nanoparticles before they can reach the diseased tissues<sup>11-13</sup>, and this can lead to significant damage to major organs such as liver, spleen, etc., especially when the



nanomaterials carry lethal anticancer drugs. In contrast, approaches to intentionally activate the body's own immune system to fight against diseases can be quite effective<sup>14-20</sup>. The goal of active immunotherapy is to elicit or amplify an immune response to harness the body's inherent defenses against foreign pathogens and self-malignancy. The experimental use of nanomaterials for such active immunotherapies has not been explored to a great extent in part due to the limited understanding of the interactions between the immune system and nanomaterials<sup>21</sup>. Nevertheless, recent studies have shown that some nanoparticle-based vaccines can be much more potent than soluble peptide or protein antigens<sup>22-30</sup>, and it has been proposed that nanovaccines are more adaptable and perhaps safer than viral vaccines<sup>31-33</sup>.

Most studies using nanomaterials in immunotherapies focus on antigen delivery, with little emphasis on the ability of nanomaterials to alter the potency of immunomodulators. In addition, the majority of nanovaccine systems are based on lipids or polymers such as poly(lactic-co-glycolic acid) (PLGA), or polystyrene<sup>23-24, 34-39</sup>, many of which display some intrinsic immune stimulation that may limit their use for immunotherapies (due to unintended stimulation of APCs) or that may interfere with the function of loaded immunomodulators. For many immunotherapeutic or immunomodulation applications, a desirable criterion is that the nanomaterial itself shows low intrinsic immune stimulation.

CD40 is a co-stimulatory receptor as well as a member of the family of tumor necrosis factor (TNF) receptors found on APCs such as dendritic cells, B cells, and macrophages<sup>40-42</sup>. Agonistic monoclonal antibodies to CD40 (CD40 mAb) can activate APCs and improve immune responses when used in combination with antigens or

vaccines<sup>18, 43-44</sup>. In addition, CD40 mAb can produce substantial antitumor efficacy and can also potentially be used to treat chronic autoimmune inflammation<sup>45-48</sup>. However, the therapeutically effective dose of CD40 mAb is high and the high dose can result in severe side effects<sup>47, 49</sup>. We have recently developed nanoparticles based on luminescent porous silicon that display low systemic toxicity and degrade *in vivo* into renally cleared components<sup>1, 50-51</sup>. The porous nanostructure and intrinsic near-infrared photoluminescence of porous silicon nanoparticles (LPSiNPs) enable the incorporation of drug payloads and the monitoring of distribution and degradation *in vivo*<sup>1</sup>. In this study, we show that when multiple copies of the CD40 mAb FGK45 are incorporated onto a LPSiNP, the activation potency on B cells is significantly amplified, equivalent to using ~ 30-40 fold larger concentration of free FGK45. LPSiNPs without FGK45 appear inert to B cells.

### 6.3 Experimental

*Preparation of FGK45 loaded luminescent porous silicon nanoparticles (FGK-LPSiNPs):* LPSiNPs were first prepared using a previously described method<sup>1, 52</sup>. In brief, (100)-oriented p-type single-crystal Si wafers (0.8-1.2 mΩ cm, Siltronix) were electrochemically etched in an electrolyte containing aqueous 48% hydrofluoric acid and ethanol in a 3:1 ratio. The resulting porous Si films were lifted from the Si substrate, fractured by ultrasound and filtered through a 0.22 μm membrane. Finally, the photoluminescence of the nanoparticles were activated by soaking in deionized water for 14 d. To prepare FGK-LPSiNP, an avidin coating was first applied. A 1 mL aliquot of an aqueous dispersion of 0.2 mg of LPSiNP was mixed with a 0.08 mL aliquot of water

containing 0.04 mg of avidin (Thermo Fisher Scientific, Inc.). The mixture was stirred for 1 h at room temperature, rinsed with water three times by centrifugation. The particles were resuspended in water to 0.2 mg/mL and were then mixed with a 0.045 mL aliquot of water containing 0.022 mg of biotin-conjugated FGK45 (Enzo Life Sciences, Inc.; FGK45 is a monoclonal antibody to mouse CD40). The mixture was stirred for 1 h at room temperature, rinsed with water three times by centrifugation to remove any excess FGK45. The supernatant of each wash was combined and the quantity of excess FGK45 in the supernatant was measured by micro BCA (bicinchoninic acid) protein assay (Thermo Fisher Scientific, Inc.) to calculate the quantity of FGK45 loaded on LPSiNP.

*Nanoparticle characterization:* Transmission electron micrographs (TEM) were obtained with a FEI Tecnai G<sup>2</sup> Sphera. Dynamic light scattering (Zetasizer Nano ZS90, Malvern Instruments) was used to determine the hydrodynamic size of the nanoparticles. The photoluminescence (PL,  $\lambda_{\text{ex}} = 370$  nm and 460 nm long pass emission filter) spectra of LPSiNP or FGK-LPSiNP were obtained using a Princeton Instruments/Acton spectrometer fitted with a liquid nitrogen-cooled silicon charge-coupled device (CCD) detector.

*Immunoblot analysis:* FGK-LPSiNPs and FGK45 were diluted in lithium dodecyl sulfate (LDS) sample buffer and reducing agent (Invitrogen), incubated at 80 °C for 10 min, loaded on a 4-12% Bis-Tris gel (Invitrogen) and run under reducing conditions. The gel was then transferred to PVDF membrane and a western blot was performed to detect rat IgG. Briefly, the membrane was blocked in 5% milk in tris-buffered saline Tween 20

(TBST) for 30 min, probed with goat anti-rat IgG (H+L) HRP (Southern Biotech, diluted 1:10,000 in 5% milk in TBST) for 60 min, washed three times with TBST, prepared with ECL Plus substrate (Amersham Biosciences) and signal was detected on a Typhoon 9400 variable mode imager (Amersham Biosciences).

*In vitro degradation of FGK-LPSiNP:* A series of samples containing 0.05 mg/mL of FGK-LPSiNP in 1 mL of PBS solution or pH 4.0 buffer solution were incubated at 37 °C. An aliquot of 0.5 mL of solution was removed at different time points and filtered with a centrifugal filter (30,000 Da molecular weight cut-off, Millipore, inc.) to remove undissolved LPSiNP. 0.4 mL of the filtered solution was diluted with 5 mL HNO<sub>3</sub> (2 % (v/v)) and subjected to analysis by inductively coupled plasma optical emission spectroscopy (ICP-OES, Perkin Elmer Optima 3000DV). The decrease in PL of the above samples over time was also monitored.

*Mice:* C57BL/6 mice were maintained in specific pathogen-free facilities at the University of California, San Diego. Animal protocols were approved by the Institutional Animal Care and Use Committee.

*Cell uptake of FGK-LPSiNP:* Mouse bone marrow-derived dendritic cells (BMDC) were prepared as described<sup>53</sup> and harvested on day 8 for use in microscopy experiments. BMDC (40,000-60,000 cells per well) were seeded into 8-well chamber glass slides (Millipore, inc.) and cultured overnight. The cells were washed with RPMI (Roswell Park Memorial Institute) medium once and incubated with 0.05 mg/mL LPSiNP

or FGK-LPSiNP in RPMI medium for 1.5 hours at 37 °C. For the competitive binding experiment, BMDC were first incubated with 0.03 mg/ml free FGK45 for 30 min in RPMI medium, then incubated with 0.05 mg/mL FGK-LPSiNP as above. The cells were washed 3 times with RPMI medium and incubated with Alexa Fluor 488 conjugated CD11c antibody (clone N418, eBioscience—all antibodies are from eBioscience unless otherwise indicated; 1µg/ml) in RPMI medium for 10 min to visualize the BMDC. The cells were then rinsed three times with PBS, fixed with 4% paraformaldehyde for 20 min and then observed with a Zeiss LSM 510 confocal fluorescence microscope. An excitation wavelength of 405 nm and an emission filter with a bandpass at  $700 \pm 50$  nm were used to image the near-IR photoluminescence of the nanoparticles.

*In vitro stimulation of B cells:* Single-cell suspensions of C57BL/6 splenocytes were prepared and subjected to red blood cell lysis using ACK lysis buffer (0.15 M NH<sub>4</sub>Cl, 1 mM KHCO<sub>3</sub>, 0.1 mM EDTA, pH 7.3). B cells were sorted out via CD43 (Miltenyi) magnetic bead depletion. Sorted cells were plated at  $2 \times 10^5$  cells/well and incubated with LPSiNP, av-LPSiNP, FGK-LPSiNP, free agonistic anti-CD40 (clone FGK45), PBS, or CpG (Pfizer) for 42 h at 37 °C.

*Flow cytometry:* Approximately 1-2 million cells were resuspended in Hank's Balanced Salt Solution (Invitrogen) with 1% fetal calf serum (Omega Scientific) added (HBSS 1% FCS), incubated for 15 min at 4 °C with anti-mouse FcγRII-III (supernatant from hybridoma 2.4G2 cultures), and stained with fluorescently conjugated antibodies for 20 min at 4°C. For particles using avidin-FITC, cells were stained with MHC II biotin

(M5/114.15.2), washed with HBSS 1% FCS, stained with streptavidin PerCP, CD86 Phycoerythrin (GL1; PE) and B220 Allophycocyanin (RA3-6B2) and analyzed by flow cytometry. For particles using non-labeled avidin, cells were stained with B220 FITC, CD86 PE and MHC II Allophycocyanin and analyzed by flow cytometry.

## 6.4 Results and Discussion

LPSiNPs were prepared by electrochemical etch of highly doped p-type single-crystal Si wafers in an electrolyte consisting of aqueous hydrofluoric acid and ethanol, lift-off of the porous layer, ultrasonic fracture, filtration of the resulting nanoparticles through a 0.22  $\mu\text{m}$  filter membrane, and finally activation of luminescence by treatment in an aqueous solution following the published procedure<sup>1, 50-51</sup>. To incorporate FGK45 onto the nanoparticles, we first coated the LPSiNPs with avidin by physisorption (av-LPSiNPs). Biotinylated FGK45 was then conjugated to the nanoparticles through the strong biotin-avidin binding interaction (FGK-LPSiNPs), Fig. 6.1a. Approximately 0.058 mg of FGK45 was loaded per milligram of LPSiNPs, as measured by bicinchoninic acid (BCA) protein assay. The structure of FGK45 loaded on nanoparticle-FGK45 construct was also confirmed by gel electrophoresis and immunoblotting (Fig. 6.2). The FGK-LPSiNPs appeared similar to LPSiNPs in the transmission electron microscope (TEM) images (Fig. 6.1b), but the mean hydrodynamic size measured by dynamic light scattering (DLS) increased from  $\sim 130 \pm 10$  nm to  $\sim 188 \pm 15$  nm after protein attachment (Fig. 6.3).

The intrinsic photoluminescence from the silicon nanostructures in FGK-LPSiNPs under ultraviolet excitation appeared in the near-infrared region of the spectrum ( $\lambda_{\text{max}} =$

790 nm), similar to the non-loaded LPSiNPs. However, the intensity of photoluminescence was somewhat lower from the protein-coated formulation (Fig. 6.1c)<sup>1</sup>. In a physiologically relevant aqueous solution of phosphate buffered saline (PBS) at pH 7.4 and 37 °C, the FGK-LPSiNP construct was observed to degrade within 24 h (Fig. 6.1d). The degradation was tracked by monitoring disappearance of the photoluminescence signal, which decreased gradually upon dissolution of the quantum confined silicon nanostructure<sup>7, 54</sup>, and by appearance of free silicic acid in solution (by inductively coupled plasma-optical emission spectroscopy, ICP-OES), Fig. 6.1d.

The FGK-LPSiNPs were more readily taken up by APCs compared to bare LPSiNPs. When cultured with mouse bone marrow-derived dendritic cells (BMDC), LPSiNPs showed limited (but still detectable) presence in the cells (Fig. 6.4a); in contrast, BMDC incubated with FGK-LPSiNPs under the same conditions showed much higher uptake of nanoparticles (Fig. 6.4b). This uptake was substantially blocked by pre-treatment of the BMDC with free FGK45, indicating that FGK45 binding is responsible for the increased internalization of FGK-LPSiNP (Fig. 6.4c). It has been shown that the CD40 ligand and agonistic antibodies can induce endocytosis of CD40 upon binding<sup>55-56</sup>, which may be responsible for cellular uptake of FGK-LPSiNP in the present case. However, because agonistic CD40 antibodies can also engage FcγRIIB on APCs<sup>57</sup>, interaction of cellular receptors for the Fc domain of the FGK45 antibody could also contribute to the uptake. We tested for inhibition of this interaction by pre-incubation of BMDC with anti-mouse FcγRII-III. The presence of FcγRII-III somewhat reduced, but did not eliminate, cellular uptake of FGK-LPSiNP (Fig. 6.5), which suggests that this is a relevant (but not exclusive) internalization element in the present system.

Subcellular localization of FGK-LPSiNPs was further examined by confocal fluorescence microscopy. By following the near-infrared photoluminescence spectrum of the nanoparticles, we observed FGK-LPSiNPs outside of the lysosomes of the dendritic cells (Fig. 6.4d). The appearance of FGK-LPSiNPs outside of the lysosomes of the dendritic cells (Fig. 6.4d) is consistent with previous reports that various types of silicon or silica based nanomaterials can escape from lysosomes and distribute inside the cytosol<sup>1, 58-60</sup>. In separate experiments aimed at simulating the low pH conditions inside the lysosome, only < 5% dissolution of LPSiNPs was observed in pH 4 buffer solution over a 24h period (Fig. 6.4e and 6.6). Although LPSiNPs are expected to degrade within a few hours at pH 7.4 due to dissolution of the protective oxide coating<sup>1, 61</sup>, they are much more stable in acidic media such as the environment present in the interior of lysosomes. The observed ability of LPSiNPs to escape from lysosomes opens the possibility for delivery of antigens to the cytosol and inducing the MHC class I antigen presentation pathway<sup>18-19</sup>.

We next investigated the activity of FGK-LPSiNPs added to B cells, by measuring the expression of cell surface molecules indicative of B cell activation. The nanoparticles in this experiment contained avidin labeled with fluorescein isothiocyanate (av-FITC). The resulting construct emits both in the green (from the FITC label) and in the near-infrared (from the silicon nanostructure) when excited with ultraviolet light (Fig. 6.7a). B cells enriched from mouse splenocytes were incubated with FGK-LPSiNPs or av-LPSiNPs and then analyzed by flow cytometry. After 42 h of culture, the FITC signal was only detected from B cells that had been exposed to FGK-LPSiNPs (Fig. 6.7b-e). B cells incubated with FGK-LPSiNPs also displayed increased expression of the cell



surface receptors, CD86 and major histocompatibility complex class II (MHC II), the response typical of B cells that have received a signal through CD40 (Fig. 6.7b-e)<sup>45</sup>. Furthermore, the extent of activation induced by FGK-LPSiNPs was concentration dependent (Fig. 6.8). When exposed to a low concentration of FGK-LPSiNPs, not all of the B cells were activated, as indicated by the wide distribution of the fluorescence intensity from the cells in flow cytometry dot plots (Fig 7.7b and 7.7d). However, the population of B cells that displayed high FITC signals also expressed high levels of CD86 and MHC II, indicating that the cells bound with nanoparticles were the ones that were activated (Fig 7.7b and 7.7d). In contrast, B cells cultured with various concentrations of av-LPSiNP all showed low FITC signals and low activation marker levels (Fig. 6.8).

Multivalency is one of the notable advantages of using nanomaterials for biomedical applications. For example, studies using nanoparticles as cancer diagnostic and therapeutic agents have shown that when multiple copies of tumor targeting ligand are displayed on an individual nanoparticle, its tumor targeting efficiency can be significantly enhanced<sup>62-65</sup>. This enhancement is generally ascribed to the multivalent effect which is also observed in many natural processes such as antibody interactions and clotting<sup>11</sup>. To determine if multivalency plays a strong role in the activation potency of the agonistic antibody to APCs, we cultured B cells with either FGK-LPSiNPs or an equivalent concentration of free FGK45 and analyzed the cells by flow cytometry. Both FGK-LPSiNPs and free FGK45 activated B cells, and the activation level of the cells correlated with the concentration of FGK45 (Fig. 6.9a). However, at a given total concentration of FGK45 antibody, FGK-LPSiNPs showed substantially higher activation

potency than free FGK45. Activated B cells upregulated CD86 and MHC II to a detectable level when cultured with FGK-LPSiNPs containing as little as  $\sim 3.6 - 7.2$  ng/mL of FGK45; whereas a similar level of B cell activation was only observed when the concentration of free FGK45 was  $\geq 140 - 200$  ng/mL (Fig. 6.9a). Comparison of the titration curves of FGK-LPSiNPs and free FGK45 revealed that the B cell activation potency of FGK45 in the FGK-LPSiNP constructs is equivalent to using  $\sim 30-40$  fold larger concentration of free FGK45 (Fig. 6.9a).

To test if the enhancement of APC activation is caused by the uncoated porous silicon nanomaterial itself, we cultured B cells with various concentrations of LPSiNPs as control experiments. No induction of CD86 or MHC II was observed at LPSiNP concentrations up to 5000 ng/mL, equivalent to the highest concentration of FGK-LPSiNPs used in the stimulation study (Fig. 6.9b and Fig. 6.10). This suggests that the amplification induced by the FGK-LPSiNP construct results from enhancement of the agonistic antibody's intrinsic function rather than an immune response to the nanomaterial itself. The very low stimulation of APCs by LPSiNPs that do not contain FGK45 is attributed to their primarily inorganic chemical composition; the chemical structure of the silicon-based nanoparticles (and their biodegradation products) possess little similarity to natural pathogens or other "danger signals" normally presented to the immune system<sup>8, 21, 66</sup>.

## 6.5 Conclusions

The present study represents the first example of amplification of the potency of an agonistic anti-CD40 antibody to stimulate APCs using nanomaterials. Agonistic CD40

mAb has attracted considerable interest as it has recently entered clinical trials as a therapeutic for solid tumors<sup>46</sup>. The amplification effect seen in the present study suggests that a nanoparticle-based CD40 antibody therapeutic may amplify the potency and decrease the dose required in the clinical application of CD40 mAb. In addition to the enhancement effect, the inert inorganic composition and biodegradable property of LPSiNPs could overcome some of the disadvantages of lipid or polymer-based materials for immunotherapy applications. Their intrinsic photoluminescence also provides a means to monitor the degradation of LPSiNPs and track their interaction with the immune system.

## 6.6 References

1. Park, J.-H. et al. Biodegradable luminescent porous silicon nanoparticles for in vivo applications. *Nature Mater.* **8**, 331-336 (2009).
2. Tasciotti, E. et al. Mesoporous silicon particles as a multistage delivery system for imaging and therapeutic applications. *Nat. Nanotechnol.* **3**, 151-157 (2008).
3. Salonen, J. et al. Mesoporous silicon microparticles for oral drug delivery: Loading and release of five model drugs. *J. Control. Release* **108**, 362-374 (2005).
4. Low, S.P., Voelcker, N.H., Canham, L.T. & Willams, K.A. The biocompatibility of porous silicon in tissues of the eye. *Biomaterials* **30**, 2873-2880 (2009).
5. Xiao, L., Gu, L., Howell, S.B. & Sailor, M.J. Porous Silicon Nanoparticle Photosensitizers for Singlet Oxygen and Their Phototoxicity against Cancer Cells. *ACS Nano* **5**, 3651-3659 (2011).
6. Wolkin, M.V., Jorne, J., Fauchet, P.M., Allan, G. & Delerue, C. Electronic states and luminescence in porous silicon quantum dots: The role of oxygen. *Phys. Rev. Lett.* **82**, 197-200 (1999).
7. Canham, L.T. Silicon Quantum Wire Array Fabrication by Electrochemical and Chemical Dissolution. *Appl. Phys. Lett.* **57**, 1046-1048 (1990).

8. Anderson, S.H.C., Elliott, H., Wallis, D.J., Canham, L.T. & Powell, J.J. Dissolution of different forms of partially porous silicon wafers under simulated physiological conditions. *Phys. Status Solidi A-Appl. Res.* **197**, 331-335 (2003).
9. Erogbogbo, F. et al. Biocompatible luminescent silicon quantum dots for imaging of cancer cells. *Acs Nano* **2**, 873-878 (2008).
10. Peer, D. et al. Nanocarriers as an emerging platform for cancer therapy. *Nature Nanotech.* **2**, 751-760 (2007).
11. Ruoslahti, E., Bhatia, S.N. & Sailor, M.J. Targeting of drugs and nanoparticles to tumors. *J. Cell Biol.* **188**, 759-768 (2010).
12. Moghimi, S.M., Hunter, A.C. & Murray, J.C. Long-circulating and target-specific nanoparticles: Theory to practice. *Pharmacological Reviews* **53**, 283-318 (2001).
13. Brigger, I., Dubernet, C. & Couvreur, P. Nanoparticles in cancer therapy and diagnosis. *Adv. Drug Deliv. Rev.* **54**, 631-651 (2002).
14. Kantoff, P.W. et al. Sipuleucel-T Immunotherapy for Castration-Resistant Prostate Cancer. *New England Journal of Medicine* **363**, 411-422 (2010).
15. Hodi, F.S. et al. Improved Survival with Ipilimumab in Patients with Metastatic Melanoma. *New England Journal of Medicine* **363**, 711-723 (2010).
16. Porter, D.L., Levine, B.L., Kalos, M., Bagg, A. & June, C.H. Chimeric Antigen Receptor-Modified T Cells in Chronic Lymphoid Leukemia. *New England Journal of Medicine* **365**, 725-733 (2011).
17. Hunder, N.N. et al. Treatment of metastatic melanoma with autologous CD4+T cells against NY-ESO-1. *New England Journal of Medicine* **358**, 2698-2703 (2008).
18. Pardoll, D.M. Spinning molecular immunology into successful immunotherapy. *Nature Rev. Immunol.* **2**, 227-238 (2002).
19. Waldmann, T.A. Immunotherapy: past, present and future. *Nature Med.* **9**, 269-277 (2003).
20. Rosenberg, S.A., Yang, J.C. & Restifo, N.P. Cancer immunotherapy: moving beyond current vaccines. *Nature Med.* **10**, 909-915 (2004).
21. Dobrovolskaia, M.A. & McNeil, S.E. Immunological properties of engineered nanomaterials. *Nature Nanotech.* **2**, 469-478 (2007).
22. Shen, H. et al. Enhanced and prolonged cross-presentation following endosomal escape of exogenous antigens encapsulated in biodegradable nanoparticles. *Immunology* **117**, 78-88 (2006).

23. Slutter, B. et al. Conjugation of ovalbumin to trimethyl chitosan improves immunogenicity of the antigen. *J. Control Release* **143**, 207-214 (2010).
24. Uto, T. et al. Targeting of antigen to dendritic cells with poly( $\gamma$ -glutamic acid) nanoparticles induces antigen-specific humoral and cellular immunity. *J. Immunol.* **178**, 2979-2986 (2007).
25. Copland, M.J., Rades, T., Davies, N.M. & Baird, M.A. Lipid based particulate formulations for the delivery of antigen. *Immunol. Cell Biol.* **83**, 97-105 (2005).
26. Elamanchili, P., Diwan, M., Cao, M. & Samuel, J. Characterization of poly(D,L-lactic-co-glycolic acid) based nanoparticulate system for enhanced delivery of antigens to dendritic cells. *Vaccine* **22**, 2406-2412 (2004).
27. Cho, N.-H. et al. A multifunctional core-shell nanoparticle for dendritic cell-based cancer immunotherapy. *Nature Nanotech.* **6**, 675-682 (2011).
28. Li, H., Li, Y., Jiao, J. & Hu, H.-M. Alpha-alumina nanoparticles induce efficient autophagy-dependent cross-presentation and potent antitumour response. *Nature Nanotech.* **6**, 645-650 (2011).
29. Makidon, P.E. et al. Pre-Clinical Evaluation of a Novel Nanoemulsion-Based Hepatitis B Mucosal Vaccine. *PLoS One* **3** (2008).
30. Makidon, P.E. et al. Induction of immune response to the 17 kDa OMPA *Burkholderia cenocepacia* polypeptide and protection against pulmonary infection in mice after nasal vaccination with an OMP nanoemulsion-based vaccine. *Med. Microbiol. Immunol.* **199**, 81-92 (2010).
31. Peek, L.J., Middaugh, C.R. & Berkland, C. Nanotechnology in vaccine delivery. *Adv. Drug Deliv. Rev.* **60**, 915-928 (2008).
32. Demento, S.L. et al. Inflammasome-activating nanoparticles as modular systems for optimizing vaccine efficacy. *Vaccine* **27**, 3013-3021 (2009).
33. Moon, J.J. et al. Interbilayer-crosslinked multilamellar vesicles as synthetic vaccines for potent humoral and cellular immune responses. *Nature Mater.* **10**, 243-251 (2011).
34. Diwan, M., Elamanchili, P., Lane, H., Gainer, A. & Samuel, J. Biodegradable nanoparticle mediated antigen delivery to human cord blood derived dendritic cells for induction of primary T cell responses. *J. Drug Targeting* **11**, 495-507 (2003).
35. Petersen, L.K., Xue, L., Wannemuehler, M.J., Rajan, K. & Narasimhan, B. The simultaneous effect of polymer chemistry and device geometry on the in vitro activation of murine dendritic cells. *Biomaterials* **30**, 5131-5142 (2009).

36. Li, A. et al. Signalling pathways involved in the activation of dendritic cells by layered double hydroxide nanoparticles. *Biomaterials* **31**, 748-756 (2010).
37. Reddy, S.T. et al. Exploiting lymphatic transport and complement activation in nanoparticle vaccines. *Nature Biotech.* **25**, 1159-1164 (2007).
38. Klippstein, R. & Pozo, D. Nanotechnology-based manipulation of dendritic cells for enhanced immunotherapy strategies. *Nanomed.-Nanotechnol. Biol. Med.* **6**, 523-529 (2010).
39. Cui, Z., Han, S.-J., Vangasseri, D.P. & Huang, L. Immunostimulation mechanism of LPD nanoparticle as a vaccine carrier. *Molecular Pharmaceutics* **2**, 22-28 (2005).
40. Banchereau, J. et al. The CD40 Antigen and its Ligand. *Annu. Rev. Immunol.* **12**, 881-922 (1994).
41. Schoenberger, S.P., Toes, R.E.M., van der Voort, E.I.H., Offringa, R. & Melief, C.J.M. T-cell help for cytotoxic T lymphocytes is mediated by CD40-CD40L interactions. *Nature* **393**, 480-483 (1998).
42. Bennett, S.R.M. et al. Help for cytotoxic-T-cell responses is mediated by CD40 signalling. *Nature* **393**, 478-480 (1998).
43. Dougan, M. & Dranoff, G. in *Annual Review of Immunology*, Vol. 27 83-117(2009).
44. Palucka, K., Banchereau, J. & Mellman, I. Designing Vaccines Based on Biology of Human Dendritic Cell Subsets. *Immunity* **33**, 464-478 (2010).
45. Beatty, G.L. et al. CD40 Agonists Alter Tumor Stroma and Show Efficacy Against Pancreatic Carcinoma in Mice and Humans. *Science* **331**, 1612-1616 (2011).
46. Vonderheide, R.H. et al. Clinical activity and immune modulation in cancer patients treated with CP-870,893, a novel CD40 agonist monoclonal antibody. *J. Clin. Oncol.* **25**, 876-883 (2007).
47. Jackaman, C., Cornwall, S., Graham, P.T. & Nelson, D.J. CD40-activated B cells contribute to mesothelioma tumor regression. *Immunol. Cell Biol.* **89**, 255-267 (2011).
48. Mauri, C., Mars, L.T. & Londei, M. Therapeutic activity of agonistic monoclonal antibodies against CD40 in a chronic autoimmune inflammatory process. *Nature Med.* **6**, 673-679 (2000).
49. Barr, T.A., McCormick, A.L., Carling, J. & Heath, A.W. A potent adjuvant effect of CD40 antibody attached to antigen. *Immunology* **109**, 87-92 (2003).
50. Heinrich, J.L., Curtis, C.L., Credo, G.M., Kavanagh, K.L. & Sailor, M.J. Luminescent colloidal Si suspensions from porous Si. *Science* **255**, 66-68 (1992).

51. Gu, L., Park, J.-H., Duong, K.H., Ruoslahti, E. & Sailor, M.J. Magnetic Luminescent Porous Silicon Microparticles for Localized Delivery of Molecular Drug Payloads. *Small* **6**, 2546-2552 (2010).
52. Sailor, M.J. *Porous Silicon in Practice: Preparation, Characterization, and Applications*. (Wiley-VCH, Weinheim, Germany; 2012).
53. Dejean, A.S. et al. Transcription factor Foxo3 controls the magnitude of T cell immune responses by modulating the function of dendritic cells. *Nature Immunol.* **10**, 504-513 (2009).
54. Lehmann, V. & Gosele, U. Porous Silicon Formation: a Quantum Wire Effect. *Appl. Phys. Lett.* **58**, 856-858 (1991).
55. Chen, J., Chen, L., Wang, G. & Tang, H. Cholesterol-dependent and - Independent CD40 internalization and signaling activation in cardiovascular endothelial cells. *Arterioscler. Thromb. Vasc. Biol.* **27**, 2005-2013 (2007).
56. Chen, Y. et al. Internalization of CD40 regulates its signal transduction in vascular endothelial cells. *Biochemical and Biophysical Research Communications* **345**, 106-117 (2006).
57. Li, F. & Ravetch, J.V. Inhibitory Fc gamma Receptor Engagement Drives Adjuvant and Anti-Tumor Activities of Agonistic CD40 Antibodies. *Science* **333**, 1030-1034 (2011).
58. Slowing, I., Trewyn, B.G. & Lin, V.S.Y. Effect of surface functionalization of MCM-41-type mesoporous silica nanoparticles on the endocytosis by human cancer cells. *J. Am. Chem. Soc.* **128**, 14792-14793 (2006).
59. Serda, R.E. et al. The association of silicon microparticles with endothelial cells in drug delivery to the vasculature. *Biomaterials* **30**, 2440-2448 (2009).
60. Ashley, C.E. et al. The targeted delivery of multicomponent cargos to cancer cells by nanoporous particle-supported lipid bilayers. *Nature Mater.* **10**, 389-397 (2011).
61. Wu, E.C. et al. Oxidation-Triggered Release of Fluorescent Molecules or Drugs from Mesoporous Si Microparticles. *ACS Nano* **2**, 2401-2409 (2008).
62. Hong, S. et al. The binding avidity of a nanoparticle-based multivalent targeted drug delivery platform. *Chem Biol* **14** (2007).
63. Park, J.-H. et al. Systematic Surface Engineering of Magnetic Nanoworms for in vivo Tumor Targeting. *Small* **5**, 694-700 (2009).
64. Liu, Z. et al. In vivo biodistribution and highly efficient tumour targeting of carbon nanotubes in mice. *Nat. Nanotech.* **2**, 47-52 (2007).

65. Montet, X., Funovics, M., Montet-Abou, K., Weissleder, R. & Josephson, L. Multivalent effects of RGD peptides obtained by nanoparticle display. *J. Med. Chem.* **49**, 6087-6093 (2006).
66. Van Dyck, K., Robberecht, H., Van Cauwenbergh, R., Van Vlaslaer, V. & Deelstra, H. Indication of silicon essentiality in humans - Serum concentrations in Belgian children and adults, including pregnant women. *Biol. Trace Elem. Res.* **77**, 25-32 (2000).



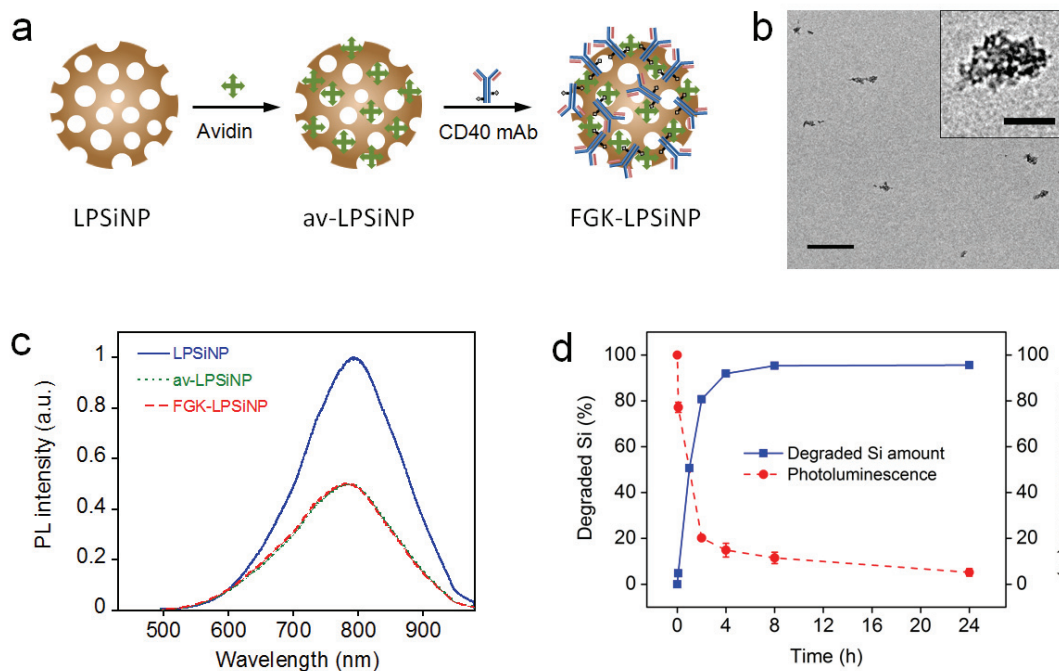


**Figure 6.1 Preparation and characterization of FGK45 loaded luminescent porous silicon nanoparticles (FGK-LPSiNP).** **a**, Schematic representation of the preparation of FGK-LPSiNP. LPSiNP was first coated with avidin by physisorption (av-LPSiNP). Biotinylated FGK45 was then conjugated to the nanoparticles through biotin-avidin binding to form FGK-LPSiNP. **b**, Transmission electron microscope image of FGK-LPSiNP (inset shows the porous nanostructure of one of the nanoparticles). Scale bar is 1  $\mu\text{m}$  (100 nm for the inset). **c**, Photoluminescence (PL) spectra of LPSiNP, av-LPSiNP and FGK-LPSiNP. PL was measured using UV excitation ( $\lambda_{\text{ex}} = 370 \text{ nm}$ ). **d**, Appearance of dissolved silicon in solution (by ICP-OES) and decrease in photoluminescence intensity from a sample of FGK-LPSiNP (50  $\mu\text{g/mL}$ ) incubated in PBS solution at 37°C as a function of time.

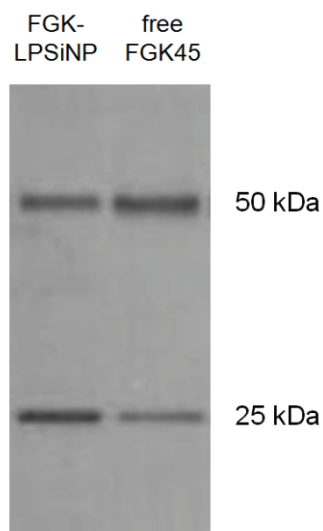


**Figure 6.2 Immunoblot analysis of FGK45 loaded on luminescent porous silicon nanoparticles (LPSiNPs).** A western blot used to detect rat IgG (H+L) in FGK-LPSiNPs and free FGK45 is shown. The gel was run under reducing conditions, yielding both heavy (50kDa) and light (25kDa) chain antibody bands of FGK45. Antibody that had been loaded on LPSiNPs appears similar to free FGK45.

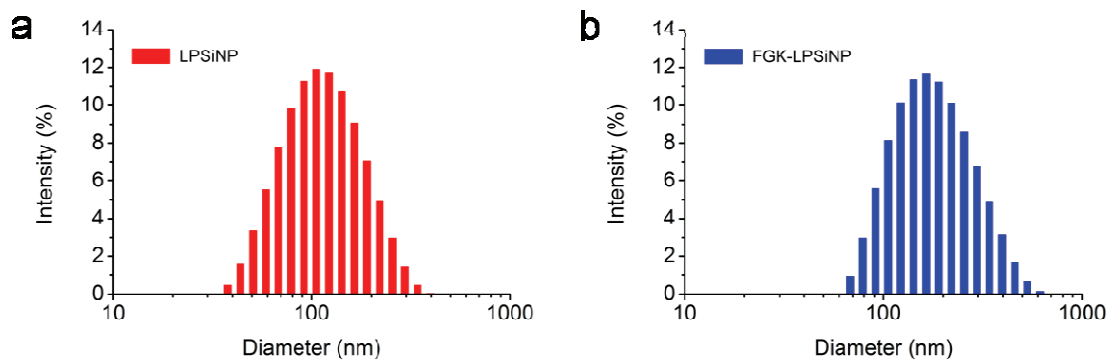


**Figure 6.3 Representative hydrodynamic size data.** Hydrodynamic size distribution of (a) LPSiNPs and (b) FGK-LPSiNPs obtained by dynamic light scattering. Note that the mean size increases from ~130 nm to ~188 nm due to the attached protein molecules.

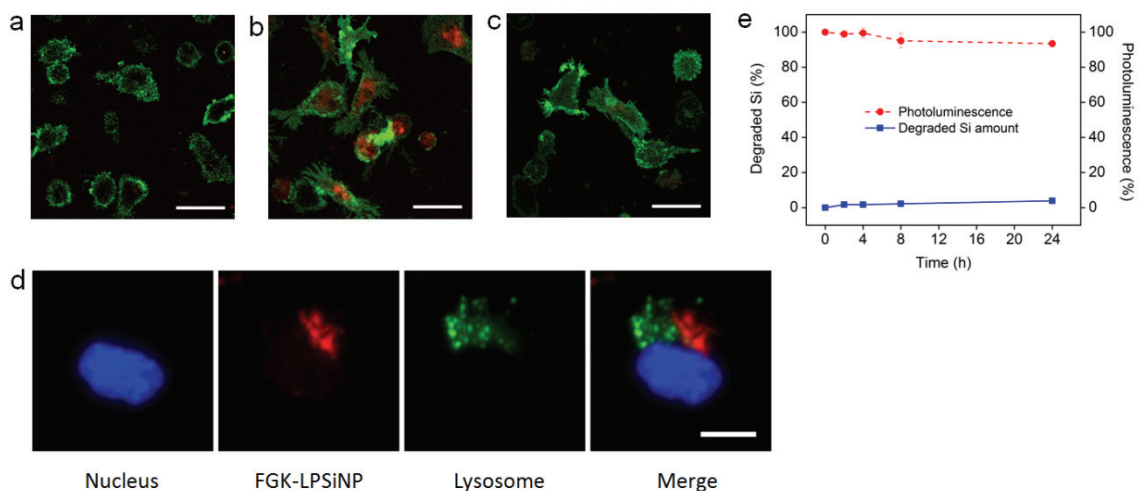


**Figure 6.4 Dendritic cell uptake of FGK-LPSiNPs.** Fluorescence microscope images of mouse bone marrow-derived dendritic cells (BMDC) incubated with **a**, LPSiNPs or **b**, FGK-LPSiNPs for 1.5 h at 37 °C. **c**, free FGK45 inhibits uptake of FGK-LPSiNPs. BMDC were blocked with free FGK45 for 30 min and then incubated with FGK-LPSiNPs for 1.5 h at 37 °C. BMDC were detected by staining with Alexa Fluor 488 conjugated CD11c antibody (green). FGK-LPSiNPs were detected by their intrinsic visible/near-infrared photoluminescence (red,  $\lambda_{\text{ex}} = 405 \text{ nm}$  and  $\lambda_{\text{em}} = 700 \pm 50 \text{ nm}$ ). The scale bars are 40  $\mu\text{m}$ . **d**, FGK-LPSiNPs distribution in BMDC. BMDC were incubated with FGK-LPSiNP for 1.5 h at 37 °C. The lysosomes (green) of the cells were stained with LysoTracker (Invitrogen). Blue and red indicate the cell nucleus and FGK-LPSiNPs, respectively. The scale bar is 10  $\mu\text{m}$ . **e**, Degradation of LPSiNPs (50  $\mu\text{g/mL}$ ) in pH 4 buffer solution at 37 °C as a function of time.

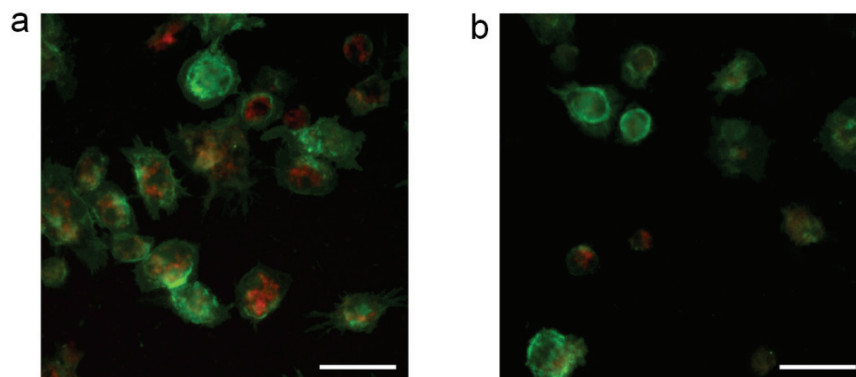


**Figure 6.5 Dendritic cell uptake of FGK-LPSiNPs.** Fluorescence microscope images of mouse bone marrow-derived dendritic cells (BMDC) incubated with FGK-LPSiNPs for 1.5 h at 37 °C. **a**, BMDC were incubated with FGK-LPSiNPs directly. **b**, BMDC were blocked with anti-mouse FcγRII-III for 30 min prior to incubation with FGK-LPSiNPs. BMDC were detected by staining with Alexa Fluor 488 conjugated CD11c antibody (green). FGK-LPSiNPs were detected by their intrinsic visible/near-infrared photoluminescence (red,  $\lambda_{\text{ex}} = 370$  nm and  $\lambda_{\text{em}} = 720 \pm 80$  nm). The scale bars are 40  $\mu\text{m}$ .

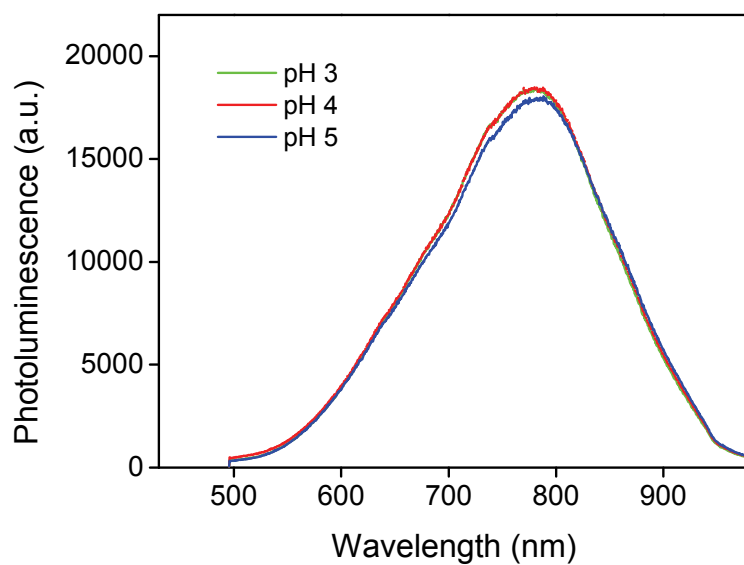


**Figure 6.6 Photoluminescence spectra of LPSiNPs in acidic buffer solutions at room temperature.** The nanoparticles are stable for 24 h in all three acidic pH values indicated (excitation wavelength 370 nm, emission filter 460 nm longpass).

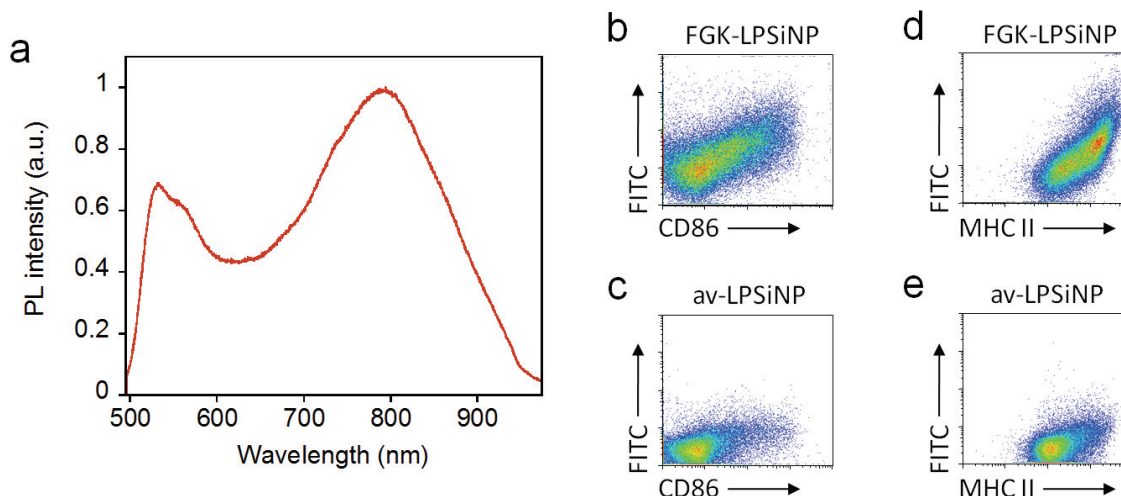


**Figure 6.7 Interaction of FGK-LPSiNPs with B cells.** **a**, Photoluminescence spectrum of LPSiNPs coated with FITC-labeled avidin, showing the emission bands from both the FITC label ( $\lambda_{\max} \sim 520$  nm) and porous silicon ( $\lambda_{\max} \sim 790$  nm). **b-e**, Flow cytometry data quantifying the level of expression of the B cell activation markers CD86 (**b**, **c**) and MHC II (**d**, **e**) after incubation with 5  $\mu\text{g}/\text{mL}$  of FGK-LPSiNPs (**b**, **d**) or av-LPSiNPs (**c**, **e**) for 42 h. The nanoparticles used in this experiment were coated with FITC-labeled avidin. The FITC signal from the cells is plotted against the expression level of CD86 (**b**, **c**) or MHC II (**d**, **e**) after stimulation. FGK-LPSiNPs used here contain 36  $\mu\text{g}$  of FGK45 per milligram of nanoparticles. Note the quantity of FGK45 loaded is smaller when LPSiNPs are coated with FITC conjugated avidin compared with non-labeled native avidin.

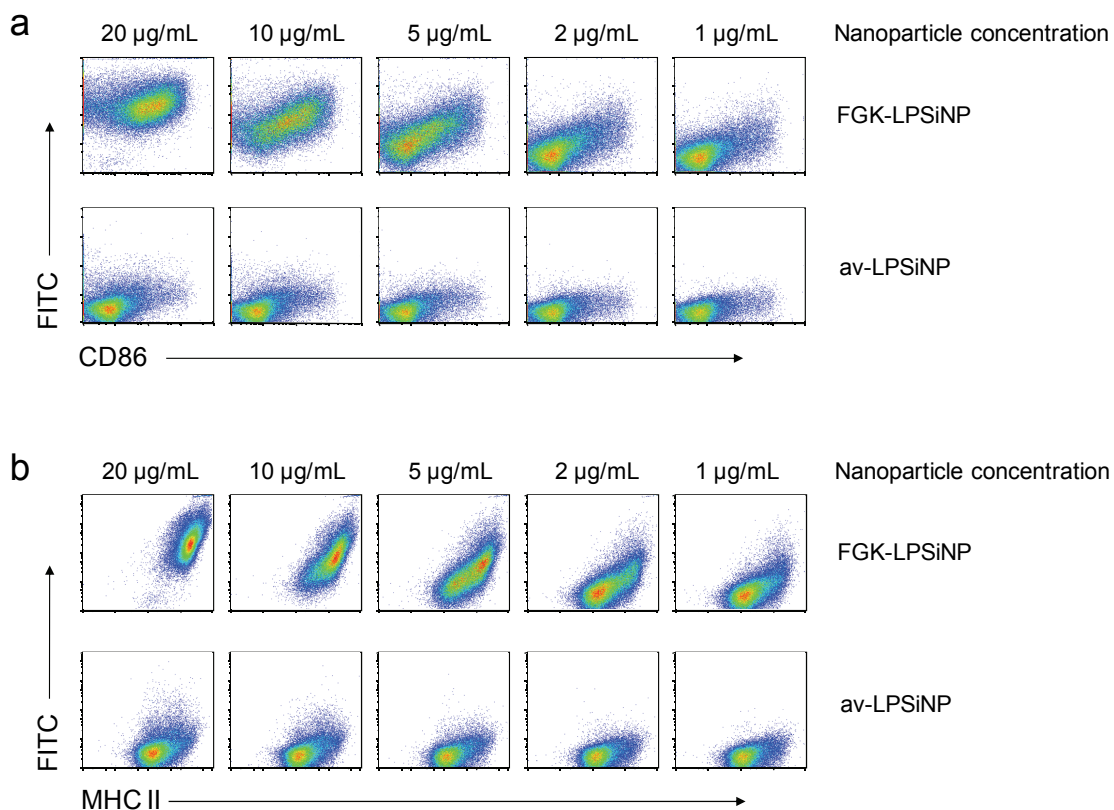


**Figure 6.8 Stimulation of B cells using various concentrations of FGK45 loaded LPSiNPs (FGK-LPSiNPs, top row in (a) and (b)) or avidin coated LPSiNPs (av-LPSiNPs, bottom row in (a) and (b)).** FGK-LPSiNPs used in this study contain 0.036 mg of FGK45 in 1 mg of nanoparticles. Avidin was conjugated with FITC before coating on the nanoparticles. After 42 h of culture, the FITC signal is only detected from B cells that had been stimulated with FGK-LPSiNPs. The B cells stimulated with FGK-LPSiNPs upregulated the activation markers CD86 (**a**) and MHC II (**b**), and the cells with high FITC signal also expressed high levels of CD86 (**a**) and MHC II (**b**), which indicates the cells that bound FGK-LPSiNPs were also the ones that upregulated the activation markers.



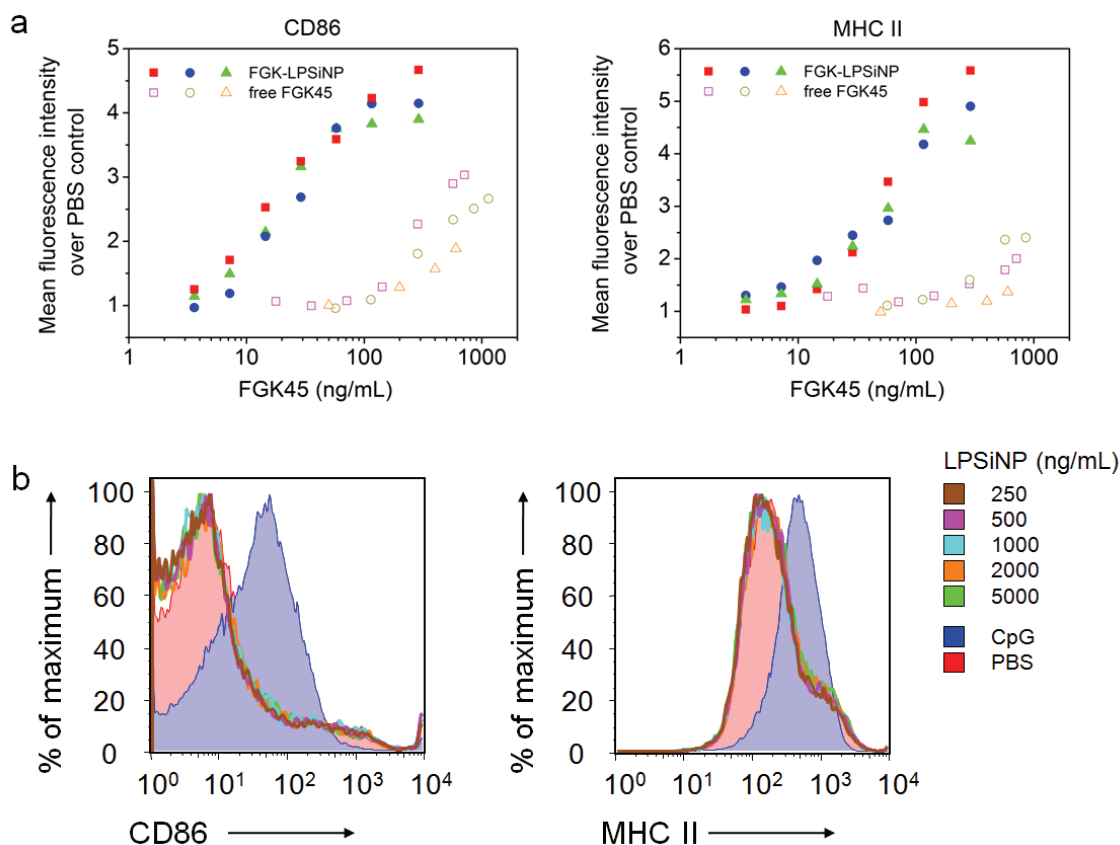


**Figure 6.9 Amplified activation potency of FGK-LPSiNPs compared to free FGK45.**  
**a**, Flow cytometry analysis of the expression of B cell activation markers CD86 and MHC II, represented as the relative mean fluorescence intensity of the marker staining, after incubation with either FGK-LPSiNPs or free FGK45 for 42 h at 37 °C. The concentration of FGK45 on the FGK-LPSiNP constructs is reported based on the total loading of FGK45 on the nanoparticles (58  $\mu$ g of FGK45 per mg of nanoparticles). Data are from independent experiments. **b**, Flow cytometry histograms of B cell activation markers CD86 and MHC II after incubation with various concentrations of LPSiNPs for 42 h at 37 °C. PBS (red shaded) and CpG (blue shaded) were used as negative and positive controls, respectively.

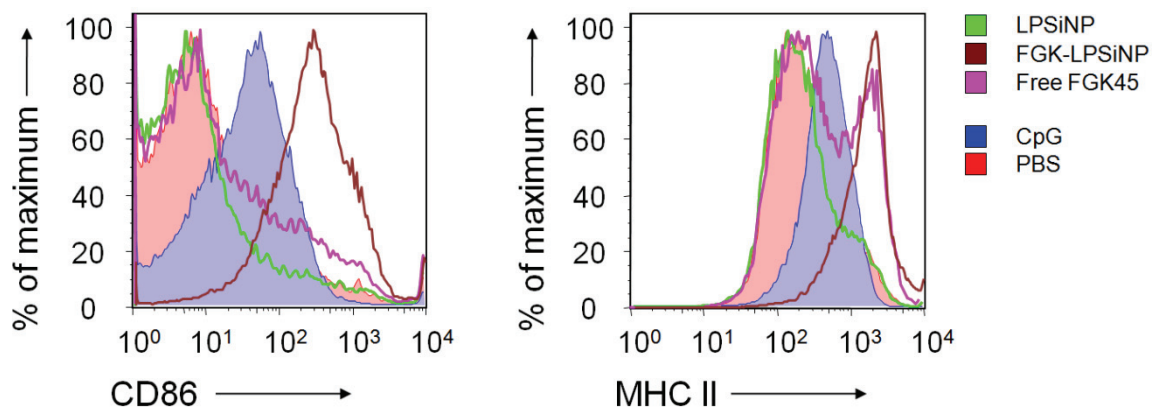


**Figure 6.10 No CD86 or MHC II upregulation of B cells incubated with LPSiNP.** Flow cytometry histograms of B cell activation markers CD86 and MHC II after incubation with 5  $\mu\text{g}/\text{mL}$  of LPSiNPs (green curve), 5  $\mu\text{g}/\text{mL}$  of FGK-LPSiNPs containing 0.29  $\mu\text{g}$  of FGK45 (maroon curve), or 0.29  $\mu\text{g}$  of free FGK45 (magenta curve) for 42 h at 37  $^{\circ}\text{C}$ . PBS (red shaded) and CpG (blue shaded) were used as negative and positive controls, respectively.

Chapter six, in part of full, is a reprint (with co-author permission) of the material as it appears in the following publication: **Gu, Luo**; Ruff, Laura E.; Qin, Zhengtao; Corr, Maripat P.; Hedrick, Stephen M.; Sailor, Michael J., “Multivalent Porous Silicon Nanoparticles Enhance the Immune Activation Potency of Agonistic CD40 Antibody”, *accepted by Advanced Materials*. The author of this dissertation is the primary author of this manuscript.

## **APPENDIX A**

### **Generation of Porous Silicon Images on Si Wafers**

## A.1 Introduction

A luminescent color image or black and white image made of porous silicon (or porous Si residual for black and white images) can be generated on n type silicon wafers with photo-assisted etching<sup>1-2</sup>. Photon illumination on n type silicon can generate charge carriers (electron-hole pairs), and sufficient numbers of holes are needed to carry out the corrosion reaction.

## A.2 Materials

*silicon wafers*: n type silicon wafers with resistivity of  $\sim 0.5 - 1 \Omega$ .

*Electrolyte solution*: electrolyte containing aqueous 48% hydrofluoric acid and ethanol in a 1:1 ratio.

*Etch cell*: Whole wafer (100 mm D.I.) etch cell for large image.

*Base solution*: Mixture of 1 mol/L KOH aqueous solution with 10% (v) ethanol.

*Projector*: A projector fitted with a macro lens.

## A.3 Experimental

1. Assemble etch cell.
2. Set up the projector at a upside down orientation (Fig. A.1). This orientation is easier to adjust focus and doesn't require sealing of etch cell compared to the vertical orientation.
3. Connect the projector with a computer. Project a clear image with black background on the silicon wafer.
4. Use a piece of white paper on the wafer to help adjusting the focus of the image.

5. Add etching solution to the etch cell. Connect the power source with the etch cell.

6. Shut down the lights in the fume hood. Etch at 15 mA for 10 min in the dark. An image should be visible on the wafer a few seconds after start etching. The etching current and time can be adjusted according to the brightness and contrast of the image.

7. Wash the wafer with ethanol 3-5 times. A photoluminescent color image is done.

8. To produce a black and white image with better visibility (Fig A.2). Soak above wafer in the base solution, then wash the wafer with water and ethanol 3 times each.

#### **A.4 References**

1. Doan, V.V. & Sailor, M.J. Luminescent Color Image Generation on Porous Silicon. *Science* **256**, 1791-1792 (1992).
2. Lehmann, V. & Foll, H. Formation mechanism and properties of electrochemically etched trenches in n-type silicon. *Journal of the Electrochemical Society* **137**, 653-659 (1990).

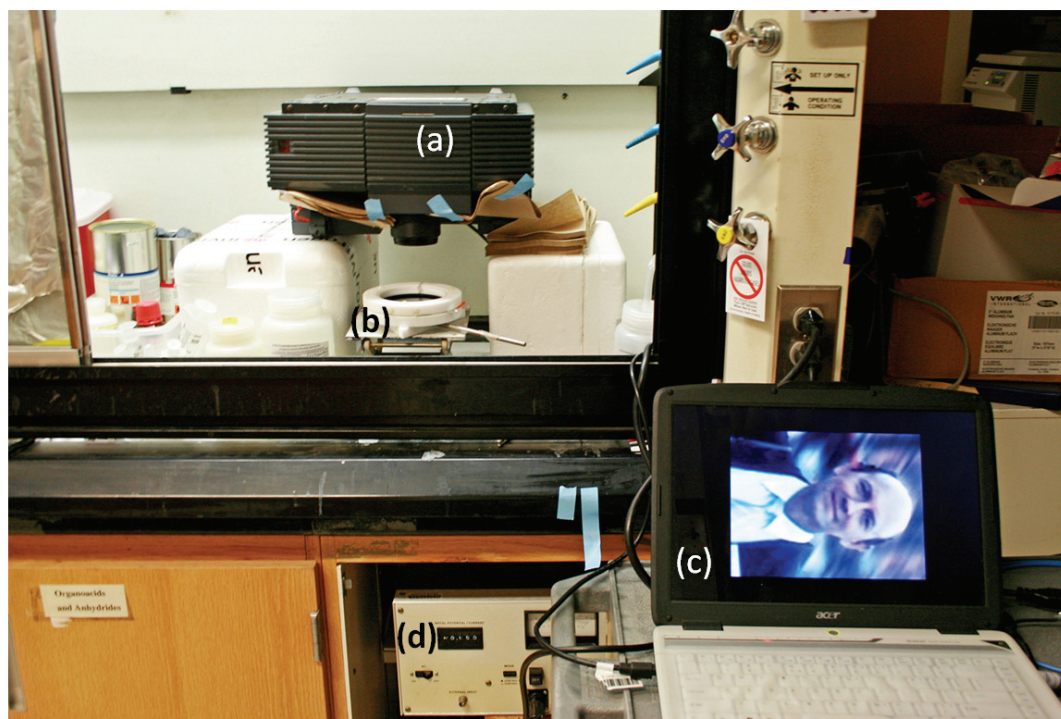


**Figure A.1** The setup of photo-assisted etching of a image on Si wafers. (a) A projector fitted with a macro lens. (b) Whole wafer Teflon etch cell. (c) A computer connected to the projector. (d) Power supply that controls the etching current and time.



**Figure A.2 Black and white images etched on Si wafers. Top:** Prof. Vitali Parkhutik (1951-2006). Known as a meticulous researcher, Parkhutik was a central figure in the field of porous semiconductors, a person who worked tirelessly to bring the community together and to help young scientists succeed. He founded the International Porous Semiconductors Science and Technology Conference in 1998. **Lower left:** Dr. Volker Lehmann (1956-2006). Known for his outstanding scientific contributions in the field of silicon electrochemistry, Lehmann was also an accomplished artist. **Lower right:** Prof. Ulrich Gösele (1949-2009). He was well known and respected throughout the materials science community, publishing extensively in the field of semiconductor physics and solid state nanostructures.